

UNIVERSITY OF ALBERTA

**Electromagnetic modelling and rational design of
GLAD thin films for optical applications**

by

VIKTOR A LEONTYEV

A thesis submitted to the Faculty of Graduate Studies and Research
in partial fulfillment of the requirements for the degree of

DOCTOR OF PHILOSOPHY

in

Micro-Electro-Mechanical Systems (MEMS) and Nanosystems

DEPARTMENT OF ELECTRICAL AND COMPUTER ENGINEERING

© Viktor Leontyev

Spring 2013

Edmonton, Alberta

Permission is hereby granted to the University of Alberta Libraries to reproduce single copies of this thesis and to lend or sell such copies for private, scholarly or scientific research purposes only. Where the thesis is converted to, or otherwise made available in digital form, the University of Alberta will advise potential users of the thesis of these terms.

The author reserves all other publication and other rights in association with the copyright in the thesis and, except as herein before provided, neither the thesis nor any substantial portion thereof may be printed or otherwise reproduced in any material form whatsoever without the author's prior written permission.

To My Parents

Abstract

This thesis presents a theoretical study of columnar films, fabricated by glancing angle deposition (GLAD), as photonic bandgap structures and metamaterials with predictable dielectric and magnetic response. Glancing angle deposition (GLAD) employs extremely oblique vapour incidence and computerized substrate motion to produce nanocolumns with a variety of shapes. Columns grow in random or periodic arrays and may be periodic in one, two, or three dimensions. The films' optical properties were studied using finite-difference time-domain and finite-difference frequency-domain methods, as well as effective medium theories, with support from experimental research.

A large part of the thesis is devoted to column arrays with subwavelength intercolumnar distance and periodically modulated column shape. Among them, s-shaped columns were designed as polarizers for linearly polarized light. Simulations have shown a competitive effect from two structural anisotropy sources, causing a band gap suppression for one of two linear polarizations, and high polarizing ability. Simulations were compared to the measurements with a very good agreement in spectral response. Subwavelength column arrays were further explored as anisotropic interference mirrors with omnidirectional reflection bands. Index graded vertical post films were designed, having up to four times wider reflection bands than in the isotropic analogs.

Band gap properties of 3D periodic GLAD columns were studied on the ex-

ample of square-spiral photonic crystals. A significant influence of column cross-section was shown, that currently prevents fabrication of square spirals with a 3D band gap in the visible range. Inverted square-spiral films have better performance, which is further improved by material redistribution along the spiral.

Lastly, this work studies the effective dielectric response of porous columnar films with metal particles. Characteristic matrix formalism was combined with finite-difference modelling to explicitly calculate their permittivity and permeability, and to study the band gap formation in periodic layers of porous metal. Anisotropic magnetic response was observed in silver columns away from the plasma resonance. Combined with a large permittivity in the infrared, this has potential for future refractive index engineering.

Acknowledgements

I am grateful to many people for making this work possible and for supporting me through its various stages. First of all I would like to thank my supervisors Dr. Andriy Kovalenko and Dr. Michael Brett for inviting me to the University of Alberta, and guiding during these years. Thank you for your constant encouragement, and valuable advice in this work. I am grateful to my supervisory committee members Dr. Jeremy Sit and Dr. Vien Van, who turned out to be my teaching professors, and had a significant impact on the outcome of this work. I am also thankful to Dr. Kyrylo Tabunshchuk, who became my informal supervisor at the very beginning. His early research defined my further work and largely determined the shape of this dissertation. His mentorship turned out to be invaluable and, I believe, made me a better researcher, and better scientific writer.

I would like to thank GLAD experimental group, as my work could not be possible without their experimental support. Polarizers, proposed and fabricated by Nick Wakefield, made a chapter of this thesis and surely deepened our understanding of columnar interference films. The study of index graded interference mirrors with Matthew Hawkeye led to another chapter and to design of omnidirectional reflectors largely outperforming currently known analogs. Collaboration with Joshua Krabbe and Dr. Michael Taschuk in photonic crystals also produced exciting results and formed a part of this thesis. The knowledge of Dr. Taschuk and his willingness to help were priceless and go far beyond our published work. I also thank Douglas Gish for his work on metallic sculptured films. Not all projects were eventually published and described here, but even little collaborations with Ryan Tucker, Douglas Gish, Nick Wakefield, and Zhifeng Huang were exciting and increased my knowledge of sculptured thin films as well as photovoltaics.

Thank you to the Theory and Modelling Group at the National Institute For Nanotechnology for your valuable comments during our seminars, and for friendly supportive environment you created. We were all working on different topics, but this only broadened my vision, and I always enjoyed our lunch time discussions, even when they were distant from science.

But most of all I would like to thank to my parents. Not only did they ignite

in me a spark of scientific curiosity years ago, but they constantly encouraged and supported me in the pathways I took. Thanks to their unfading encouragement, I see this large piece of my work done and even bigger opportunities laying ahead.

Contents

1	Introduction	1
1.1	Motivation	1
1.2	GLAD technique	3
1.2.1	The method	3
1.2.2	Basic GLAD Architectures	5
1.2.3	Substrate Patterning	8
1.2.4	Advanced Substrate Motion Algorithms	9
1.2.5	Film Inversion Techniques	11
1.3	GLAD films as photonic materials	12
1.3.1	Interference mirrors	13
1.3.2	Chiral Films	14
1.3.3	Photonic Crystals	15
1.4	Finite-difference methods for simulation of light propagation	16
1.4.1	FDTD Method	18
1.4.2	FDFD Method	22
1.5	Finite-difference modelling in this work	23
1.6	Summary of the following chapters	27
2	Polarization selectivity in s-shaped columnar films	28
2.1	Motivation	28
2.2	Theoretical model of s-shaped columnar polarizer	30
2.3	Optical properties of s-shaped films and polarizer design	33
2.4	Experimental realization and measured data	41
2.5	Continuous s-shape	45

2.6	Liquid crystals in polarizing film: polarizing switch	48
2.7	Resonant mode narrow band polarizers	53
2.8	Chapter summary	54
3	Omnidirectional reflection	
	from vertical post index-graded films	58
3.1	Motivation	58
3.2	Interference mirrors and omnidirectional reflection	61
	3.2.1 Omnidirectional band gap	63
	3.2.2 Modelling and simulation	66
	3.2.3 Transfer matrix method	67
3.3	Columnar interference filters: the model	71
3.4	Omnidirectional band gap in isotropic and in columnar films . . .	74
3.5	Experimental realization of the columnar mirror	77
3.6	Band gap optimization	80
3.7	Chapter summary	84
4	Square spiral photonic crystals with a visible band gap	86
4.1	Motivation	86
4.2	Fabrication procedure	87
4.3	Simulation and structure optimization	90
	4.3.1 The model	90
	4.3.2 The role of column cross-section	92
	4.3.3 Reflectivity of the square spiral films: comparison to the experiment	93
	4.3.4 Band gap optimization and inverted square spirals	100
	4.3.5 Improving the 3D band gap by density redistribution in the film	101
4.4	Chapter summary	104
5	Metals in GLAD films and refractive index engineering	106
5.1	Motivation	106
5.2	Dielectric properties of materials from transmission and reflection .	109
	5.2.1 Effective medium approximations	112
5.3	Refractive index engineering in the columnar metal films	114

5.3.1	Vertical posts	115
5.3.2	Effective medium approximation	117
5.3.3	Magnetic response	121
5.4	Ordered particles in GLAD films	125
5.4.1	Arrays of the ideal metal particles	126
5.4.2	The experiment and transmission loss in granular metals . .	134
5.5	Chapter summary	138
6	Conclusions	140
6.1	Summary of findings	140
6.2	Challenges and future research	143
6.2.1	Scattering in GLAD films	143
6.2.2	Multiscale and multiphysical simulations	144
6.2.3	Nonlinear processes	144

List of Tables

1.1	Comparison of the FDTD and FDFD methods.	26
2.1	Simulated parameters for the designed and fabricated geometries of s-shaped polarizers.	48
3.1	Coefficients for the series expressing TiO ₂ film density as a function of the effective refractive index.	72
3.2	Maximum reflection band widths for isotropic and anisotropic index-graded mirrors with $n_{max} = 2.4$	84

List of Figures

1.1	Due to the shadowing and material accumulation on the high points of the surface, the film differentiates into the tilted columns.	4
1.2	Glancing angle deposition apparatus.	5
1.3	Typical column architectures grown by GLAD technique: a) slanted posts; b) zig-zags; c) polygonal (square) spirals; d) helices; e) vertical posts; f) variable radius vertical posts, forming an index-graded interference mirror.	6
1.4	SEM image of slanted post film showing how columns fan out in the direction normal to the deposition plane (From [74]).	7
1.5	SEM image of square spiral film that shows a substantial column broadening in a vertical direction (From [55]).	8
1.6	Templating process with GLAD thin films: a) the original film; b) film infiltrated with PMMA; c) inverted porous structure composed of PMMA; d) the original structure restored by electrochemical deposition.	11
1.7	Principal indices of the columnar film.	13
1.8	Schematic representation of Yee staggered grid, and magnetic contour for the E_z field component belonging to one of the electric grid points.	19
1.9	The structure of FDTD simulation domain used to model periodic columnar films.	25
2.1	The model of the s-shaped columnar film.	31
2.2	FDFD calculated location of the band gap edges as a function of slanted post tilt in s-shaped columns (column horizontal cross-section is circular in all segments).	34

2.3	FDFD calculated location of the band gap edges as a function of slanted post tilt in s-shaped columns (column horizontal cross-section is elongated in slanted post segments with $e = 0.167$).	35
2.4	Relation between the cross-section broadening e , needed to close the x-polarized band gap, and slanted segment tilt β'	36
2.5	FDFD calculated location of the band gap edges as a function of cross-section broadening e ($P = 295$ nm; $\beta' = 30^\circ$; $\eta = 0.5$; $f = 64\%$; $n = 2.4$).	37
2.6	FDTD simulated transmittance (left) and Stokes parameters (right) for 20 periods of the s-shaped columns with $e = 0.15$ and all other parameters same as on Figure 2.5 (design option III).	38
2.7	FDTD simulated transmittance (left) and Stokes parameters (right) for 20 periods of the s-shaped columns with $e = 0$ and all other parameters same as in Figure 2.5 (design option II).	39
2.8	FDTD simulated transmittance (left) and Stokes parameters (right) for 20 periods of the s-shaped columns with $e = -0.2$ and all other parameters the same as on Figure 2.5 (design option I).	39
2.9	FDFD calculated location of the band gap edges as a function of slanted post fraction η ($P = 295$ nm; $\beta' = 30^\circ$; $e = 0.11$; $f = 64\%$; $n = 2.4$)	40
2.10	SEM photograph the s-shape columnar film (courtesy of Nicholas Wakefield).	42
2.11	FDTD simulated (left) and experimental (right) transmission spectra for the experimentally realized film ($P = 295$ nm; $\beta' = 33^\circ$; $e = 0.184$; $f = 64\%$; $n = 2.4$).	42
2.12	FDTD simulated Stokes parameters s_1 and s_3 for the experimentally realized film.	43
2.13	Normalized selective transmittance s_1 of the experimentally realized s-shaped film as a function of number of periods, measured and simulated at $\lambda = 515$ nm.	44
2.14	FDFD calculated location of the band gap edges as a function of incidence angle for the s-shaped columnar film realized in the experiment. The XZ plane is an incidence plane and the incidence angle is measured from the Z axis.	45

2.15	SEM image and theoretical model for the continuous s-shaped columns.	46
2.16	FDTD simulated (left) and experimentally measured (right) transmission spectra for the continuous s-shape film. The film parameters used in the simulation are: $P = 510$ nm; $\mathbf{S} = 60$ nm; $e_m = 0.22$; $f = 62\%$.	47
2.17	FDTD simulated transmission spectra for the the same geometry as in Figure 2.16, but with 19 vertical periods.	47
2.18	FDFD calculated location of the band gap edges as a function of cross-section broadening for the discrete s-shaped columns infiltrated with E7 liquid crystal. Crystal molecules are aligned along the columns and the column geometry is defined by: $P = 288$ nm; $\beta' = 35^\circ$; $\eta = 0.5$; $e = 0.17$; $f = 50\%$; $n = 2.5$.	49
2.19	FDFD calculated location of the band gap edges as a function of cross-section broadening for the same structure as on Figure 2.18, and liquid crystal (extraordinary index) aligned along X axis (left) and Y axis (right).	50
2.20	FDTD simulated transmission spectra for 29 periods of discrete s-shape columns infiltrated with liquid crystal. On left image the extraordinary index of LC is aligned along the X axis, and in the right image it is aligned along the Y axis. The column geometry is defined by: $P = 288$ nm; $\beta' = 35^\circ$; $\eta = 0.5$; $e = 0.17$; $f = 50\%$; $n = 2.5$.	51
2.21	The same as on Figure 2.20 but for slightly different column geometry: $P = 288$ nm; $\beta' = 35^\circ$; $\eta = 0.5$; $\mathbf{e} = \mathbf{0.15}$; $\mathbf{f} = \mathbf{50\%}$ and $n = 2.5$.	52
2.22	SEM image and simulated columns for the index-graded rugate filter with anisotropic defect layer (micrograph courtesy of Matthew Hawkeye).	54
2.23	FDTD simulated transmission spectra for x- and y-polarized light passing through the index-graded columnar film with anisotropic defect.	55
2.24	Resonant mode spectral location as function of defect tilt β' for the slanted post defect with circular cross-section (left), and y-elongated cross-section with $e = 0.2$ (right).	55

2.25	Resonant mode spectral location as a function of defect cross-section broadening (defect tilted at $\beta' = 45^\circ$).	56
3.1	Refractive index as a function of position for a single period of sinusoidal, DBR and Gaussian interference mirrors.	62
3.2	The model and SEM image of the index-graded columnar thin film.	64
3.3	Brewster angle in a DBR film as a function of n_1 and n_2	65
3.4	FDFD model for the oblique incidence band gap calculations.	68
3.5	Field notations on the periodic boundaries in the transfer matrix method.	69
3.6	FDFD calculated ordinary and extraordinary refractive index for the vertical post film as a function of the relative film density.	73
3.7	FDFD/TM calculated band gap positions for s- and p-polarized light in isotropic DBR film as a function of incidence angle ($n_{min} = 1.5$, $n_{max} = 2.4$).	75
3.8	FDFD/TM calculated omnidirectional band width as a function of n_{min} for the isotropic films with $n_{max} = 2.4$	76
3.9	FDFD calculated omnidirectional band width as a function of n_{min} for the isotropic films with $n_{max} = 2.5$	77
3.10	FDFD calculated omnidirectional band width as a function of n_{min} for the GLAD columnar films with $n_{max} = 2.4$	78
3.11	Experimentally measured and FDTD simulated normal transmission through sixteen periods of the columnar film with sinusoidal index profile on quartz substrate (from SEM data: $n_{min} = 1.54$ and $n_{max} = 2.32$).	79
3.12	Experimentally measured (dots) and FDFD calculated (lines) band gap positions as a function of incidence angle for the same film as on Figure 3.11.	80
3.13	P-polarized band gap positions as a function of incidence angle compared between the isotropic and columnar films with the identical sinusoidal index profile ($n_{min} = 1.54$, $n_{max} = 2.32$)	81
3.14	FDFD calculated omnidirectional band width as a function of n_{min} and n_{max} for the columnar films with sinusoidal index profile. Star indicates the position of experimentally fabricated film.	82

3.15	FDFD calculated omnidirectional band width as a function of the parameter q for the Gaussian index-graded columnar film ($n_{min} = 1.25$, $n_{max} = 2.4$, $\sigma = 0.22$, points are interpolated with cubic splines). See Section 3.3 for the description of the Gaussian profile model.	83
3.16	Omnidirectional band width as a function of σ the Gaussian index-graded columnar films ($n_{min} = 1.25$, $n_{max} = 2.4$, points are interpolated with cubic splines).	84
4.1	The process flow for nanoimprint lithography	88
4.2	Deposition of a single square spiral period.	89
4.3	The model of square spiral	91
4.4	FDFD calculated band gap width as a function of cross-section elongation in the substrate plane for a direct square spiral optimized at $w_{\parallel}/w_{\perp} = 2.3$ ($\zeta = 1$)	92
4.5	FDFD calculated band gap width as a function of cross-section elongation in substrate plane for direct and inverted square spirals optimized at $w_{\parallel}/w_{\perp} = 1.5$	93
4.6	SEM image of the square spiral (courtesy of Joshua Krabbe)	94
4.7	Simulated and experimental reflection spectra at 20° angle of incidence for p-polarized light.	95
4.8	Simulated and experimental reflection spectra at 20° angle of incidence for p-polarized (a), and for s-polarized light (b)	97
4.9	FDTD simulated p-polarized (a) and s-polarized (b) reflectance at normal incidence from 4- and 10-period square spiral film. Column geometry is fitted to the experimentally fabricated structure.	98
4.10	Measured (a) and FDTD simulated (b) p-polarized reflectance as a function of incidence angle and wavelength. Pitch $P = 468$ nm, lattice constant $a = 314$ nm, arm swing $A = 164$ nm and filling fraction $f_v = 25\%$ (circular column cross-section).	99
4.11	FDTD simulated s-polarized reflectance as a function of incidence angle and wavelength for the fabricated film.	100
4.12	FDFD band structure for the experimentally fabricated square spirals.	101

4.13	FDFD band structure for the inverted titania square spiral optimized for $\eta = 1.5$	102
4.14	FDFD calculated band gap width (a) and optimized geometry (b) for the direct square spiral as a function of density variation along the substrate normal.	103
4.15	Band gap width as function of density variation for the inverted structure.	103
5.1	Solutions of characteristic matrix equations for a 200 nm thick slab with refractive index $n = 2$	111
5.2	FDTD simulated transmission and reflection from the silver vertical posts in square array, with a lattice constant $a = 100$ nm and column diameter $D = 0.5a$	115
5.3	FDTD calculated dielectric permittivity for silver vertical posts in square array with lattice constant $a = 100$ nm and diameter $D = 0.5a$	116
5.4	FDTD calculated dielectric permittivity for silver vertical posts in square array with lattice constant $a = 100$ nm and diameter $D = 0.9a$	117
5.5	Effective medium approximation for the dielectric permittivity of silver vertical posts in square array with lattice constant $a = 100$ nm and diameter $D = 0.9a$	118
5.6	Dielectric function of silver (a), and of the Drude metal with the same plasma frequency $\omega_p = 9.01$ eV (b) (dielectric function for silver is taken from Ref. [99])	119
5.7	Effective medium approximation for the dielectric permittivity of vertical posts made of nonabsorptive metal with the plasma frequency of silver, calculated for material to void ratios $f = 0.1, 0.5$ and 0.7 . Vertical lines indicate the resonance wavelength for each graph.	119
5.8	FDTD calculated magnetic permeability for silver vertical posts in square array with lattice constant $a = 100$ nm and diameter (a) $D = 0.5a$, and (b) $D = 0.9a$	121
5.9	Permittivity and permeability of vertical posts as a function of intercolumnar distance (column diameter is $D = 0.9a$).	122

5.10	Permittivity [real (a) and imaginary (c)], and permeability [real (b) and imaginary (d)] for silver post tilted at $\beta = 0^\circ$ (vertical) and $\beta = 30^\circ$. Columns are arranged in a square array with lattice constant $a = 100$ nm, and column diameter $d = 0.9a$	123
5.11	Permittivity (a) and permeability (b) of slanted posts as a function of column tilt at $\lambda = 1500$ nm ($a = 100$ nm, $D = 0.9a$).	124
5.12	The theoretical model of vertical posts with metal inclusions.	125
5.13	FDTD simulated transmission and reflection through four layers of nonabsorptive metal particles suspended in air (Vertical pitch $P = 500$ nm, in-plane particle separation $a = 120$ nm, particles are discs with radius $r = 50$ nm and height $h = 70$ nm).	126
5.14	Transfer matrix calculated transmission and reflection through four layers of effective medium with dielectric constants obtained with Maxwell-Garnet approximation for the metal cylinders 50 nm in radius, separated by $a = 120$ nm (each layer is 70 nm thick and distance between layers is $P = 500$ nm).	127
5.15	The model of multilayer nanoribbons, infinitely long along the Y axis.	128
5.16	FDTD calculated transmission through four layers of nonabsorptive metallic ribbon arrays suspended in air (vertical pitch is $P = 300$ nm, horizontal pitch $P_x = 120$ nm, ribbon width 20 nm and height 70 nm).	129
5.17	Y-polarized transmittance through four layers of nonabsorptive metallic ribbons of various width d	130
5.18	X-polarized transmittance through four layers of nonabsorptive metallic ribbons of various width d	131
5.19	Transmittance through four layers of nonabsorptive metallic cylinders (left) and hemispherical caps (right) supported by TiO_2 columns.	131
5.20	Transmittance through four layers of silver cylinders (left) and hemispherical caps (right) supported by TiO_2 columns.	132
5.21	Transmission and absorption spectra for TiO_2 columns with four layers of silver inclusions at material to void ratio $f = 78.5\%$ (above) and $f = 54.5\%$ (below).	133
5.22	Experimentally measured transmission spectrum for the film with two and three layers of silver.	135

5.23 Simulated transmission through the experimentally fabricated film (geometry defined from SEM data).	135
5.24 Simulated transmission through the experimentally fabricated film, taking into account granular crystalline structure of metal particles.	137

Chapter 1

Introduction

1.1 Motivation

Porous nanostructures attract interest in science and industry by having properties that are not normally present in the materials they are composed of. Examples are found in solar cell technology [79, 29, 9], energy generation and storage [153, 88, 96, 136], coatings [13], and optical interconnects [121]. In the field of photonics, nanoporous materials are used to engineer films with functional refractive index profiles [147], and to manipulate the flow of light with the aid of photonic band gaps. Photonic band gaps are inherent to the periodically structured materials and appear in one, two or all three dimensions. They are expressed as spectral bands where light cannot propagate through the material. 1D band gaps occur in the interference mirrors, where periodicity is in only one direction. Films and slabs perforated with 2D periodic array of holes or made of a 2D periodic array of posts exhibit 2D band gaps, for the light propagating in the plane of the slab. 3D band gaps appear in a limited number of 3D periodic structures, such as spheres arranged in a diamond lattice [44], woodpile arrangement of rods [76] or square spiral arrays [122]. In the majority of 3D architectures, however, the band gap changes its spectral position considerably as a function of propagation direction, and no single frequency is covered by the band gap in all directions.

Nanoporous materials have high surface area, which makes their properties sensitive to the environment [112, 113, 85]. For example, water adsorption and desorption from nanoporous interference mirrors changes the refractive index enough

for a visible change in the photonic band gap spectral position, and can be used to measure humidity [40]. The surface of porous materials can be functionalized to absorb some specific compounds, such as hazardous gases, for detection purposes.

Some of the most sophisticated porous nanostructures are fabricated by glancing angle deposition (GLAD). GLAD is a variation of physical vapour deposition that employs extremely oblique deposition angles with computer-controlled substrate motion to make arrays of isolated columns bent into various shapes. The columns grow towards the vapour source, and, as the substrate is rotated, form zig-zags, spirals, variable diameter vertical posts, and their combinations. Arrays of these columns are one, two, or three dimensionally periodic, potentially having 2D and 3D photonic band gaps [33, 63].

The goal of this PhD work was a theoretical study of columnar GLAD structures aimed to define the areas where optical GLAD films are most useful, and to investigate opportunities for novel applications in these areas. The columnar films were studied in the following aspects: (i) as anisotropic index-graded films, (ii) as three dimensional photonic crystals, and (iii) as matrices for ordered arrays of metallic nanoparticles.

Columnar films can be treated as anisotropic index-graded films, when illuminated by light of wavelength much longer than the intercolumnar distance. Column arrays then have optical properties of a uniform but effectively bianisotropic material. Such a material is fully characterized by three principal refractive indices and orientation of two optical axes. In GLAD films, each of these five variables can be changed throughout the deposition. A large part of presented work will be devoted to anisotropic GLAD films. Chapter 2 will explore the anisotropic polarizers, where band gaps are sensitive to a light polarization state, and Chapter 3 will discuss the role of anisotropy in omnidirectional reflection from graded index interference mirrors.

At wavelengths comparable to the intercolumnar distance, GLAD films cannot be treated as effectively uniform, but rather express themselves as photonic crystals [142]. Theoretically it was shown that square spiral columnar films can have a true 3D band gap (range of wavelengths covered by the band gap in all directions) for a limited range of column geometries [122]. The band gap has been observed experimentally in silicon square spirals, but not for all propagation directions. In Chapter 4, GLAD square spiral photonic crystals will be considered, with the

band gap in the visible spectral range. The column nanoscale geometry will be studied in detail showing the limitations and opportunities of GLAD in making these crystals.

Many opportunities appear when metal particles are included into the structure of periodically ordered GLAD films. As opposed to suspensions in solids or liquids, metal particles in GLAD columns can form periodic arrangements combining plasmon resonance with the band gap phenomena. It was shown both theoretically and in experiments that metal nanoparticle arrays can have negative magnetic permeability and negative refractive index [53, 35]. GLAD films as templates for the ordered metal particles will be discussed in Chapter 5.

The work presented here is focused on theoretical investigation and design of columnar GLAD films for novel optical applications. The work has been largely carried using finite-difference time-domain and frequency-domain numerical techniques. These methods have been known for several decades and are currently used to simulate many complex scattering geometries. The goal of my work was to systematize the optical properties of GLAD films, outline their strengths, and develop new photonic materials with the knowledge gained.

In the following sections, GLAD technique will be reviewed and finite-difference numerical methods will be described.

1.2 GLAD technique

1.2.1 The method

GLAD technique uses physical vapour deposition at extremely oblique vapour incidence and computer-controlled substrate motion to engineer porous columnar films with various column shapes [102, 111, 38, 63, 54]. The substrate is kept at relatively low temperatures during the deposition to limit the mobility of deposited molecules, and let them settle close to the sites of their first impact. Geometrical shadowing is the dominant factor governing the microstructure of the deposited film.

As vapour arrives at grazing incidence, protruding features of the surface intercept more molecules than the valleys, and accumulate more material. Gradually these protrusions extend into columns tilted towards the vapour source (Fig-

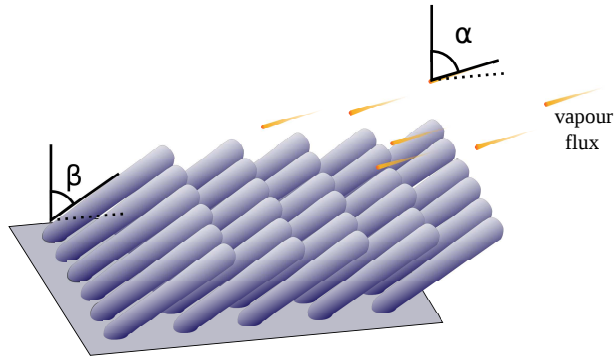


Figure 1.1: Due to the shadowing and material accumulation on the high points of the surface, the film differentiates into the tilted columns.

ure 1.1). The initial substrate roughness, causing film differentiation in columns, can be created artificially by substrate seeding, but in the absence of seeding, the vapour itself tends to form nanodroplets on the surface. These nanodroplets form an initial roughness needed for the column growth. Deposition is performed at low gas pressures, at which molecules travel from the source to the substrate in straight lines, and form a distinct shadowing pattern on the rough substrate surface. As the substrate orientation is changed, the shadowing pattern changes and so does the direction of column growth. This change in the growth direction ultimately gives the main degree of control over the nanoscale film structure.

The typical GLAD deposition setup is shown in Figure 1.2. Molecules of evaporated material travel along straight lines in a high vacuum chamber, and impinge on a tilted substrate. The plane of substrate tilt is called the deposition plane and the tilt angle is called the deposition angle α . This angle can be varied during the deposition by computer controlled step motors. The substrate orientation is also characterized by the rotation angle ϕ . To ensure a proportional size of column segments, that grow at fluctuating deposition rate, this rate is measured by a crystal thickness monitor and synchronized with substrate motion speed.

GLAD deposition is typically performed by evaporation or sputtering. In E-beam evaporation, material is placed in a crucible and continuously scanned by an electronic beam. The beam melts the material and heats it to a high temperature at which it evaporates [60]. The composition of the deposited film is determined by the molecular composition of evaporated material, ability of components to

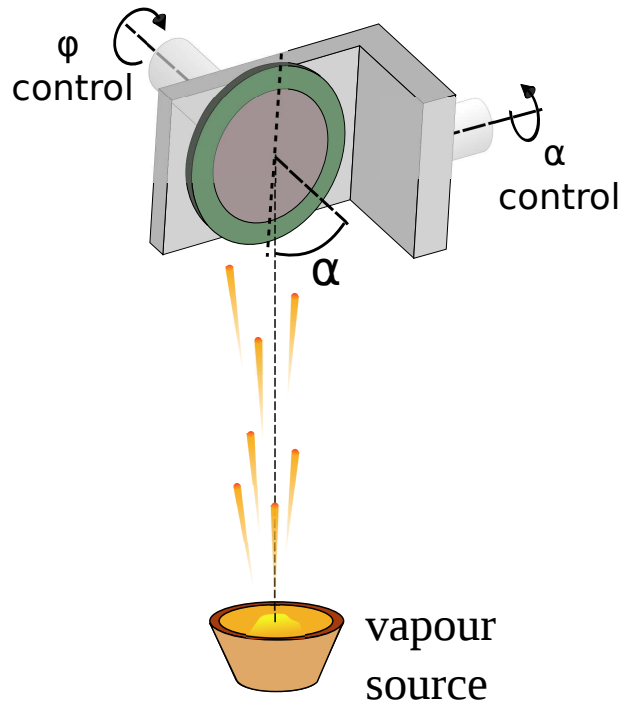


Figure 1.2: Glancing angle deposition apparatus.

condense as a film, and the background environment that molecules have to pass while travelling to the substrate. Many GLAD materials are multi-atom molecules, and different atoms in these molecules have different deposition efficiency. For example, titanium dioxide forms the films with a lower oxygen content than in the evaporated material. This is usually corrected by introducing more oxygen into the deposition chamber [72].

Several evaporants can be deposited simultaneously from separated sources to make composite materials. Such deposition may not produce a film of a new chemical composition, but form a film with one material suspended in another. For example, simultaneous deposition of metal and dielectric produced a dielectric columnar film with metal nanoparticles suspended in the columns [42].

1.2.2 Basic GLAD Architectures

Based on the substrate motion algorithm, GLAD architectures can be split into several classes shown in Figure 1.3. The simplest motion algorithm has both the

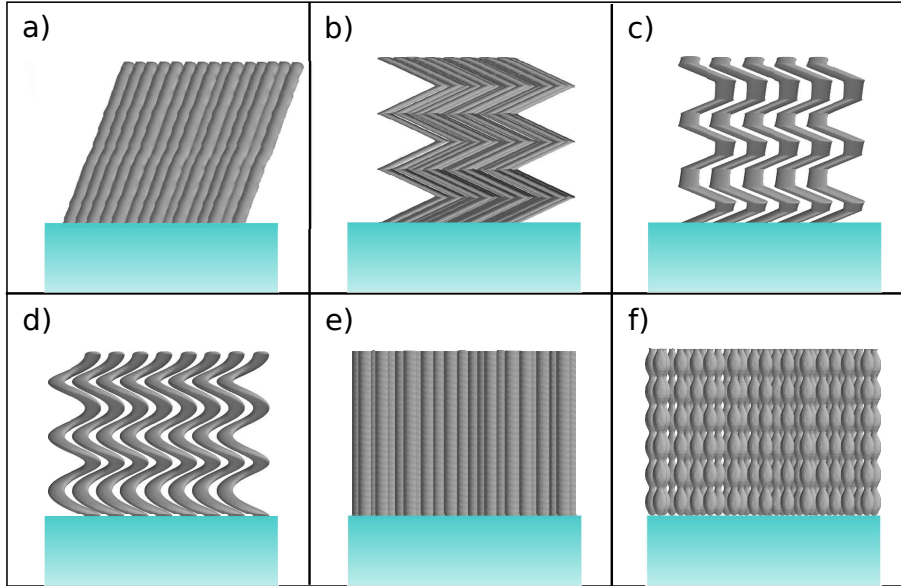


Figure 1.3: Typical column architectures grown by GLAD technique: a) slanted posts; b) zig-zags; c) polygonal (square) spirals; d) helices; e) vertical posts; f) variable radius vertical posts, forming an index-graded interference mirror.

deposition angle α and rotation angle ϕ fixed throughout the deposition. The film grows as an array of slanted posts tilted at an angle β towards the vapour source. This angle is lower than the deposition angle α and determined mainly by the deposition angle and by the deposited material. Several relationships between these two angles were derived based on empirical data fitting [92, 45, 139], geometrical analysis [120], and column growth simulations [75]. One such relationship, that empirically accounts for the deposition angle and deposited material is [139]:

$$\tan\left(\frac{\beta}{C}\right) = \frac{1}{2} \tan(\alpha), \quad (1.1)$$

where C is a material dependent constant, which was found to be $C = 0.53$ and $C = 0.78$ for titanium dioxide and magnesium fluoride respectively in the deposition angle range $0^\circ < \alpha < 80^\circ$.

In slanted post films, shadowing occurs in the deposition plane, but not perpendicular to it. As a result, columns fan out in the direction normal to the deposition plane, and often merge to form ribbon-like structures. The example

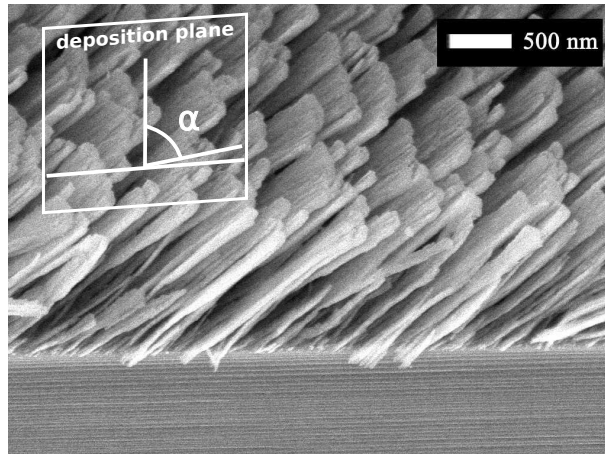


Figure 1.4: SEM image of slanted post film showing how columns fan out in the direction normal to the deposition plane (From [74]).

is shown in Figure 1.4. The column coalescence can be further promoted if the substrate is patterned with narrow lines normal to the deposition plane, leading to highly ordered ribbons [114].

In more sophisticated motion algorithms, the rotation angle ϕ is varied during the deposition. Discrete rotations by $\pm 180^\circ$ produce zig-zag structures, in which column growth direction alternates between two opposite azimuths, but the average column growth remains vertical. This substrate motion algorithm is known as a serial bideposition technique (SBD), and has been previously used to produce biaxial films of high optical birefringence [47, 48, 98, 49].

When the substrate is rotated at a constant speed ($\phi(t) = \omega \cdot t$) vertical helices are formed [50, 130, 102]. The turn radius of these helices is smaller at fast rotation speeds and larger at slower speeds. At very high rotation speed, the helix radius becomes smaller than diameter of the column and helix degenerates into a vertical post.

An important class of columnar films is formed when vertical posts are deposited at a variable deposition angle. The column radius then becomes a function of the vertical coordinate, and so does the film's effective refractive index. Index-graded vertical posts were thoroughly studied as rugate interference filters and as nanoporous gas sensors [113, 40], and will be addressed in detail in Chapter 3 of this thesis.

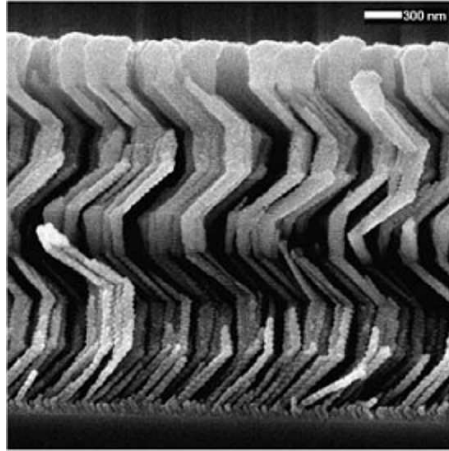


Figure 1.5: SEM image of square spiral film that shows a substantial column broadening in a vertical direction (From [55]).

If the substrate is periodically turned by $\Delta\phi = \frac{2\pi}{n}$, where $n = 2, 3, 4, 5, \dots$ etc., polygonal spirals form [128]. Zig-zag columns ($n = 2$) and helical columns ($n = \infty$) can be classified as particular cases of this class of architectures. One frequently studied type of the polygonal spiral is a square spiral, with $n = 4$. It has been proven to have 3D band gaps at least in theoretical research [122, 123]. Square spirals will be addressed in Chapter 4 of this thesis, where the importance of column cross-section will be shown and a search will be undertaken for column geometries with 3D band gaps in the visible spectral range.

1.2.3 Substrate Patterning

Whatever the substrate motion algorithm is, the film's architecture is influenced by an initial arrangement of seeds on the substrate. If film is deposited on a clean substrate without seeds, adsorbed atoms of evaporated material either form monolayers or nucleate, depending on their attachment strength to each other, binding energy to the substrate, and substrate temperature [91]. The initial nuclei of deposited material then create shadowing pattern needed for columnar growth. Columns are randomly distributed on a substrate and usually tend to increase their diameter as they grow. This column broadening creates a competition, in which some columns stop growing, while other continue to grow and broaden even more (see Figure 1.5). The film porosity, however, remains constant with the

column height [63, 38]. If films are deposited on a seeded substrate, the initial shadowing pattern is created by an existing array of seeds. Each seed produces a single column if it has the same radius as an equilibrium radius of the columns grown on an unseeded substrate [54, 115]. The spatial density of seeds also needs to be comparable to the equilibrium column density. If seeds have a much larger diameter than the average column in the unseeded film, multiple columns will sprout from each seed, and if intercolumnar spacing is too large, columns will grow between seeds.

Seeds are most often prepared by e-beam lithography, photolithography or nanoimprint lithography, depending on the seed specifications, size of seeded area, and potential application [54, 114]. E-beam lithography [60] is often used in the research work, being the most precise lithographic method currently available. The disadvantage of e-beam lithography is that it only can cover small substrate areas, as it is a time consuming nonparallel method. Larger seeded areas are prepared by e-beam lithography to be used as matrices for other lithographic methods, for example for nanoimprint lithography.

Photolithography is suitable for large area seeding and used both in laboratory and industrial scales [60, 52]. This method is the dominant one in CMOS microfabrication, with the resolution approaching 10 nm. These resolutions have been achieved by decreasing the wavelength of projected light and by using sophisticated optical systems. As a result, the projecting equipment for high resolution lithography is exceedingly costly for research purposes.

Nanoimprint lithography [36, 101] uses a stamp, fabricated once (using e-beam lithography for example), and applied multiple times to seed the substrates. The stamp is prepared as an array of protruding dots, and then mechanically impressed into a layer of nanoimprint resist. Substrate nanoimprint seeding has been reported for seed sizes and lattice constants below 100 nm, which makes the method useful both for industry, and for research.

1.2.4 Advanced Substrate Motion Algorithms

Sections of GLAD films deposited at fixed azimuth and deposition angle tend to fan out and increase diameter as they grow. Advanced substrate motion algorithms prevent these effects, and reduce column bifurcation, merging and other deviations

from the ordered arrangement. Several techniques were developed to control the column diameter, cross-section shape, and the amount of broadening along the vertical direction. One of these techniques, called PhiSweep, is often employed during square spiral film fabrication [55, 63]. Instead of depositing each arm at a constant azimuth ϕ , this angle is quickly alternated between two values $\phi - \gamma$ and $\phi + \gamma$. Provided that the frequency of angle alternations is high enough, columns grow in vanishingly small increments at an average azimuth ϕ . The PhiSweep has a profound impact on a film's morphology. With PhiSweep, a column's diameter significantly decreases, while the mean film density remains the same as in the film deposited at a constant azimuth. Due to a more uniform shadowing distribution, the column horizontal cross-section becomes closer to circular. Also, less column broadening is observed, making the columns more uniform along their length. The positive effect of PhiSweep disappears when the PhiSweep growth increments become comparable to or smaller than the typical column radius.

Another motion algorithm, used to control column cross-section and improve the morphology, is a variable-alpha post (VAP) method [63]. Here both substrate rotation ϕ and deposition angle α precess around a certain fixed axis. The method brings column's cross-section closer to that of a tilted cylinder, and minimizes the cross-section distortions at abrupt column turns.

The spin-pause method is another algorithm used to alter the column tilt and porosity [103]. Usually one needs to decrease the deposition angle to reduce column tilt. Film density is changed, however, when deposition angle is decreased. With spin-pause method it is possible to vary column tilt while keeping a film density fixed. The deposition angle is fixed, and substrate motion quickly alternates between two modes — fast continuous substrate rotation and fixed angle deposition. The columns grow in vanishing increments of tilted and vertical posts, with the average tilt β' determined by the ratio of spinning to stopped time. If the rotation is stopped all the time column tilt is at maximum β , defined by the deposition angle and by the type of the deposited material. If the substrate is rotated without stopping, the column will grow vertically. The spin-pause technique thus allows one to control the film's anisotropy and optical axis tilt in birefringent columnar films. The value of β' relative to β is determined by the fraction of spinning time δ during the tilted segment deposition as $\tan \beta' = (1 - \delta) \tan \beta$. The spin-pause technique affects the column's cross-section, which is elongated normally to the

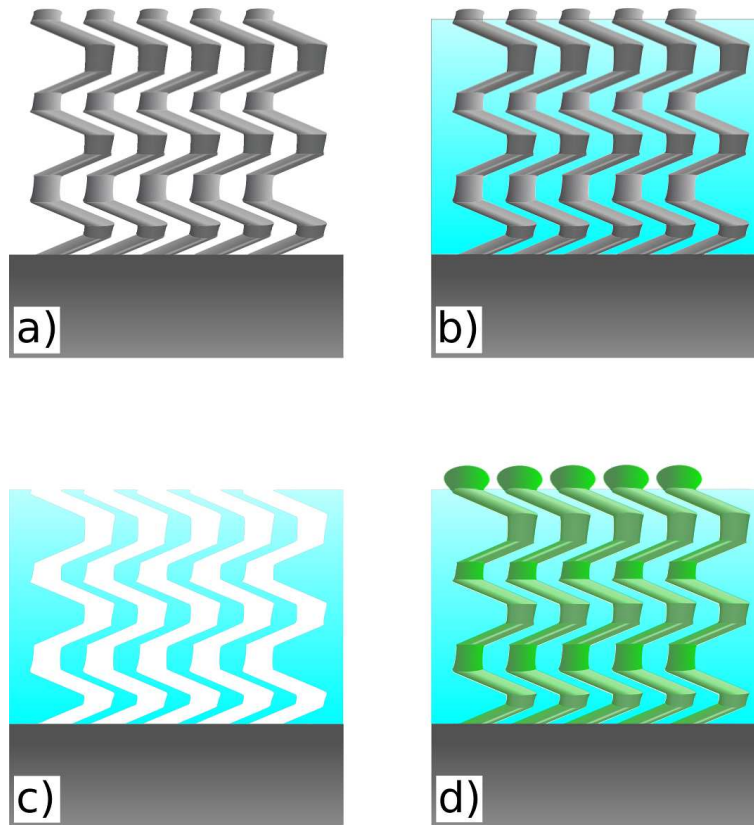


Figure 1.6: Templating process with GLAD thin films: a) the original film; b) film infiltrated with PMMA; c) inverted porous structure composed of PMMA; d) the original structure restored by electrochemical deposition.

deposition plane if $\beta' > 0$, and circular if $\beta' = 0$. The cross-section anisotropy is the highest when $\beta' \rightarrow \beta$.

1.2.5 Film Inversion Techniques

Inverted columnar films are composed of air columns a dielectric matrix, and sometimes have enhanced optical properties, such as wider 3D band gaps in inverted square spirals. Film templating is used to invert GLAD columns (see Figure 1.6). In the templating process films are fabricated using material, which can be later etched away. Silicon dioxide, for example, readily forms columns, and can be selectively etched away after filling with PMMA (polymethyl methacrylate) polymer. The polymer is infiltrated into the film, and then part of it is etched back to expose

silicon dioxide columns. The columns are chemically removed, leaving a polymer membrane perforated with pores copying the architecture of GLAD film. Instead of polymer, other materials such as metals can be used [11].

In a double templating, the porous polymer membrane is infiltrated again with a third material, and then the polymer is etched away. This method brings back the original template, but made of a different material. The method is useful when columns need to be made from materials that cannot be directly or easily deposited by GLAD. Some metals for example, have relatively low melting temperatures and high atom diffusion length preventing efficient column differentiation when deposited directly by GLAD.

1.3 GLAD films as photonic materials

Photonic band gaps form due to the destructive interference of light on periodic structures, when their spatial period is close to the wavelength of light. The band gap spectral position and width depend on the propagation direction and, in most cases, a given wavelength is not covered by the band gap in all directions in 3D space. If it does, the periodic structure is regarded as 3D photonic crystal due to the similarity between the photonic band gaps and electronic band gaps in crystal lattices. If the condition holds only in a plane, the structure is considered as a 2D photonic crystal, and in index-graded waveguides and interference mirrors band gaps exist only in one dimension. The latter are often studied using analytic theories, such as coupled mode and transfer matrix theories [22, 145].

GLAD films can be 3D, 2D or 1D periodic, depending on the motion algorithm and substrate seeding. If deposited on a periodically seeded substrate with appropriate periodic motion algorithm, they potentially form a 3D photonic crystal. Among columnar architectures only square spiral structure is known to have a 3D band gap so far. 2D photonic crystals are easier to fabricate, due to fewer restrictions. GLAD vertical post arrays can be an example of these, but are easily outperformed by similar structures fabricated by deep reactive ion etching in silicon and silica slabs. Structures obtained by etching form arrays of air posts, which have larger band gaps than dielectric posts in air. The walls of etched pores are also smoother than the GLAD column surface, therefore GLAD fabrication of 2D crystals does not seem practical at this time.

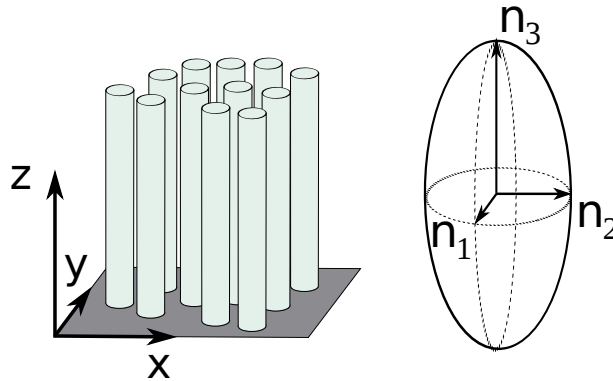


Figure 1.7: Principal indices of the columnar film.

1D periodic GLAD films, however, deserve attention. In a special case, when the intercolumnar spacings are much smaller than the wavelength of light, GLAD columns transfer light as an effectively uniform, but anisotropic medium with three principal refractive indices n_1 , n_2 and n_3 , as shown on a Figure 1.7. When all three indices are different, the material is bianisotropic (having two optical axes) and its optical properties are fully characterized by three indices and three angles describing the optical axes' orientation. GLAD columns are generally bianisotropic except vertical posts, which are rotationally symmetric and uniaxial. If the film is deposited without rotation, one optical axis is normal to the deposition plane (due to mirror symmetry relative to this plane), and the other one is oriented along the columns. The effective refractive indices can be calculated approximately with an effective medium theory, but accurate dispersion relations are obtained only with numerical methods. If the refractive index and principal (optical) axis orientation varies along the column length, the film becomes a 1D graded-index interference mirror.

1.3.1 Interference mirrors

A GLAD film, if deposited on unseeded substrate at a constant rotation, forms as a closely spaced array of vertical posts, with intercolumnar distances of an order of 100 nm [39]. The density of these films can be varied by the deposition angle, causing corresponding variations of the refractive index. In the visible spectral range, titanium dioxide is often used, as it is a high index material which is trans-

parent in this range and may be deposited by GLAD. A high refractive index is needed to produce wide photonic band gaps.

Vertical posts are rotationally symmetric and films can be characterized by two indices: $n_1 = n_2 = n_o$ (ordinary index) and $n_3 = n_e$ (extraordinary index). The ordinary index is measured in the substrate plane, and the extraordinary index along the column axis. The measured relationship between n_o and deposition angle covers the range $1.16 \leq n_o \leq 2.23$ [39] for TiO₂ vertical posts. Birefringence, defined as a difference between ordinary and extraordinary indices $\Delta n = n_e - n_o$, has also been studied for several metal oxides [47], with the maximum value for titanium dioxide of $\Delta n = 0.15$ at deposition angles $\alpha \sim 65^\circ$.

With the relation between the deposition angle and refractive index known, one can program the film's refractive index profile as desired. Discrete profiles, with step-wise index variation, and sinusoidal ("rugate") profiles were studied previously and band gaps were shown in the infrared and visible regions [37, 118].

If defect layer is inserted in a periodic sequence, the defect mode appears in the band gap as a narrow transmission line. Interesting gas and humidity detecting opportunities were shown for the films with defect layers [113]. The resonant mode is narrow compared to the band gap, and even small changes in refractive index cause a detectable shift. In humidity sensors the response is fast, and can be cycled repeatedly without noticeable film degradation [40].

Defect modes in the columnar films are also interesting by their optical birefringence, since their spectral position may be polarization-dependent, even if the band gap itself is insensitive to the polarization of light. By infiltrating the defect with liquid crystal it may also be possible to make the defect mode position sensitive to an external electric field.

1.3.2 Chiral Films

Anisotropic materials with a helically twisted optical axis form a class of structurally chiral materials. Naturally, these materials occur as a chiral nematic phase of liquid crystals. They are classified as left-handed or right-handed depending on the direction of axis rotation. In right-handed materials, the rotation is clockwise if the imaginary plane is moved away from the observer looking along the helix, and left-handed in the opposite case. Accordingly, right-hand circularly polarized light

(RCP) has an electric vector rotating clockwise relative to the observer looking into the beam, and left-hand circularly polarized light (LCP) has counterclockwise electric vector rotation. Chiral materials selectively reflect light of one handedness, while transmitting the other one.

GLAD helical films are chiral because their optical axis is helically twisted along the substrate normal. They are deposited at a constant substrate rotation, with the deposition angle α fixed. The helix pitch is defined by the rotation frequency and deposition rate, while the degree of anisotropy is determined by deposition angle and deposited material.

The optical response of chiral films is characterized by the difference between the RCP and LCP transmittance $\Delta T_{RCP-LCP}$. It has been shown, both theoretically and experimentally, that helical GLAD films have polarization-selective band gaps for circularly polarized light [130, 131, 50]. Both band gaps also can exist simultaneously with one band gap much weaker than the other one. The right-handed films have an RCP band gap, while LCP band gap is either weak or not observed. In a trigonal (3-sided) spiral, which is also chiral, band gaps were observed for both LCP and RCP light, but were located at different wavelengths [128].

1.3.3 Photonic Crystals

Only a limited number of spatially periodic dielectric structures have three dimensional photonic band gaps, and their fabrication on a microscale is challenging. 3D band gaps were reported in “woodpile” structures, and in diamond-like structures formed by drilling crossed pores in the solid. The widest band gaps were found in the diamond lattices of overlapping spheres (and even wider in their inverted form) [44]. Smaller band gaps were found in FCC (face centered cubic) and hexagonal close packed (HCP) lattices of aspherical particles, and in a cubic lattice of spheres [143].

A series of theoretical studies [123, 122] have shown that wide band gaps can exist in the square-spiral columnar structure where column arms connect nodes of a diamond lattice. This structure can be fabricated by GLAD, because nodes of the lattice, when projected on FCC lattice, form a series of parallel layers, connected by a series of parallel lines. In each layer, nodes form a square array, identical to

arrays above and below, but shifted in relation to them. The deposition is started from a square array of seeds to form slanted posts. As column tips reach the next plane, substrate is turned by 90° either clockwise or counterclockwise. The column tips always stay in the plane parallel to the substrate, and preserve the initial square arrangement, determined by the substrate seeding.

As arms pass from one layer to the next, they do not necessarily connect the nearest nodes. Square spirals connecting the nearest neighbours (diamond:1), every third neighbour (diamond:3) and every fifth neighbour (diamond:5) of diamond lattice were theoretically considered in works of Toader et al. [123, 122]. Band gaps larger than 10% were found in all configurations, if columns were made of silicon (refractive index of silicon is $n \approx 3.5$ in the near infrared). The widest 3D band gaps were observed for diamond:5 spirals, and the smallest for the diamond:3 architecture, indicating that wide band gaps of square spiral films are not necessarily due to their connection with the diamond lattice. This conclusion was supported by the fact that in the optimized square spiral geometries, arms pass relatively far from the diamond lattice nodes.

The same studies have also shown that the cross-section shape influences the photonic band gap. Rectangular cross-sections showed wider band gaps than circular. Inverted structures also had wider band gaps than the direct ones, which is a well known trend among photonic crystals.

Only one of the geometries described in the work of Toader et al. is within the potential reach of GLAD technique: the diamond:1 structure. Arms of the optimized diamond:1 column are tilted at 64° from the substrate normal, which is close to the limit of GLAD method. Diamond:5 columns have even larger tilt, and therefore not considered in the experiments.

1.4 Finite-difference methods for simulation of light propagation

Numerical modelling occupies a significant niche in nanomaterial research, and its popularity continues to increase. While analytical methods give deep insight into the physics of the processes, their predictive ability is limited to a small number of models. Numerical methods give an approximate solution with a high accuracy,

yielding results similar to experimental. In electromagnetics, several families of numerical methods are used, depending on the problem which is being solved. All of these methods are based on one or another form of Maxwell's equations. In the differential form, the equations link electric and magnetic fields and their time derivatives:

$$[\vec{\nabla} \times \vec{E}] = -\frac{\partial}{\partial t} \vec{B} - \vec{K}, \quad (1.2)$$

$$[\vec{\nabla} \times \vec{H}] = \frac{\partial}{\partial t} \vec{D} + \vec{J}, \quad (1.3)$$

$$\vec{\nabla}(\epsilon \vec{E}) = \rho / \epsilon_0, \quad (1.4)$$

$$\vec{\nabla}(\mu \vec{H}) = 0, \quad (1.5)$$

where \vec{E} and \vec{H} are electric and magnetic field vectors, $\vec{D} = \epsilon \epsilon_0 \vec{E}$ is an electric displacement vector, $\vec{B} = \mu \mu_0 \vec{H}$ is a magnetic induction, ϵ and μ are the relative permittivity and permeability, \vec{J} and \vec{K} are electric and magnetic current densities, and ρ is the electric charge density. Magnetic charges, as well as magnetic currents, have not been found in the nature, but an artificial system of surface magnetic currents is often used in numerical simulations to represent a complex scattering body by a closed surface with certain distribution of electric and magnetic currents.

Numerical techniques, such as the finite-difference time-domain method (FDTD), finite element method (FEM), and finite volume methods discretize these equations in one or another way in space and propagate the solution in time using some set of initial and boundary conditions [119, 71]. These methods calculate the time dependence of a spatial field distribution, which is further used to find transmittances, absorption and other parameters directly compared to the experiment. The disadvantage of time-dependent methods is high demand on computer memory and time, because all points of a simulated domain have to be stored, and the fields are evolved through a large number of time steps.

In many instances, it is possible to find a steady state solution by solving a frequency dependent Helmholtz equation:

$$[\vec{\nabla} \times \frac{1}{\epsilon \epsilon_0} [\vec{\nabla} \times \vec{H}_k]] = - \left(\frac{\omega}{c} \right)^2 \vec{H}_k. \quad (1.6)$$

The Helmholtz equation is obtained from Maxwell equations by representing

electromagnetic waves as a series of harmonic plane waves in the form

$$\vec{H} = \sum_{\omega=1}^{\infty} \vec{H}_{\omega} \exp[i(\omega t + \vec{k} \cdot \vec{r})]. \quad (1.7)$$

The finite-difference frequency-domain (FDFD) method is often used to solve this equation. In FDFD, the problem is discretized with finite differences in space and represented as an eigenproblem $Ax = \lambda x$. The solution is a set of eigenmodes and eigenfrequencies for the system. The method is thus useful for the problems that involve waveguiding, or light transport in periodic structures. The Method of Moments (MoM) is another method that solves Helmholtz equation using Green's functions and discretizes the problem over the object's surface. Numerical techniques that use surface discretization, such as Method of Moments, are better suited for the problems with low surface-to-volume ratio. In scattering problems, involving a single scattering body these methods are preferred [140]. GLAD films have high surface-to-volume ratios, therefore volume discretization methods, such as finite-difference or finite-volume methods are more suitable for them. The current work is based on finite difference methods, which are described below.

1.4.1 FDTD Method

In the finite difference methods, space and time are discretized with a grid of points and derivatives are calculated based on the field differences between the adjacent points. In the time domain, Yee discretization method is used for the spatial coordinates [146]. In this method two staggered rectangular grids are used, one for the electrical field values, and the other one for magnetic fields, as shown on Figure 1.8. The grids are displaced relative to each other in such a way that each electric field point is surrounded by six magnetic field points. Similarly each point carrying the magnetic field is surrounded by six electric field points. The magnetic points surrounding each electric field point form three magnetic contours, naturally satisfying Ampere's Law for each electric field component. The electric points, accordingly, form three closed contours around each magnetic point, satisfying Faraday's law. By discretizing the equations into two staggered grids, the method automatically takes into account the integral form of Maxwell's equations.

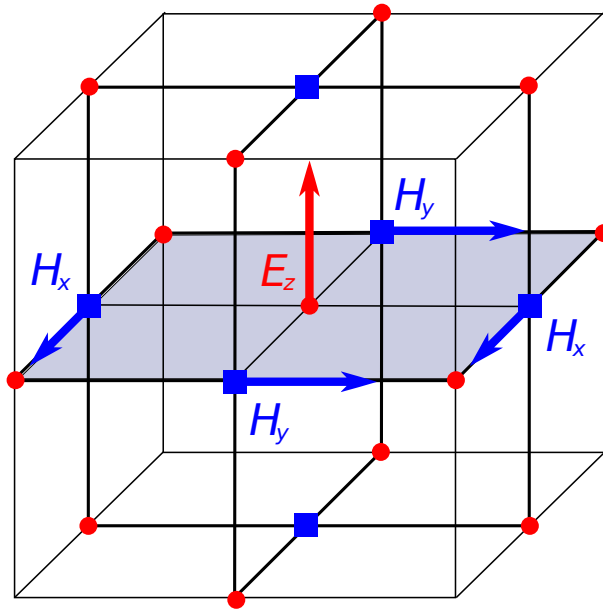


Figure 1.8: Schematic representation of Yee staggered grid, and magnetic contour for the E_z field component belonging to one of the electric grid points.

Fields are updated in time in a leapfrog manner, with the magnetic field being updated in one half step, and its new value used to update the electric field in the alternate half-step. With Yee discretization and leapfrog time stepping FDTD has a second-order numerical accuracy. Computational cost grows as a fourth order of the grid resolution in 3D space, because the number of cells increases cubically and the number of time steps grows proportionally to the resolution. The maximum time step is defined by a Courant-Friedrichs-Lewy (CFL) stability condition:

$$\Delta t \leq \frac{\Delta n_m}{c\sqrt{N}},$$

where Δ is a spatial grid step (if equal in all dimensions), $N = 1, 2,$ and 3 for one, two and three-dimensional space, and n_m is a minimum refractive index that occurs in the computational domain. This condition is a mathematical expression of the fact that the information on a Yee grid does not propagate further than by one spatial cell in a single simulation step.

In the time domain, Maxwell's equations require both initial and boundary conditions. The initial field distribution is usually set to zero and the boundary

conditions are most often either Bloch periodic, or open. With Bloch periodic conditions, fields on the one side of computational domain are equal to the fields on the opposite side with a phase shift: $\psi(\vec{R}) = \psi(\vec{R} - \vec{L}) \cdot \exp(i\vec{k}\vec{L})$, where L is domain size along the axis normal to the given boundary, and \vec{k} is the propagation vector of light at a given frequency. Most often, the vector \vec{k} is chosen in such a way that $(\vec{k}\vec{L}) = 0$, then multiple frequencies can be simulated simultaneously.

Almost all problems involve open boundary conditions along one or more spatial coordinates. Open boundaries are most often simulated by absorbing non-reflective layers of artificial material, called perfectly matched layers (PML). PML layers have the same impedance value as the adjacent space to ensure the absence of reflection, and a finite conductivity to absorb passing light. PML layers are placed adjacent to cell boundaries while the boundary can be either Bloch periodic, or have all fields suppressed to zero (perfect metal boundary). As a consequence any fields that are not absorbed by PML either appear on the opposite domain side or, reflected by perfect metal boundary return on the same side. These fields decrease the simulation accuracy, but usually to a very little extent [119].

Light sources are added as current sources $\vec{J}(\vec{r}, t)$ in the point or in the plane. The sources defined in this way are transparent to radiation, and do not interfere with the scattered field. A wavefront of any shape can be assigned using a planar source with a functional dependence $\vec{J}(\vec{r}, t)$. This is used to define plane waves with arbitrary propagation angles originating in planes parallel to the grid mesh.

Due to a conceptual simplicity and versatility, the FDTD method has found many applications. Radar cross-sections for airplanes [119], scattering from dust and snow particles [144], and scattering in biological cells [107] are only a few examples which encompass scales from micrometers to several meters. Systems studied in the present work are in the nanoscale range and will be considered at infrared, visible and ultraviolet wavelengths.

Many dispersive, anisotropic, and nonlinear materials can be simulated with FDTD. Permittivity and permeability are functions of coordinates and time if the equations are written in the time domain. Frequency-dependent approximations are Fourier transformed to be simulated in FDTD and, since the transformation has to be analytical, only a limited number of such approximations can be used. The Lorentz dielectric model is frequently used and accurate enough to simulate many practically important dispersive materials, including metals and semiconductors.

If the material's dielectric function is too complicated to be fitted by the Lorentz model, the exact values of complex ϵ can be assigned for every frequency, but then simulation is carried for one frequency at a time.

FDTD has several disadvantages, one of which is a staircase surface discretization. The staircase discretization occurs when surfaces are not parallel to grid lines. Where two materials fall into the same grid cell, the refractive index of the more abundant one is assigned, and the smooth surface becomes stepped. The average of two refractive indices is often used, calculated using the effective medium approximations. Staircase surface discretization does not cause significant errors in dielectrics, as long as wavelength is significantly larger than the grid step (at least 20 times is usually sufficient). On metal surfaces however, simulations must be carried out with care, because plasmons are confined to the surface and therefore sensitive to its shape. One approach that is sometimes used to improve the resolution of FDTD method on such boundaries, hybridizes FDTD method with other methods using non-orthogonal computational grids. Finite volume or finite element methods, for example, can be employed in the vicinity of the metal surface. Solutions obtained in this sub-domain are then extrapolated to the boundary of FDTD grid. The second approach is to carry FDTD integration on non-uniform or conformal meshes. Non-uniform meshes have a variable grid step, and if this step is varied slowly in space, the overall accuracy will be high enough, as long as time step satisfies CFL condition for the smallest cell in domain [90]. In the conformal-mesh approach, cells containing metal boundary are subdivided into a finer grid. Because the time step on this sub-grid can be much smaller than that required in the rest of computational domain, the simulation here is carried separately with small time-steps and then extrapolated to the boundary of the course grid [17]. FDTD algorithms with non-rectangular adaptive grids were also proposed for more accurate surface treatment, and successfully employed in a number of research tasks [2].

An interesting variation of the FDTD method is a pseudo-spectral time-domain (PSTD) technique. It partially transfers the differential equations into a frequency domain, which allows one to treat large systems with relatively limited computational resources. In PSTD, instead of calculating spatial derivatives as finite differences one uses their Fourier transform. With only two grid cells per wavelength this method achieves similar accuracy to FDTD with 10 to 20 grid cells per wave-

length. Benefits of this method become less significant, however, when the feature size of the scattering body is comparable to the wavelength, because the grid step still has to be much smaller than the feature size.

1.4.2 FDFD Method

The FDFD method, like FDTD, uses finite differences to calculate spatial derivatives, but has the time-independent Helmholtz equation as an equation of state. This gives rise to an eigenvalue problem in the form $Ah = \left(\frac{\omega}{c}Bh\right)$ where h is a magnetic field eigenvector, A_{ij} is the matrix operator:

$$A_{ij} = \langle b_i | \hat{A}_{\vec{k}} | b_j \rangle, \quad (1.8)$$

$$\hat{A}_{\vec{k}} = \left(\vec{\nabla} + i\vec{k}\right) \times \frac{1}{\epsilon} \left(\vec{\nabla} + i\vec{k}\right) \times,$$

and $B_{ij} = \langle b_i | b_j \rangle$ forms an identity matrix, if basis functions $\langle b_i |$ and $| b_j \rangle$ are orthonormal. This problem is solved approximately, using a truncated set of basis functions and an iterative approach to find eigenvalues ω and eigenfunctions h . Eigenfrequencies attain a discrete set of values for a given wavevector \vec{k} , while the wavevector can be varied continuously [58]. Each eigenfrequency is characterized by an integer number n , and at a given n the function $\omega_n(\vec{k})$ is called n -th photonic band.

The FDFD method assumes periodic boundary conditions in all directions, and is suitable for photonic crystal analysis. It also requires a relatively small amount of computer memory, since the volume is limited to a single periodic cell. The computation expense is proportional to $[p \cdot i \cdot N \cdot \log(N)]$, where N is number of grid points, i is number of iterations used when solving matrix problem, and p is number of bands calculated. The number of photonic bands, similarly to the number of states in quantum mechanics, is infinite, but only a few of the lowest bands are usually calculated. In most periodic structures, practically useful band gaps appear within the first nine photonic bands. Band gaps between 1st and 2nd bands are usually considered in one-dimensional periodic structures, and 4th and 5th bands in square spiral photonic crystals and diamond and FCC lattices.

1.5 Finite-difference modelling in this work

FDTD and FDFD methods were used extensively in the present work for the following reasons. GLAD films form either periodic or random column arrangements, and often are also periodic in the vertical dimension (normal to the substrate). While light transmission through the whole film would be an impossible task to calculate, in a periodic array only a single column needs to be considered in the FDTD method, and a single period of the 3D structure is sufficient to describe the photonic properties in FDFD. With current computer capabilities, many FDTD and FDFD simulations can be performed on desktop computers with only a few requiring more than 8GB of computer memory.

Random column arrays can be also simulated as periodic structures, if the light wavelength is much larger than the intercolumnar distance. At long wavelengths their optical response becomes similar to that of a uniform anisotropic material. The dielectric constant of this material may be a sophisticated function of column geometry, but it is invariant to the scale of the structure, and to the column distribution on the substrate. Indeed, if random columns are characterized by a dielectric tensor with diagonal values ϵ_1 , ϵ_2 and ϵ_3 , the same columns can be arranged into a periodic array that will yield the same dielectric tensor. Therefore two arrays can have an identical optical response as long as the column spacing is much smaller than wavelength.

A convenient way to represent random columns is a square lattice. Incident light is then treated as a linear combination of two orthogonal polarizations oriented along the lattice axis: $\vec{E} = \vec{e}_1 \vec{E}_{e_1} + \vec{e}_2 \vec{E}_{e_2}$, where \vec{e}_1 and \vec{e}_2 are unit vectors of the square lattice. The square lattice has the same column spacing in these two orthogonal directions, making it physically similar to the random column arrangement.

MPB (MIT Photonic Bands) and MEEP (MIT Electromagnetic Equation Propagation) open-source software were used for all FD simulations done in this work [94, 58]. This software developed in Massachusetts Institute of Technology currently incorporates a wide spectrum of abilities, including simulation of dispersive, anisotropic and nonlinear materials. It can be used in C or in Scheme programming environments, with the first one suitable for development tasks and the second one convenient in research. The packages carry a limited number of basic geometrical

objects and material models, which can be used as a base to create more complex structures.

For the work described here an in-house library of dispersive materials and columnar objects has been produced to cover the wide range of GLAD architectures. Dispersive materials were characterized by the Lorentz approximation:

$$\epsilon(\omega) = \epsilon_\infty - \frac{f_0 \omega_p^2}{\omega(\omega - j\gamma_0)} + \sum_{l=1}^k \frac{f_l \omega_p^2}{\omega_l^2 - \omega^2 + j\omega\gamma_l}, \quad (1.9)$$

where ϵ_∞ is a dielectric constant at $\omega \rightarrow \infty$, ω_p is plasma frequency and k is a number of Lorentzian relaxations with frequencies ω_l , strengths f_l , and lifetimes $1/\gamma_l$. Lorentz approximations for metals were taken from [99], while for silicon and titanium dioxide they were obtained using the experimental data from references [126] and [65].

FDFD was used to analyze the photonic band structure of periodic GLAD films, and at long wavelengths to calculate their effective dielectric tensor. FDFD method was also used to calculate the mode structure of periodic films with defects. In this case, a super-cell including both defect and the surrounding periodic film was considered.

The model of a GLAD film used in FDTD simulations is shown in Figure 1.9. The cell is periodic along the X and Y axes, with pitch P_x and P_y . Open boundary conditions are implemented along the Z axis through the PML layers. The domain is occupied by a stack of identical geometrical objects, each representing a single period of a GLAD film. A defect layer was often inserted between any of these periodic layers. Each periodic layer was constructed to satisfy column continuity across the film.

A plane wave source is placed normal to Z axis below the structure, and fields are collected in horizontal planes, above (transmittance) and below (reflectance) the film. When needed, a substrate was attached to the film and submerged into one of two PML layers, representing an infinitely thick layer of substrate material (which is usually thicker than the coherence length). Transmission and reflection are calculated by dividing the Fourier transforms of transmitted and reflected fields by the Fourier transform of a source field (measured in the absence of scattering structure).

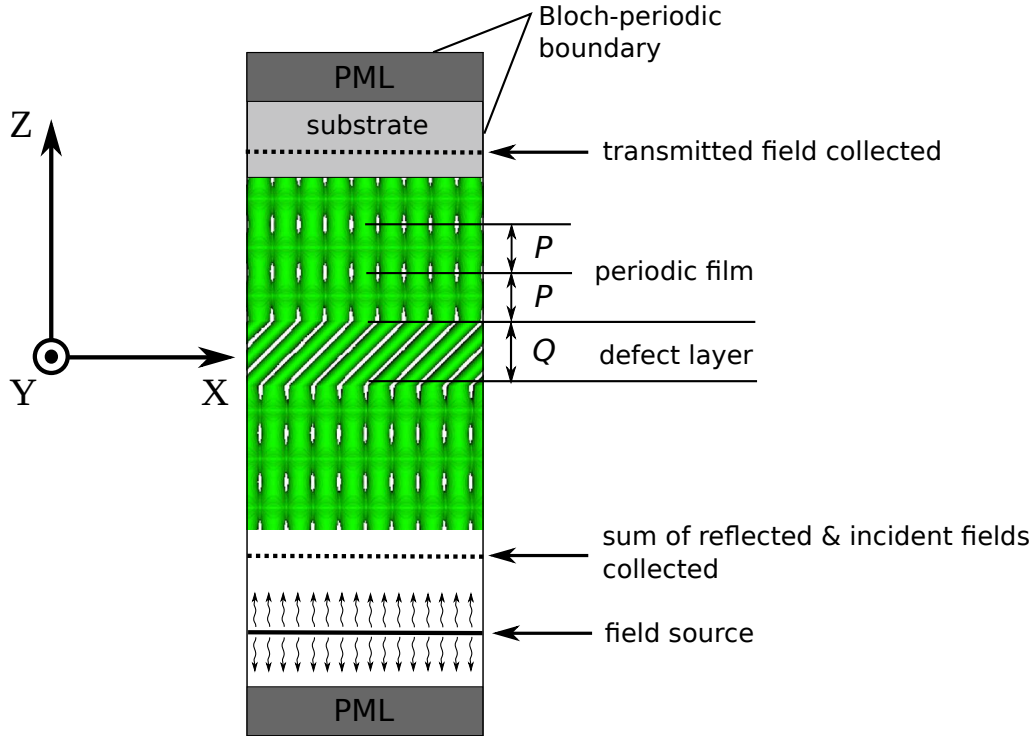


Figure 1.9: The structure of FDTD simulation domain used to model periodic columnar films.

If light is incident normally on the film, the wavevector \vec{k} is parallel to Z axis ($k_x = k_y = 0$), and multiple frequencies can be propagated simultaneously. The film is then illuminated by a Gaussian pulse:

$$E(t) = E_{max} \cdot e^{i\omega t + \phi_0} \cdot \frac{\Delta\omega}{\sqrt{(2\pi)^{3/2}}} e^{\Delta\omega^2(t-t_m)^2/(8\pi^2)}, \quad (1.10)$$

where ω is a centre frequency, $\Delta\omega$ is frequency dispersion, and t_m is a point of time when the pulse amplitude is at maximum. The value t_m has to be sufficiently high, so that source field at the beginning of simulation is negligibly small.

An obliquely incident plane wave can be generated by the source plane aligned normally to Z axis, if the complex phase of the wave is varied along the plane. For example for the plane wave with wavevector in the XZ plane at an angle γ with the Z axis, the electric field distribution on the source plane is: $\vec{E}(x, t) = \vec{E}_0 \sin(\omega t + \phi_0) \exp(ik_x x)$, where $\vec{E}_0 = \hat{x}E_p \cos(\gamma) + E_s \hat{y} + \hat{z}E_p \sin(\gamma)$. Here E_s and

E_p are the amplitudes of s and p polarized electric fields. Simulation is more time demanding at oblique incidence, because k_x or k_y are no longer equal to zero and only a single frequency can be simulated at a time. Oblique incidence simulations were also limited to closely packed thin columns of subwavelength sizes, because larger columns scatter light, so that k_x and k_y are no longer preserved.

	Finite-difference time-domain (FDTD)	Finite-difference frequency-domain (FDFD)
Simulation output	transmission and reflection spectra; field dynamics	dispersion relations; mode structure
Boundary conditions	open (PML) or Bloch-periodic	Bloch-periodic in all directions
Advantages	finite size and aperiodic structures can be simulated; directly related to the experimental data via transmittance and reflectance	computationally inexpensive and fast; effective dielectric properties are easily found from the slope of dispersion curve
Disadvantages	computationally expensive; maximum time step is limited by the CFL condition	not very useful for aperiodic structures and structures with defects; results do not directly relate to measured transmittance and reflectance

Table 1.1: Comparison of the FDTD and FDFD methods.

Comparison of the frequency-domain and time-domain methods is given in Table 1.1, outlining the advantages and disadvantages of each. In practice, periodic GLAD structures were often studied using both FDTD and FDFD methods to fully describe their optical properties. Simulations were carried using a high-end processing workstation with two dual-core AMD Opteron processors and 8GB of operating memory. A typical time-domain simulation, involving normal-incidence Gaussian pulse transmission through 3 μm long dielectric columns with 100 nm intercolumnar distance, lasted up to 5000 seconds, and occupied 1.4% of available memory at 5 nm spatial resolution. Simulations for obliquely incident light, resonant mode transmission, and dispersive materials were larger and longer, occupying up to 40% of memory and lasting more than one day in some cases. Frequency domain calculations consumed only a fraction of memory taken by time-domain simulations, and calculation times ranged from minutes to several hours, depending on the resolution and simulation tasks. Post-processing of the simulated data and accompanying analytical calculations for this thesis were performed in Octave [25], a specialized programming language for numerical computation, which is compatible with MATLAB.

1.6 Summary of the following chapters

The next two chapters - Chapter 2 and Chapter 3 will be devoted to the birefringent films formed by dense column arrays, where the intercolumnar distance is much smaller than the light wavelength. Such arrays often can be regarded as an effectively uniform but optically anisotropic slabs with the refractive index varied only in the direction normal to the film's surface. In Chapter 2, the film's birefringence is used to design nonabsorptive thin film polarizers, and in Chapter 3 we will see how optical anisotropy affects the angular response of the interference mirrors, and creates a path for the omnidirectional reflector design. Chapter 4 will address the optical performance of square spiral photonic crystals in the visible spectral range. The challenge of low refractive index contrast at these wavelengths will be addressed with geometry optimization, extending the knowledge already collected in literature. The rest of the thesis will be devoted to metal-dielectric composites based on the columnar structure of GLAD films. Ordered metal particles and the refractive index engineering will be discussed.

Chapter 2

Polarization selectivity in s-shaped columnar films ¹

2.1 Motivation

Optical anisotropy in GLAD films may arise due to their columnar structure, even when they are composed of an isotropic material. This anisotropy is expressed when the wavelength is substantially longer than the intercolumnar distance. The structure then behaves as an optically uniform, but anisotropic index-graded material. Because the anisotropy is structural, it can be manipulated during fabrication through changes in the column tilt, spatial orientation, and density. Such a degree of freedom is not available in naturally anisotropic materials, which are usually described by a fixed set of principal refractive indices, and a rather inflexible orientation of the optical axes in the crystal. Below we discuss the application of anisotropic GLAD films in the role of nonabsorptive polarizers.

Nonabsorptive polarizers are useful due to their ability to polarize light without loss, contrary to the polarizers based on selective absorption of light. Nonabsorptive polarizers are employed, for example, in high power laser systems, where even partial absorption may cause damage in the polarizing element. Traditionally they are implemented as reflective dielectric stacks, tilted at the Brewster angle to the incident beam [24]. Brewster stacks polarize in a wide spectral range, but have to be positioned at an angle to the beam, and therefore occupy relatively

¹A version of this chapter has been published in Ref. [74].

large space. Due to this tilt, they also can not be easily integrated in micro-optical devices. Thin film polarizers operating at normal incidence are, on the other hand, compatible with microfabrication, which enables their integration in optoelectronic devices. They are often designed as anisotropic interference mirrors [46], and as metal wire gratings [149]. Anisotropic interference mirrors, due to the film's anisotropy, have a polarization dependent refractive index profile. Their band gap position is, therefore, sensitive to the light polarization, making it possible to selectively reflect certain polarizations within a narrow spectral band. Among different fabrication approaches, the serial bideposition technique [46] has been used to make alternating layers of two anisotropic dielectrics. The anisotropy was achieved due to the porous columnar microstructure of the film. The method, however, involved multiple materials, which complicated the fabrication.

The GLAD technique uses more general substrate motion algorithm than serial bideposition and therefore allows one to vary anisotropy without changing the material. A single-material columnar film can be designed to selectively reflect light of one polarization and transmit the other one. The polarizing properties are achieved within the photonic band gap, and therefore the polarizer has a limited spectral width, similarly to the other interference-based thin film polarizers. The structure proposed and discussed here is composed of s-shaped dielectric columns. The film's refractive index and optical axis tilt are periodically varied by means of the variation of the column tilt. The whole film can be fabricated in a single deposition session and with only one evaporant source. Constant porosity is then maintained, making it easier to infiltrate the film with other materials, for example, liquid crystals [108].

The architecture of s-shaped columnar film is described by a number of variables, such as film density, column profile, and cross-section shape; therefore, the design is open to many possibilities. While the experimental analysis of all these possibilities may be lengthy and expensive, numerical simulation provides a fast and efficient way to do it. Finite-difference methods are well suited for this task because the analysis is focused on transmittance and reflectance from a planar film.

2.2 Theoretical model of s-shaped columnar polarizer

The planar nonabsorptive thin film polarizer is realized by a periodic variation of the column tilt along the film depth. It is known that the periodic refractive index variation gives rise to band gaps, where light is completely reflected. Here the band gap forms due to the optical axis tilt variation in the bianisotropic material (see Section 1.3 of Chapter 1). Column tilt can be varied either continuously or in discrete steps, with both ways having some advantages.

The discrete s-shape architecture realized by GLAD is shown on Figure 2.1. The film is composed of alternating layers A and B with different principal refractive indices and optical axes orientations. Layer A, formed by vertical posts, is uniaxial with optical axis parallel to Z axis. Its ordinary refractive index is in the substrate plane, and extraordinary index normal to it. Layer B is composed of slanted posts tilted in XZ plane. It is bianisotropic with one optical axis along Y axis and the other one in the XZ plane. Assuming that the column cross-section is constant and circular in both layers A and B, the effective index parallel to the Y axis will be nearly the same in these layers. Then light polarized along Y axis ($E_x = E_z = 0$) will be subjected to the same index n_o both in A and B sections, and will be transmitted without reflection. Light polarized along the X axis ($E_y = E_z = 0$) will be subjected to a variable refractive index, equal to n_o where the axis is vertical, and to $n_o < n' < n_e$, where the axis is tilted. Thus, the x-polarized light will experience multiple reflections leading to a photonic band gap.

Each vertical period of the film consists of a four layer sequence. Layers A and A' are vertical posts, and layers B and B' are slanted posts tilted in the XZ plane. To ensure that the average column growth is vertical, the tilt direction in sections B and B' is opposite. Layers A and A', in turn, are identical. The column geometry is characterized by the height of vertical posts h_v and slanted posts h_t , and by the slanted post tilt β' . The column's vertical pitch is defined as $P = 2(h_t + h_v)$. In the following discussion the column profile will be specified in the terms of pitch P and the ratio $\eta = h_t/P = h_t/(h_v + h_t)$, rather than in terms of heights h_v and h_t . The angle β' is closely related to the deposition angle, and can be varied by a spin-pause technique without influencing the mean film's density [103].

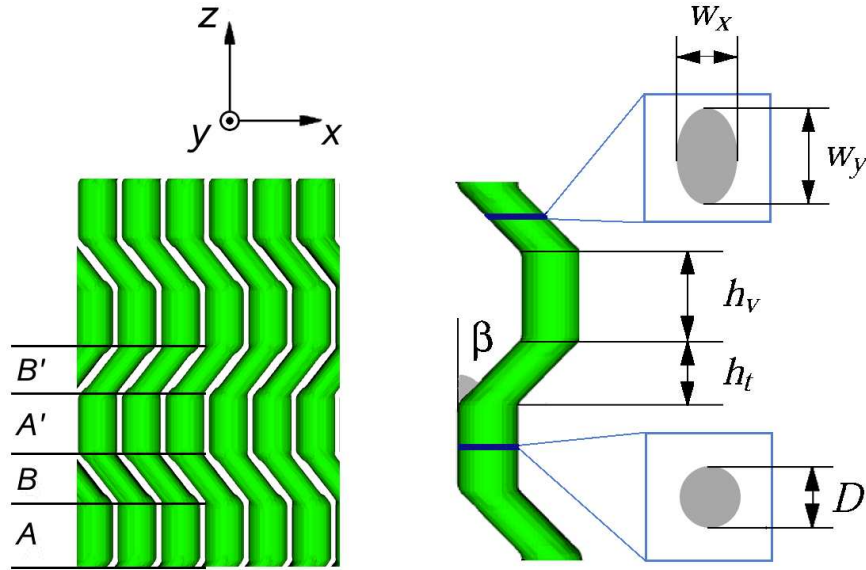


Figure 2.1: The model of the s-shaped columnar film.

Columns in the layers A/A' and B/B' have different horizontal cross-sections. In the vertical segments the cross-section is approximately circular in a substrate plane, because these segments are fabricated at a fast continuous substrate rotation, and are therefore rotationally symmetric. The column cross-section in tilted segments has been approximated as elliptical in the substrate plane. Because the columns are tilted in the XZ plane the major axes of ellipses are oriented along X and Y axis, and characterized by two widths w_x and w_y . Again, in the following discussion, instead of using the absolute values for these widths, the ratio $e = (w_y - w_x)/D$ will be used, where D is a diameter of a circle with surface area $S = \pi D^2 = \pi w_x w_y / 4$. The area S is constant throughout the film assuming that the deposition angle is not changed, and there is no column extinction and broadening due to competition in their growth. Due to rotational symmetry, in the vertical sections A/A' the cross-section is circular: $w_x = w_y = D$. In the tilted sections, due to the lack of shadowing along Y-axis, column cross-sections are elongated in Y-direction and the relation $w_y > w_x$ usually holds. By modifying the substrate motion algorithm, for example, with the PhiSweep technique, this relation can be reversed, therefore both positive and negative values of e were

considered.

Based on SEM image analysis, fabricated s-shaped TiO₂ columns formed random arrays with an average intercolumnar distance close to 60 nm and average column diameter slightly less than 55 nm. Close column spacing allowed us to model these films as an ordered rectangular array of columns, since the wavelength of interest (in the visible range) is much larger than the intercolumnar distance. The structure was simulated as a square array, with lattice constant $a = 60$ nm. Because the effective medium optical properties are scale invariant, the exact value of a is not important and only the material to void fraction $f = S/a^2$ has to be known. The simulated film is thus characterized by a vertical pitch P , fraction of tilted segments η , cross-section elongation in tilted segments e , slanted post tilt β' , column volume filling f , and material refractive index $n = 2.4$, corresponding to the electron beam evaporated titanium dioxide. In practice, the TiO₂ refractive index varies with wavelength (increasing on a blue side) and depends on the crystalline structure [65]. Rutile form has the highest index ranging from $n \approx 2.65$ to $n \approx 3.0$ across the visible spectrum, and anatase form has the index ranging from $n \approx 2.5$ to $n \approx 2.9$. Electron beam evaporated material has somewhat lower index values, ranging from $n \approx 2.25$ to $n \approx 2.65$, due to the presence of voids in it. Annealing brings it closer to the anatase, and we chose the value in-between to account for the voids that possibly remain after annealing. The material was treated as nondispersive, because the refractive index variation across the typical band gap (less than 30% of the centre wavelength) is relatively small. Also we considered it nonabsorptive, since any significant absorption starts at wavelengths smaller than 350 nm, in the ultraviolet, and films were designed for the visible range. Therefore with the transmission T calculated in the simulation, the reflection was determined as $R = 1 - T$.

Due to the periodic column arrangement, Bloch periodic boundary conditions were used in FDTD for the X and Y directions, and open boundary conditions (PML layers) in Z direction. In frequency domain calculations, the computational cell was 3D periodic with the size in Z and X/Y dimensions equal to P and a respectively. The resolution of the Yee grid was increased until no further significant transmittance change was observed, and eventually the grid step $\Delta = a/32 = 1.875$ nm was chosen for all calculations.

2.3 Optical properties of s-shaped films and polarizer design

The structure's symmetry determines symmetries of the electromagnetic modes it carries. Discrete translational symmetry, for example, is responsible for the band gap formation while continuous translational symmetry leads to a continuous light transmission. S-shaped columns have mirror symmetry with respect to the XZ plane (plane of the column tilt), which is responsible for polarization dependence of their optical response. The electromagnetic modes can be split in two orthogonal polarization states: one with the electric vector oscillating in the XZ plane, and the other with the electric vector aligned along the Y axis. Considering normally incident light, where the vector \vec{k} is parallel to the Z axis we can treat light as a superposition of x-polarized and y-polarized orthogonal modes. It is important that the intercolumnar distance in the film is much smaller than the light wavelength. While in three-dimensional photonic crystals, where column separation is comparable to the wavelength and the mirror plane can be placed only in a discrete number of points, densely spaced s-shaped columns have mirror symmetry in a continuum of points along Y-axis. X and y-polarized transmittances were considered and the polarization dependent band gaps were sought.

FDFD calculations were carried for column geometries similar to those experimentally realized. The starting model was chosen with pitch $P = 295$ nm, $\eta = 1/2$, volume filling $f = 64\%$, slanted post tilt $\beta' = 30^\circ$, and circular cross-section ($e = 0$) throughout the film depth. The band gap of interest is located between the second and third photonic bands, because the layers B and B' are optically identical at normal incidence, and effectively one pitch P contains two sub-pitches AB and A'B'. Band gap edges are, therefore, determined as the highest frequency of the second photonic band $\omega_2(k)$ and lowest frequency of the third photonic band $\omega_3(k)$ respectively (see Section 1.4.2 for definition of photonic band and method of calculation). Figure 2.2 shows the band gap edges for x and y-polarized band gaps as a function of column tilt β' . At $\beta' = 0$ the band gap is absent regardless of the polarization, because the whole column is a vertical post, lacking the refractive index variation. At increasing angles, the x-polarized band gap appears, but the y-polarized band gap remains closed because the effective refractive index for y-polarized light is the same in vertical and in tilted segments. The x-polarized band

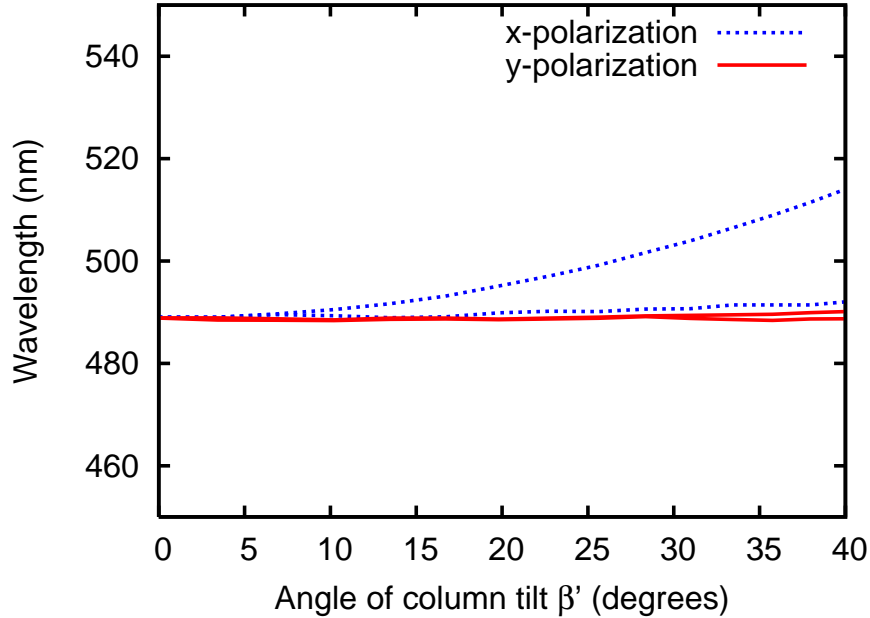


Figure 2.2: FDFD calculated location of the band gap edges as a function of slanted post tilt in s-shaped columns (column horizontal cross-section is circular in all segments).

gap also redshifts slightly, indicating that the average refractive index experienced by x-polarized light increases.

The result is different when cross-section anisotropy is taken into account. Band gap edges are shown on Figure 2.3 for the structure with a Y-elongated cross-section in tilted segments ($e = 0.167$). Both x- and y-polarized band gaps exist even at $\beta' = 0$, because of the column cross-section variation between segments A and B. The y-polarized band gap weakly depends on β' , since changing the tilt does not change the Y component of the effective refractive index. The x-polarized band gap, however, decreases with growing β' , and vanishes at $\beta' \approx 30^\circ$. At larger angles, the x-polarized band gap reappears again.

The collapse of the x-polarized band gap is caused by the competitive influence of the two anisotropy sources. A structural anisotropy is expressed in the column tilt, and a cross-sectional anisotropy is expressed in the cross-section elongation. Increasing column tilt leads to an increase of the x-polarized refractive index in the tilted segments. The larger the difference, the wider the band gap becomes. Cross-

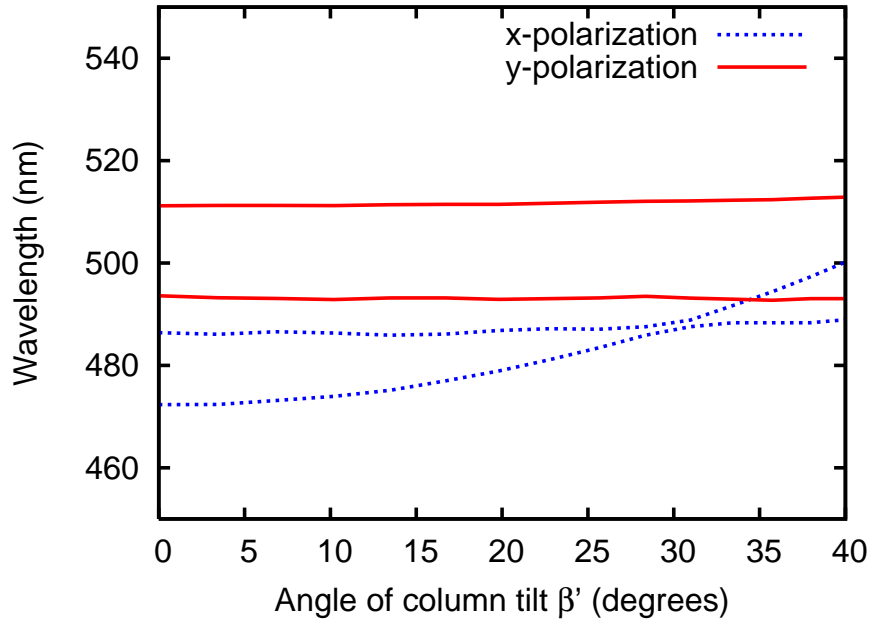


Figure 2.3: FDFD calculated location of the band gap edges as a function of slanted post tilt in s-shaped columns (column horizontal cross-section is elongated in slanted post segments with $e = 0.167$).

section broadening in the Y direction has the opposite effect, because it makes the film more porous in the X direction and denser in the Y direction. This lowers the x-polarized refractive index in the tilted segments. The counteracting influence of the column tilt and cross-section broadening thus suppresses the x-polarized band gap for a certain combination of these parameters. Figure 2.4 shows the cross-section broadening needed to suppress the x-polarized band gap as a function of β' .

While structural and cross-sectional anisotropies act competitively when the cross-section is elongated along the Y axis, their influence becomes synergistic when the cross-section is broadened along X. Figure 2.5 shows the x- and y-polarized band gap edges as a function of cross-section broadening for both negative and positive e values. As expected, the x-polarized band gap gradually widens in the negative domain of e values. The y-polarized band gap disappears only at $e = 0$ and steadily increases with both positive and negative cross-section elongations. Spectral positions of the x- and y-polarized band gaps have the opposite trends.

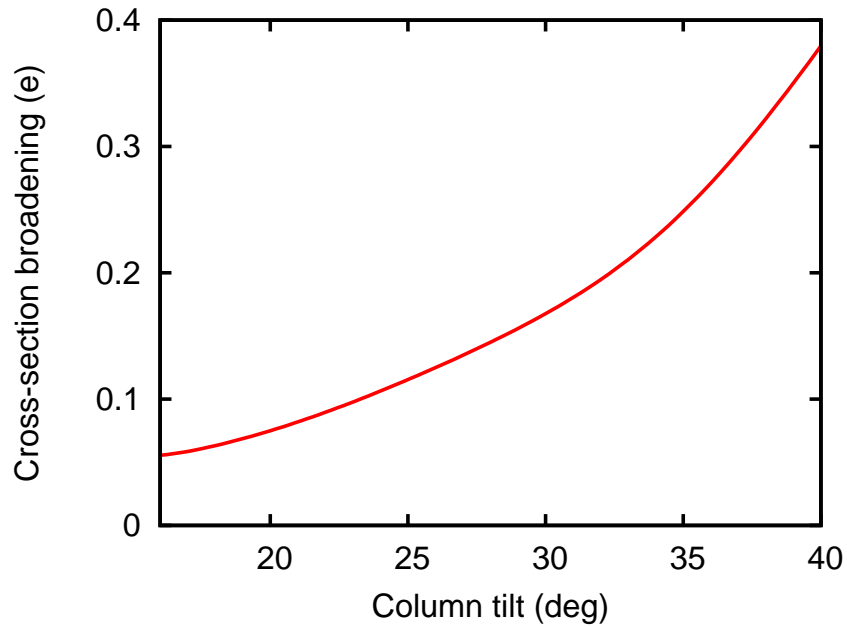


Figure 2.4: Relation between the cross-section broadening e , needed to close the x-polarized band gap, and slanted segment tilt β'

The x-polarized band gap blueshifts with increasing e indicating that the film, on average, becomes more porous in X direction. The y-polarized band gap redshifts, because the average amount of voids in the y-direction decreases.

The competitive effects of the two kinds of form anisotropy and band gaps spectral shift create three distinct design opportunities for the narrow band non-absorptive polarizers. The option which is the easiest to fabricate, labelled as (III) on Figure 2.5 exploits the cross-section broadening along Y axis to suppress the x-polarized band gap, and achieve polarization selective transmittance. Due to the lack of shadowing in the direction normal to the deposition plane, GLAD columns naturally tend to broaden in this direction. Therefore no special substrate motion techniques need to be employed to achieve this cross-section shape. Figure 2.6 shows the FDTD simulated transmission spectra and normalized Stokes parameters $s_1 = S_1/S_0$ and $s_3 = S_3/S_0$ for the x- and y-polarized light passing through 20 periods of s-shaped columnar structure with cross-section elongation $e = 0.17$. Stokes parameters S_0 to S_4 were calculated for the 45° polarized incident light to show the polarizing strength of the film, and phase retardation between the x- and

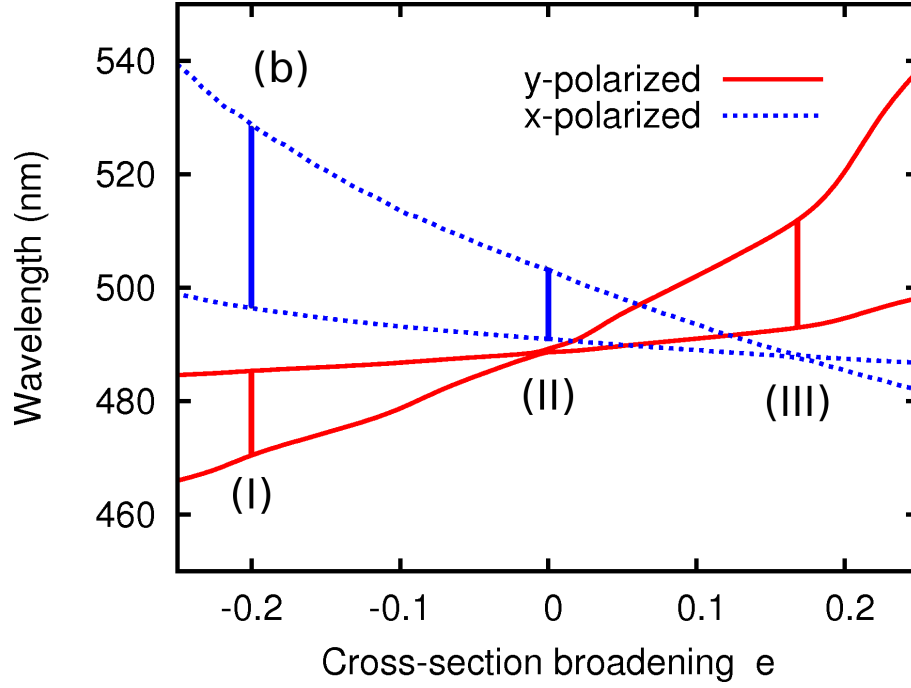


Figure 2.5: FDFD calculated location of the band gap edges as a function of cross-section broadening e ($P = 295$ nm; $\beta' = 30^\circ$; $\eta = 0.5$; $f = 64\%$; $n = 2.4$).

y-polarized beams. Stokes parameters are defined as:

$$S_0 = |E_x|^2 + |E_y|^2,$$

$$S_1 = |E_x|^2 - |E_y|^2,$$

$$S_2 = 2 \Re(E_x E_y^*),$$

$$S_3 = 2 \Im(E_x E_y^*),$$

where E_x and E_y are the field intensities of x- and y-polarized light. The S_0 is the intensity, and since we are interested only in the relative intensities, it is convenient to divide all other parameters by S_0 . The S_1 represents the degree of linear polarization with the value $s_1 = S_1/S_0 = 1$ corresponding to entirely x-polarized light, and $s_1 = -1$ corresponding to y-polarized light. The parameter S_3 shows the degree of circular polarization in the transmitted light and for a 45° polarized incident beam, it shows the phase difference between the two orthogonal

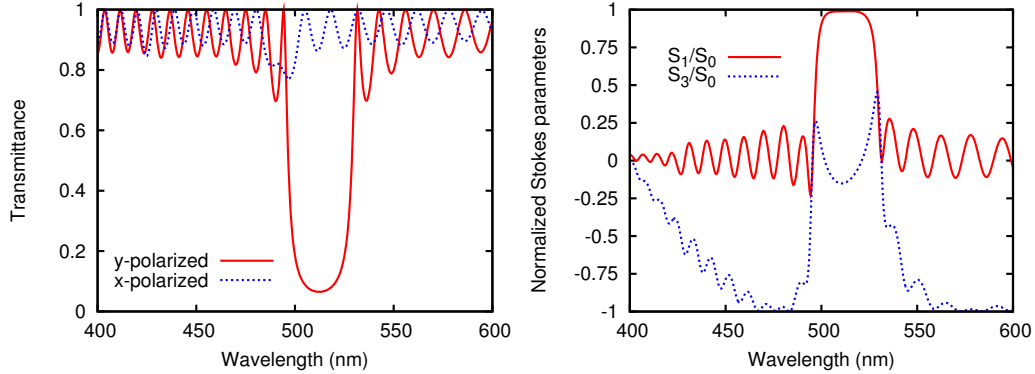


Figure 2.6: FDTD simulated transmittance (left) and Stokes parameters (right) for 20 periods of the s-shaped columns with $e = 0.15$ and all other parameters same as on Figure 2.5 (design option III).

polarizations on the transmitted side.

We can see on the figure that the y-polarized band gap is centered around 510 nm, and is strong enough to reflect close to 95% of the light, but the x-polarized spectrum has only a very slight dip, marking the location of the vanishing x-polarized band gap. The x-polarized transmittance is relatively constant and slightly below unity due to the reflection loss on the film surface. Stokes parameters show the normalized selective transmittance (s_1) and the degree of elliptical polarization of the transmitted light (s_3). The graph shows that the film acts as a narrow band polarizer with high x-polarized transmittance $s_x > 0.95$ in the band $501 < \lambda < 523$ nm, and $s_x > 0.98$ within $504 < \lambda < 520$ nm.

The second option, labelled (II), uses a constant circular cross-section throughout the film, in which case the y-polarized band gap does not form. Slight blueshift of the x-polarized band gap further favours high polarizing ability of the film. Figure 2.7 shows the transmittances and Stokes parameters for isotropic cross-section $e = 0$. The reflection in the x-polarized band gap centre exceeds 95%, while the y-polarized band gap is vanishingly small. The Stokes parameters show the presence of the y-polarized transmittance band with a selective transmittance $s_y = -s_1 > 0.98$ in the band $500 < \lambda < 523$ nm.

The last option, labelled as (I), exploits cross-section broadening in the deposition plane, leading to two separated polarizing bands (Figure 2.8). The band located on the red side selectively reflects x-polarized light, while the band lo-

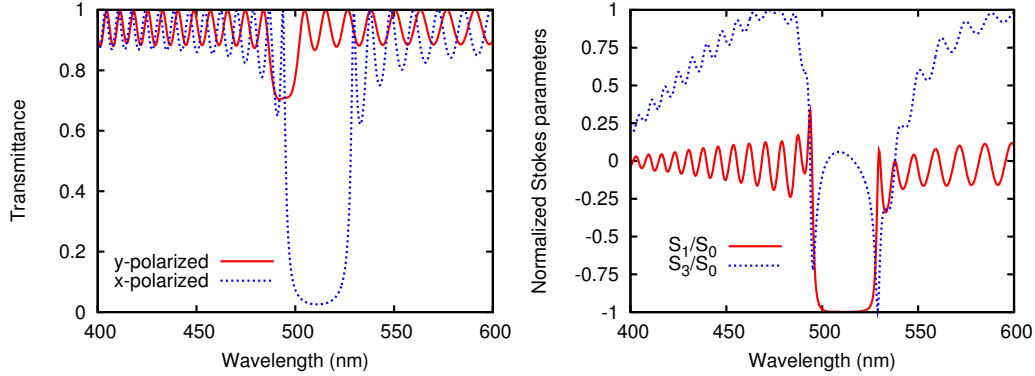


Figure 2.7: FDTD simulated transmittance (left) and Stokes parameters (right) for 20 periods of the s-shaped columns with $e = 0$ and all other parameters same as in Figure 2.5 (design option II).

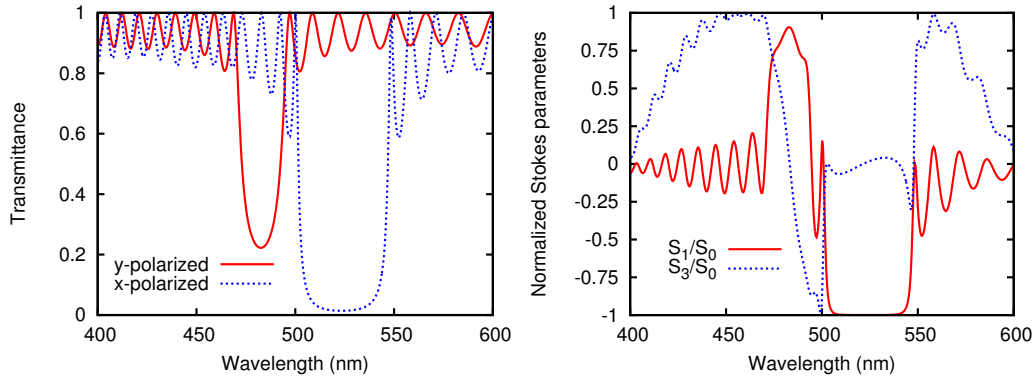


Figure 2.8: FDTD simulated transmittance (left) and Stokes parameters (right) for 20 periods of the s-shaped columns with $e = -0.2$ and all other parameters the same as on Figure 2.5 (design option I).

cated on the blue side reflects y-polarized light. The transmission spectrum and Stokes parameters are shown for 25 periods of film with cross-section elongation $e = -0.17$. We can see that two band gaps of the opposite polarization exist and are completely separated. The y-polarized band gap is smaller than the x-polarized one, and transmitted light is not completely polarized in this band ($s_1 < +1$) at a given film thickness of 20 periods. A larger number of vertical pitches will increase the x-polarized band gap strength. This design option is the most challenging for fabrication, since current versions of PhiSweep method are barely capable of

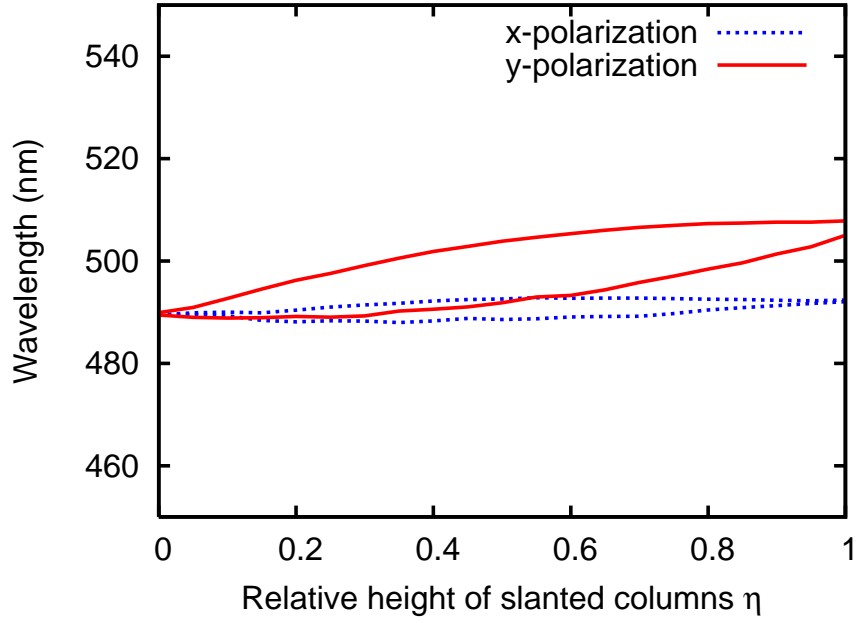


Figure 2.9: FDFD calculated location of the band gap edges as a function of slanted post fraction η ($P = 295$ nm; $\beta' = 30^\circ$; $e = 0.11$; $f = 64\%$; $n = 2.4$)

bringing the e value below zero. This option is interesting, however, because two polarizing bands exist simultaneously for the opposite polarization states.

The polarizing ability of the filter is maximized when (a) one of the two band gaps closes or band gaps are completely separated, and (b) the spectral width of the remaining band gap is large. One more parameter that is easily changed besides column tilt and cross-section shape is the fraction of tilted segments η . Figure 2.9 shows the FDFD calculated positions of the band gap edges as a function of parameter η for the film with pitch $P = 295$ nm, tilt $\beta' = 30^\circ$, cross-section anisotropy $e = 0.11$, and volume filling $f = 64\%$. Both x- and y-polarized band gap widths are largest when $\eta \approx 0.5$, favouring the structure with equal fractions of vertical and tilted segments. However, the bands separate more spectrally as the η increases, therefore values of η slightly larger than $\eta = 0.5$ may be optimal for fabrication.

2.4 Experimental realization and measured data

The experimental part of this work has been done by Nicholas Wakefield at the University of Alberta Nanofabrication Facility. The discrete s-shape structure was realized with the following substrate motion algorithm. Each vertical column segment of columns was deposited at a constant substrate rotation $\phi(t) = \omega t + \phi_0$. Film thickness was monitored by a quartz crystal microbalance and the rotation speed was computer controlled to maintain a vertical growth speed at 5 nm per one substrate rotation. During the deposition of tilted segments, the substrate rotation was stopped completely to maximize the structural anisotropy of the film.

Titanium dioxide films were deposited using reactive e-beam evaporation at elevated oxygen pressures ranging from 8 mPa to 12 mPa. Films were deposited on silicon substrates for the structural characterization with SEM, and on glass substrates for the optical characterization. A series of s-shaped films, 6 pitches each, were fabricated at the deposition angles ranging from $\alpha = 60^\circ$ to 83° . The vertical post height was equal to the height of slanted post segments ($\eta = 0.5$). Deposition angles between 70° and 75° yielded the highest polarization selectivity, therefore angle $\alpha = 70^\circ$ was chosen for subsequent depositions. This angle gives a column tilt $\beta' = \beta = 36^\circ$ according to equation (1.1) and tilt close to 30° was measured on the SEM images.

A set of fourteen films was prepared with number N of s-bends ranging from 2 to 30. Each film's transmission was measured and the normalized selective transmittance s_1 was calculated for the band gap centre as $\frac{T_x - T_y}{T_x + T_y}$. The SEM image of the fabricated film is given in the Figure 2.10.

Figure 2.11 shows the experimentally measured and simulated transmittances for the 25-period discrete s-shaped film. The geometrical parameters for the simulation were determined from the SEM image and adjusted by fitting the simulated spectra to the experimental. Vertical pitch was determined from SEM $P = 295$ nm, as well as the tilt $\beta' = 30^\circ$. Film density and cross-section shape could not be determined from the SEM data, and were found by comparing simulated and experimentally measured transmittances: $e = 0.18$ and $f = 63.6\%$. With this column geometry the experimentally measured spectra are in a good agreement with the simulated: both in simulation and in the experiment the y-polarized band gap is centered at $\lambda \approx 510$ nm, and a much narrower and weaker x-polarized band gap

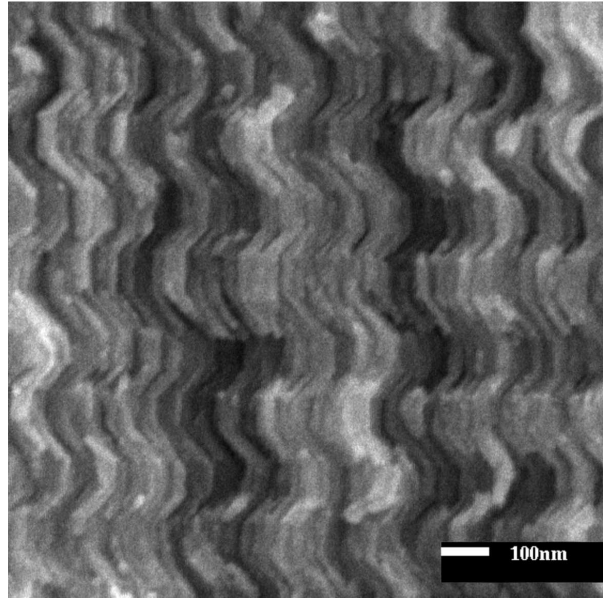


Figure 2.10: SEM photograph the s-shape columnar film (courtesy of Nicholas Wakefield).

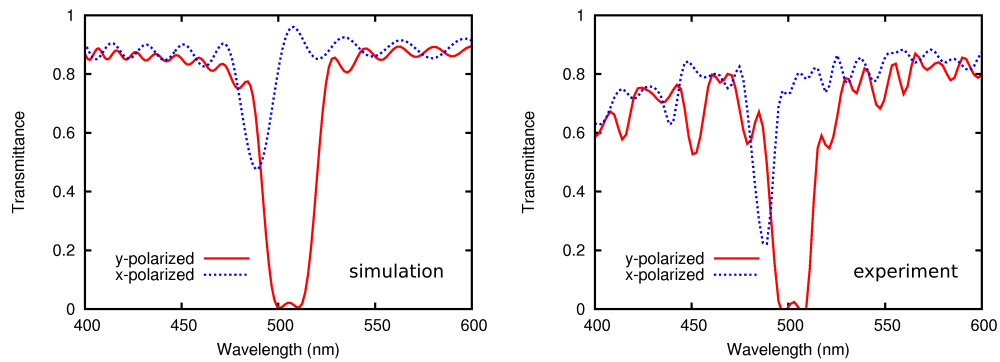


Figure 2.11: FDTD simulated (left) and experimental (right) transmission spectra for the experimentally realized film ($P = 295$ nm; $\beta' = 33^\circ$; $e = 0.184$; $f = 64\%$; $n = 2.4$).

is at ≈ 490 nm. Measured transmission decreases at $\lambda < 450$ nm, not in agreement with the predictions. Because the absorption coefficient of titanium dioxide at wavelengths larger than ~ 400 nm is vanishingly small [65], this decrease can be attributed to the increasing scattering loss at shorter wavelengths. Scattering occurs on irregularities of film density, resulting from the randomness of column

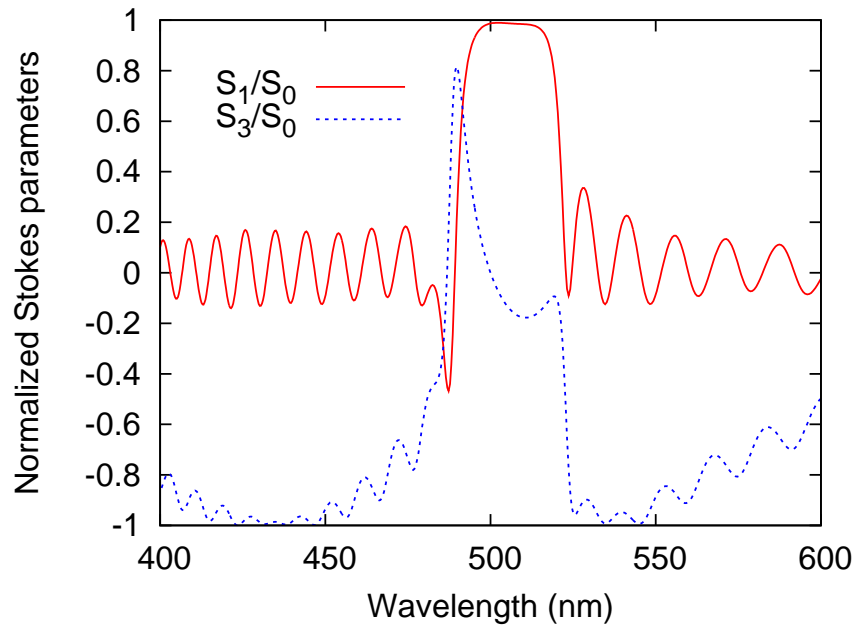


Figure 2.12: FDTD simulated Stokes parameters s_1 and s_3 for the experimentally realized film.

distribution on the substrate and from any geometrical deviations of the individual columns. Scattering loss is not substantial at the band gap wavelength of the fabricated film, but it may have to be taken into account in films with larger intercolumnar distance or at shorter wavelengths.

On Figure 2.12, FDTD simulated Stokes parameters are given for the experimentally realized film showing high polarization selectivity, with $s_1 \rightarrow 1$. The x-polarized band gap is blueshifted relative to the y-polarized band gap, and lays almost entirely outside of it.

Due to the relatively low refractive index contrast in the s-shape columns (which is due the variation of film anisotropy, rather than density), a large number of vertical periods is needed to achieve high reflection in the band gap. Fourteen films were fabricated with the numbers of vertical pitches ranging from $N = 2$ to $N = 30$, and Figure 2.13 shows the normalized selective transmittance as a function of number of periods in the discrete s-shape film with the experimentally realized architecture. Dots with error bars show the measured selective transmittance and the dotted line gives the FDTD simulated result for the centre of the y-polarized

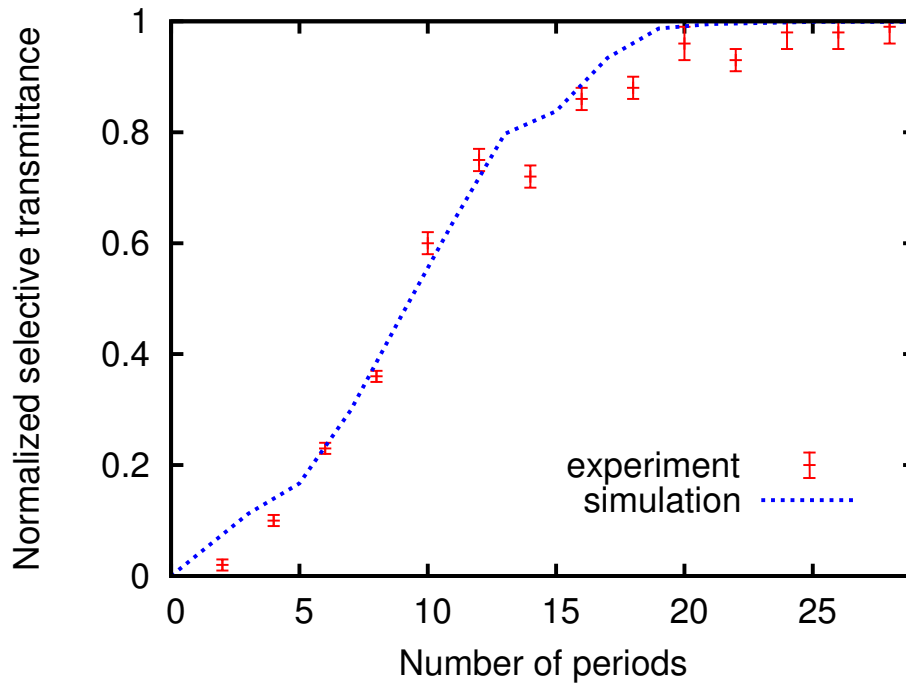


Figure 2.13: Normalized selective transmittance s_1 of the experimentally realized s-shaped film as a function of number of periods, measured and simulated at $\lambda = 515$ nm.

band gap. Computational error in the simulated graph at $N < 5$ is most probably due to the truncation of time series of the collected field amplitudes. While at sufficiently large N the transmission photonic band gap dominates the spectrum at a given wavelength, with small N the transmission spectrum is governed by Fabry-Perot resonance. Truncating the simulation in time limits the number of reflections that can be captured in Fabry-Perot resonance.

According to Figure 2.13, at least nine periods of the s-shape profile are needed to get polarization selectivity larger than $s_1 = 0.5$, but at more than 20 periods the transmitted light is almost completely polarized. With the vertical pitch of 295 nm, this results in a total film thickness close to $6 \mu\text{m}$.

The usefulness of the polarizing film has to be also judged in terms of its optical response as a function of the incidence angle. The band gaps of interference mirrors are known to blueshift with the increasing angle of incidence, and this limits their application to narrow-angle beams. Figure 2.14 shows FDFD calculated x- and

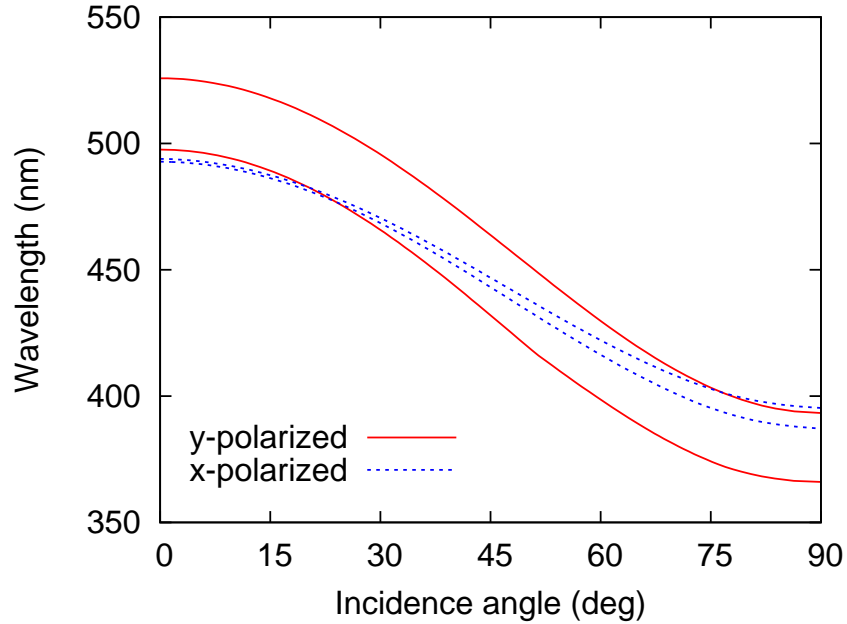


Figure 2.14: FDFD calculated location of the band gap edges as a function of incidence angle for the s-shaped columnar film realized in the experiment. The XZ plane is an incidence plane and the incidence angle is measured from the Z axis.

y-polarized band gap positions for the experimentally realized film as a function of incidence angle. Both band gaps blueshift by ~ 100 nm between $i = 0^\circ$ and $i = 90^\circ$, and the x-polarized band gap falls within the y-polarized one at incidence angles $i > 19^\circ$. However, at least up to $i = 30^\circ$ it stays close to the edge of the y-polarized band gap. The red edge of y-polarized band gap blueshifts, and coincides with the corresponding normal incidence blue edge at $i = 29^\circ$. This means that the polarizer can be used for a beam up to 58° wide, if the beam is a single frequency mode.

2.5 Continuous s-shape

In continuous s-shaped columns, shown in Figure 2.15, the column tilt is varied gradually as a function of the vertical coordinate. This column architecture has both advantages and disadvantages, compared to the discretely bent one. Fabrication of continuously bent columns is obviously more complicated than that of a

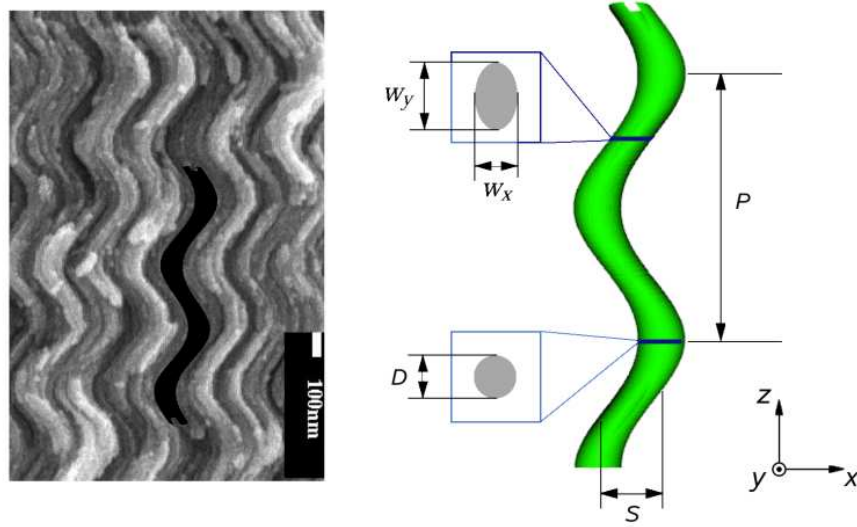


Figure 2.15: SEM image and theoretical model for the continuous s-shaped columns.

discrete shape, while the polarizing properties might not be better. The continuous architecture, however, does not have a discontinuity in the refractive index profile, and therefore may produce less diffuse light scattering by having fewer defects. Indeed, abrupt changes in the substrate motion pattern during the discrete s-shape deposition might cause splitting and merging among some of the adjacent columns, though these effects were not studied experimentally. Fabrication of continuous s-shape columns involves a spin-pause substrate motion algorithm.

The model approximated the column profile as sinusoidal with swing S , and period (pitch) P . The column's horizontal cross-section varies continuously along the column length, becoming circular at points where column is vertical, and maximally elongated where the column tilt is highest. Since the relation between column tilt and cross-section is complex and poorly studied, in the model the broadening e was assumed to vary harmonically along the vertical coordinate, with pitch equal to $P/2$. The maximum cross-sectional anisotropy e_m is observed at points of the maximum column tilt, and the minimum is $e = 0$.

Figure 2.16 gives the FDTD simulated and measured transmittances for six periods of continuous s-shaped columns with vertical pitch $P = 510$ nm, arm swing $S = 60$ nm, cross-sectional anisotropy $e_m = 0.22$, and material to void

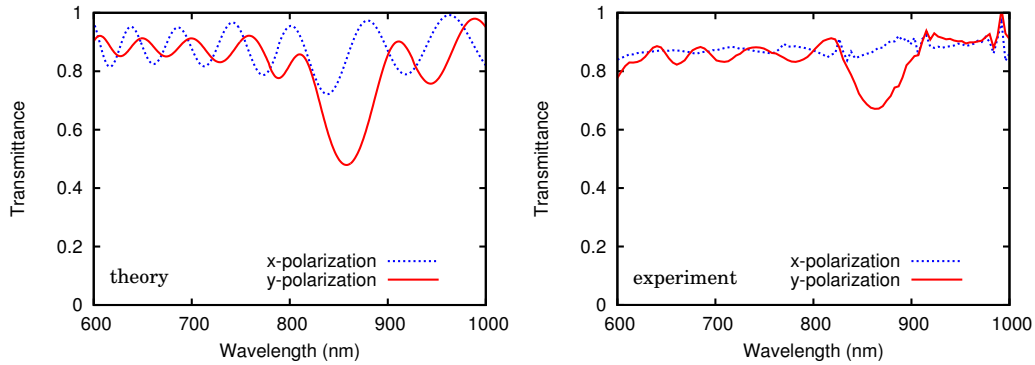


Figure 2.16: FDTD simulated (left) and experimentally measured (right) transmission spectra for the continuous s-shape film. The film parameters used in the simulation are: $P = 510$ nm; $S = 60$ nm; $e_m = 0.22$; $f = 62\%$.

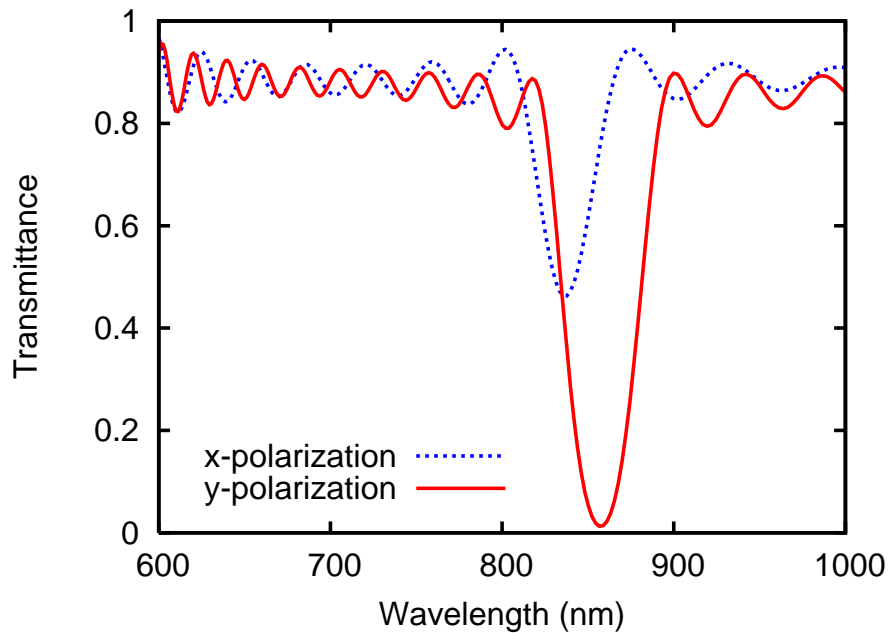


Figure 2.17: FDTD simulated transmission spectra for the the same geometry as in Figure 2.16, but with 19 vertical periods.

ratio $f = 62\%$. Pitch and arm swing were found from SEM images, while cross-section anisotropy and film density were determined by comparing simulated spectra with the experimentally measured one. The optical response of continuously bent columns is qualitatively the same as the one of the discretely bent columns.

The x-polarized band gap is suppressed due to the competitive influence of structural and cross-sectional anisotropies because the cross-section is broadened in YZ plane. The y-polarized band gap is redshifted relative to the x-polarized one and is substantially stronger. As shown in Figure 2.17, at a large number of s-shaped periods ($N = 19$), the y-polarized band gap is slightly weaker than the one of the discrete s-shape, because of the lower variance (r.m.s. deviation from average) of the refractive index in the continuously bent s-shaped film.

A summary of the column geometries considered in the discussion above is presented in Table 3.2.

	P (nm)	e	f (%)	β' (deg.)	Swing (nm)
Model I	295	-0.2	64	30	-
Model II	295	0	64	30	-
Model III	295	0.15	64	30	-
Experiment - discrete	295	0.184	64	33	-
Experiment - continuous	510	0.22	62	-	60

Table 2.1: Simulated parameters for the designed and fabricated geometries of s-shaped polarizers.

2.6 Liquid crystals in polarizing film: polarizing switch

Porous thin film polarizing elements fabricated by GLAD may be electronically switched when filled with liquid crystals [108, 134]. Liquid crystals (LC) share the fluidity of liquids with the crystalline organization that depends on the external conditions. LC molecules transition from the ordered to randomly oriented states under the influence of temperature, concentration, or external fields. When in the organized state, they form an anisotropic material.

As we have seen above, the columnar thin film has distinct polarizing properties on its own. After infiltrating this film with liquid crystal, these polarizing properties can be further tuned by the external field. As the LC is switched between random and ordered states, the film anisotropy can be either enhanced or suppressed.

Consider the discrete s-shape columns filled with a liquid crystal. One common LC that can be used for this purpose is the E7 mixture, made of cyanobiphenyl molecules with long aliphatic tails. In the addressed state, this material is uniaxi-

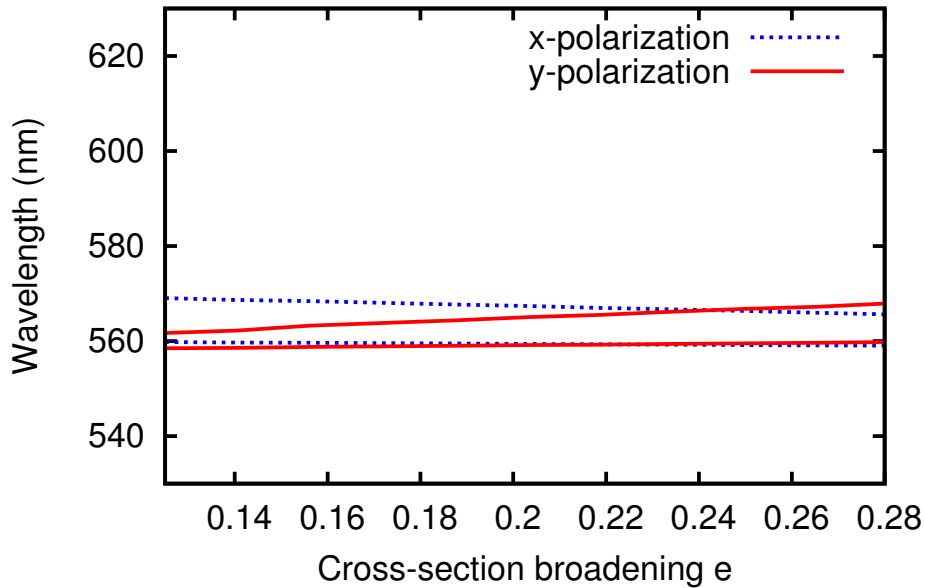


Figure 2.18: FDFD calculated location of the band gap edges as a function of cross-section broadening for the discrete s-shaped columns infiltrated with E7 liquid crystal. Crystal molecules are aligned along the columns and the column geometry is defined by: $P = 288$ nm; $\beta' = 35^\circ$; $\eta = 0.5$; $e = 0.17$; $f = 50\%$; $n = 2.5$.

ally anisotropic with ordinary and extraordinary indices $n_o = 1.52$ and $n_e = 1.75$ respectively. In the absence of the external field, LC alignment in GLAD films depends on the type of the columnar structure [135]. For slanted posts, LC alignment is preferentially along the columns, but if their cross-section is highly broadened, and the columns form a ribbon-like structure, LC molecules align along the grooves between ribbons. Because s-shaped columns have a moderate cross-section broadening and do not form nanoribbons, we can assume that LC molecules conform to the s-shaped profile in the absence of the field, aligning parallel to the columns axes.

When an electric field is applied, this alignment is switched depending on the field direction. Polarized chains of LC molecules form the optical axis along the electric field lines, and have an extraordinary refractive index in this direction. For example, if the field is aligned along the Z axis, the latter becomes an extraordinary axis for the LC, and the ordinary index is observed in the substrate plane.

FD simulations revealed interesting properties of the LC filled film. When an X or Y field is applied, the film presents two separated polarizing bands, and as

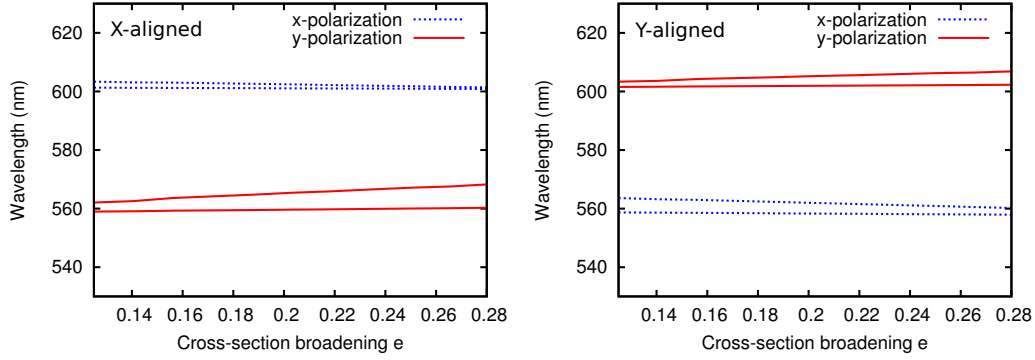


Figure 2.19: FDFD calculated location of the band gap edges as a function of cross-section broadening for the same structure as on Figure 2.18, and liquid crystal (extraordinary index) aligned along X axis (left) and Y axis (right).

the field is switched between these two directions, the polarizing state changes to the opposite. Figure 2.18 shows the x- and y-polarized band gaps as functions of cross-section broadening e for discrete s-shape film with E7 liquid crystal aligned along the columns. The column geometry is defined by pitch $P = 288$ nm, tilt $\beta' = 35^\circ$, tilted segment fraction $\eta = 0.5$, column refractive index $n = 2.5$, and column material fraction in the film $f = 50\%$. Compared to the air filled columns, discussed before, the effect of cross-section broadening is weak in the LC filled film. X-polarized band gap still slightly decreases in width as the cross-section broadens along Y axis, but not as much as without the LC. Furthermore, the y-polarized band gap is now sensitive to the cross-section geometry, because the material surrounding the column is no longer isotropic. Both band gaps are relatively narrow and both are centered at about the same wavelength.

Qualitative change occurs when the field is applied in X or in Y direction, as shown on Figure 2.19. If the field is applied along the X coordinate, the extraordinary axis aligns parallel to it. The y-polarized band gap experiences a little change, since the Y direction is still occupied by an ordinary axis, but the x-polarized band gap redshifts by about 40 nm, and decreases in width. The decrease in the band gap width indicates smaller refractive index contrast perceived by the x-polarized light, and band gap redshift is due to the average effective index increase. The opposite change happens when the LC extraordinary axis aligns along the Y coordinate (Figure 2.19b). The y-polarized band gap redshifts by about 40 nm, and

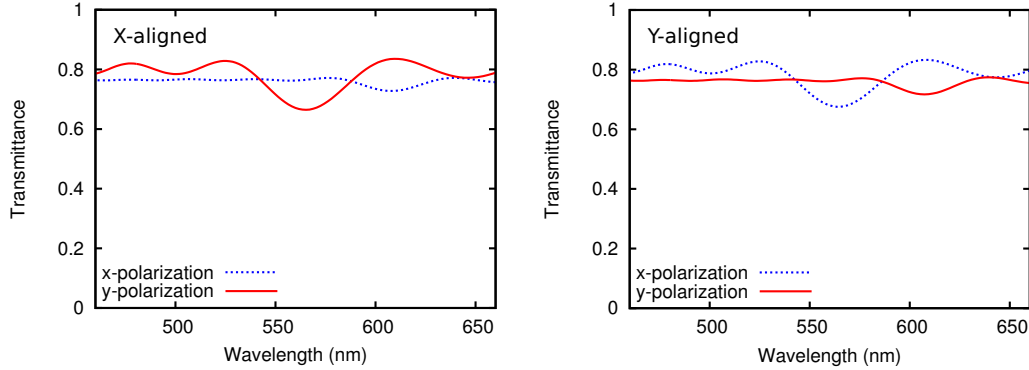


Figure 2.20: FDTD simulated transmission spectra for 29 periods of discrete s-shape columns infiltrated with liquid crystal. On left image the extraordinary index of LC is aligned along the X axis, and in the right image it is aligned along the Y axis. The column geometry is defined by: $P = 288$ nm; $\beta' = 35^\circ$; $\eta = 0.5$; $e = 0.17$; $f = 50\%$; $n = 2.5$.

becomes slightly narrower, while the x-polarized band gap does not significantly change. It is important that while one band gap redshifts with the electric field applied, the other one remains at the original spectral location. The film acts as a polarizing switch, capable of transmitting either x or y-polarized light.

The transmission spectra for these two cases (X- and Y-aligned extraordinary axis) are given on Figure 2.20. The transmission minimum is observed either for x or for y-polarized light at $\lambda \sim 560$ nm. The other polarization has a smaller transmission minimum at $\lambda \sim 610$ nm.

To keep the model simple, the LC optical axis in the absence of field was assumed to follow the column axis regardless of how far the molecule was from the column surface. Equivalently in presence of the electric field the molecules were assumed to be parallel to the field even if located close to the column surface. In practice, intermediate states can be anticipated, where in the absence of external field only molecules nearest to the surface will be parallel to this surface, and the external field will only rotate molecules located sufficiently far away from the surface. In this case spectral separation of the x and y-polarized band gaps in the presence of field can be smaller than shown.

The optical response described here is given for only one particular geometry of s-shaped columns. It will change if the model parameters are adjusted and

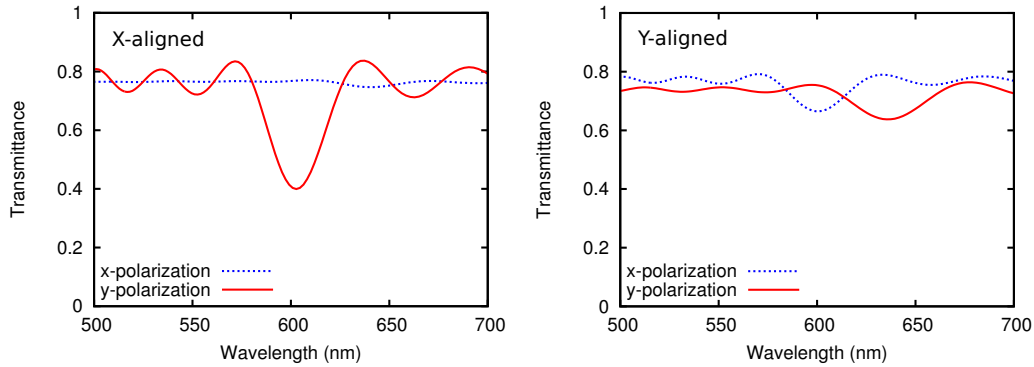


Figure 2.21: The same as on Figure 2.20 but for slightly different column geometry: $P = 288$ nm; $\beta' = 35^\circ$; $\eta = 0.5$; $\mathbf{e} = \mathbf{0.15}$; $\mathbf{f} = \mathbf{50\%}$ and $n = 2.5$.

modified, but the general trend will remain similar: LC molecules oriented along the X axis will redshift the x-polarized band gap by increasing the effective refractive index in this direction. Alignment along the Y axis, accordingly, will redshift the y-polarized band gap, marginally changing the x-polarized one. The band gaps may not stay aligned in the unaddressed state for different combinations of geometric parameters, as for an air-filled film, for example, the band gaps were completely separated. The band gap width also can be modified and potentially enhanced by optimizing the geometry of the film. In Figure 2.21 the transmission spectra are shown for the LC filled film with slightly larger column radius ($f = 0.64$) than in the previous case. The y-polarized band gap in the x-addressed state is considerably deeper here than that seen on Figure 2.20a.

The obvious disadvantage of LC filled columnar films is low refractive index contrast, which requires a large number of vertical periods for substantial filtration. The spectra shown above were calculated for the films with 29 vertical periods, and still the polarization selectivity is small. As we have seen in the previous section similar numbers of vertical periods in air filled films produced well defined transmission minima, and polarization selectivity close to 100%. This makes the LC filled filter better suited for slight modulation of light polarization rather than for filtering purposes.

2.7 Resonant mode narrow band polarizers

Films described above use polarization-dependent band gap properties to filter two orthogonal linear polarizations. The same physical effects can be used to create polarization dependent resonant modes [37]. Resonant modes have very low group velocities of light, and therefore the interaction time of light with the structure is large. For this reason, a noticeable polarization splitting of resonant modes can be expected if even a thin layer of anisotropic defect is inserted into the interference film.

Consider rotationally symmetric vertical post columns with a variable column radius. Columns of this kind are fabricated by GLAD deposition at a continuous fast substrate rotation [129, 113, 41, 37]. Variable column radius is achieved by periodic change in the deposition angle, and if the relation between the effective refractive index and deposition angle is known, one can make a film with a desired refractive index profile. Due to the rotational symmetry these index-graded interference mirrors have a polarization-independent band gap. These band gaps are wider than in s-shaped columns, because film density is varied, rather than its anisotropy.

The defect layer is added as a disturbance in a periodic refractive index profile, either in a form of phase shift, or in a form of additional layer with a constant refractive index. A resonant mode then appears within the band gap, with position depending on the defect layer depth and refractive index.

Since the resonant mode is sensitive to the defect layer refractive index, one can expect two distinct orthogonally polarized resonant modes if the layer is anisotropic. The experimental realization of the interference mirrors with polarization dependent resonant modes has been described in a reference [37]. Figure 2.22 shows the SEM image and the model of a slanted post defect in the rotationally symmetric index-graded film. The simulated transmission for a 16 period index-graded interference mirror with a slanted post defect between 8th and 9th periods is shown on Figure 2.23. Spectra were calculated for a TiO_2 interference filter with sinusoidal refractive index profile defined as $n(z) = 1.96 + 0.43 \cdot \sin(2\pi z/P)$, where $P = 132$ nm. The 100 nm thick slanted post defect layer consists of columns with circular cross-section, tilted by 45° . The band gap width is close to 40% and it depends only slightly on the polarization. The resonant mode is split into two well

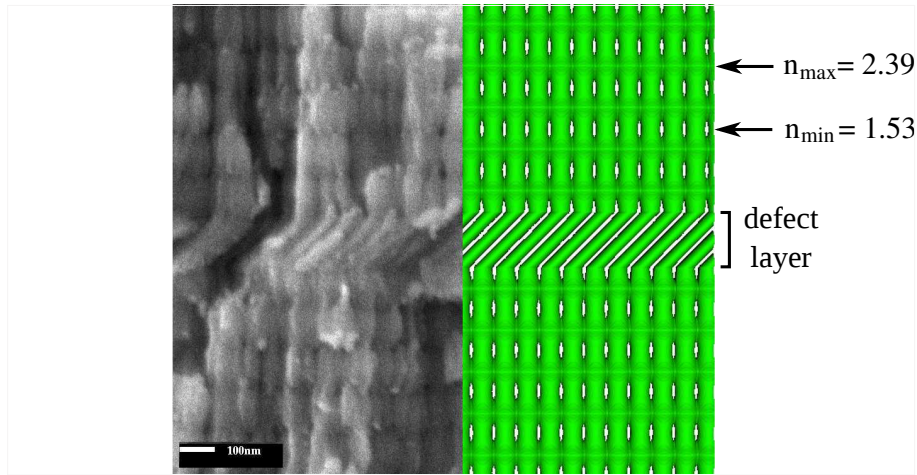


Figure 2.22: SEM image and simulated columns for the index-graded rugate filter with anisotropic defect layer (micrograph courtesy of Matthew Hawkeye).

defined resonant modes. The mode polarized parallel to the defect tilt plane is redshifted relative to the mode polarized perpendicular to this plane.

Similar effects as in the s-shaped columnar polarizers are seen for the defect modes. Figure 2.24 gives FDFD calculated mode positions as a function of column tilt. Two resonant modes overlap if the defect is rotationally symmetric and vertical, and become separated as the defect tilt increases. Both modes increase their spectral width with increasing tilt, indicating the decrease in the quality factor. Resonant mode positions as functions of cross-section broadening are shown on Figure 2.25 for the defect tilted at 45° . As in the s-shaped polarizers, a competitive influence of the column tilt and cross-section anisotropy suppresses the polarization splitting at $e = 0.29$. It is, therefore, beneficial to bring the cross-section of the experimentally realized defect layers close to circular, in order to have a wide resonant mode separation.

2.8 Chapter summary

This chapter presented GLAD fabricated thin film polarizers, employing the concept of periodic anisotropy variation in index-graded interference films. Finite difference electromagnetic modelling methods provided a valuable tool for the in-depth analysis of the relationship between nanoscale architecture and the films'

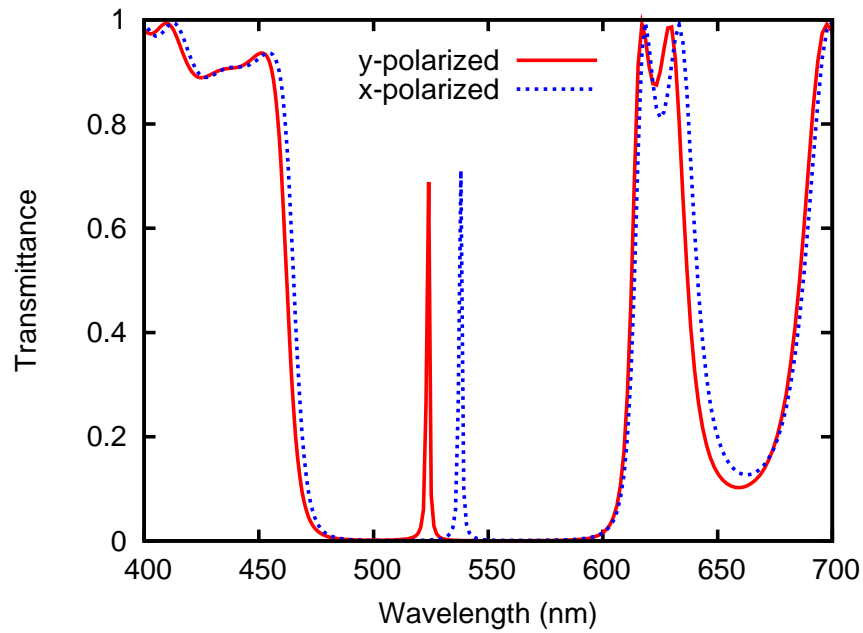


Figure 2.23: FDTD simulated transmission spectra for x- and y-polarized light passing through the index-graded columnar film with anisotropic defect.

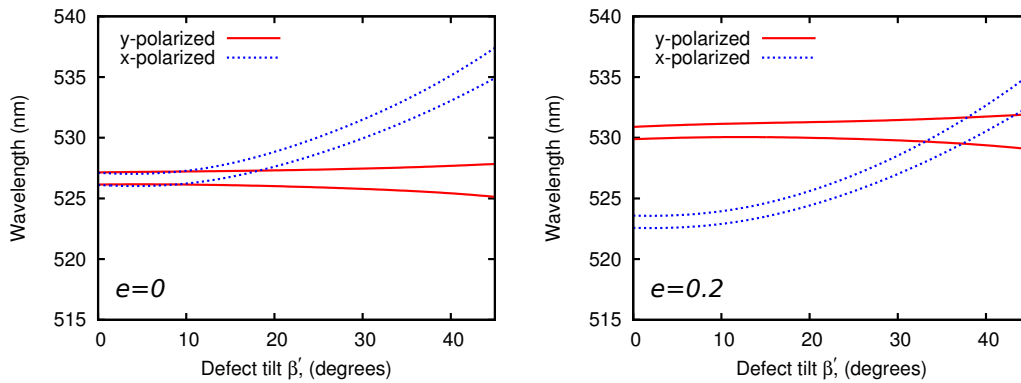


Figure 2.24: Resonant mode spectral location as function of defect tilt β' for the slanted post defect with circular cross-section (left), and y-elongated cross-section with $e = 0.2$ (right).

optical responses. The unobvious connection between cross-section anisotropy and polarizing properties of the thin film were studied and presented. In previous theoretical studies, including those based on numerical simulation techniques, the

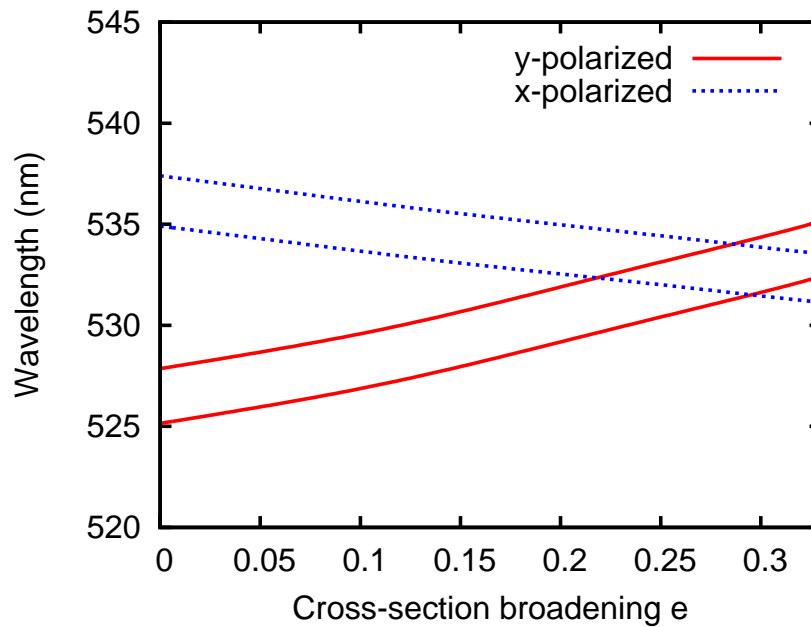


Figure 2.25: Resonant mode spectral location as a function of defect cross-section broadening (defect tilted at $\beta' = 45^\circ$).

GLAD geometries were oversimplified by treating the columns as tilted cylinders rather than variable cross-section posts. Cross-section broadening in GLAD is an additional source of anisotropy, which interacts competitively with the structural anisotropy, programmed by the column shape. The x-polarized band gap suppression is a consequence of this suppression.

Due to the combined influence of periodically varying structural and cross-sectional anisotropies, polarizers have either a single polarizing band or two separate bands. These bands can be further manipulated if the film is filled with a liquid crystal and placed in an external electric field.

Good agreement between theoretical predictions and experimental measurements indicates sufficient model detail, even though the random column distribution was approximated with an ordered array. As mentioned before, this approximation can be safely extended to circularly polarized light since the latter is a linear combination of two phase shifted linearly polarized modes. For the same reason the model is suitable for linearly polarized light incident at any azimuth, other than along the column array lattice vectors.

In the next section, we will continue to analyze the anisotropic GLAD films by considering a model of the columnar interference filter with an omnidirectional reflection band.

Chapter 3

Omnidirectional reflection from vertical post index-graded films ¹

3.1 Motivation

Interference coatings have found niches in many areas of human life. They are used in the laser industry, astronomical instruments, measuring equipment and consumer products. Classical examples are narrow-band interference filters to observe solar atmosphere, and mirrors of laser resonators [15, 141, 142]. Depending on the application, interference mirrors have different arrangements of high and low index layers, determining the spectral response. Distributed Bragg Reflectors (DBR), for example, are made as an alternating sequence of dielectric layers n_1 and n_2 , with constant refractive index throughout each layer. The refractive index profile of these mirrors is described by a pulse function. Rugate index profiles, on the other hand, have a continuous refractive index variation. They produce smaller band gaps than the DBR mirrors, but also have fewer satellite oscillations around the band gap. Continuous index profiles can also be modulated to create a film with an arbitrary spectral response [147].

Transmission and reflection spectra of interference mirrors change with the incidence angle i . As this angle increases, the band gaps typically blueshift and

¹A version of this chapter has been published in Ref. [73].

reduce their width, therefore at a given frequency the mirror usually can be used only in a limited range of incidence angles. Often, however, it is useful if a certain frequency is covered by the band gap at all incidence angles. For example, vertical cavity surface emitting lasers (VCSEL) have flat wide resonant cavities, where radiation can pass through the mirrors at high incidence angles [19, 138]. These lasers will benefit from the resonator mirror's high reflectivity in a broad angular range. Planar waveguides also may have reduced radiative loss if their surfaces are reflective at all incidence angles.

Metal films reflect omnidirectionally in a broad range of wavelengths, but they are inherently lossy. Their reflectivity is high at the long wavelengths of far infrared and microwave, but at the near infrared and optical wavelengths, a large fraction of light is lost to absorption. Photonic crystals present a lossless alternative and reflect light coming from all directions if its frequency falls within their band gaps. For this reason they are used to line waveguides, and small resonant cavities. Some waveguide solutions are ingenious and very practical, such as waveguides stretched from a macroscopic bundles of cylinders to such an extent that pores between cylinders became comparable to the wavelength and form a 2D photonic crystal [66, 105]. In many cases, however, there are no simple ways to line the surface or waveguide with a photonic crystal.

About a decade ago, a group of researchers showed theoretically and experimentally that the omnidirectional reflection is possible from 1D periodic interference mirrors, at least in a narrow spectral range [28]. Even though the band gaps blueshift with the increasing incidence angles, this blueshift can be minimized if the range of propagation directions within the film is small. Light entering the film at an arbitrary angle is refracted into a smaller cone, limited by an angle of total internal reflection. If the band gap covers some frequency within this smaller cone, the light at this frequency will be reflected at all incidence angles. The narrower the cone is, the easier it is to preserve the band gap within it, therefore films with sufficiently high average refractive index may exhibit omnidirectional reflection bands. Band gaps become wider when the refractive index contrast of the mirror is high, therefore high index material together with high refractive index contrast were suggested for omnidirectional reflection [19].

Interference mirrors with omnidirectional reflection bands have been fabricated both in the infrared and in the visible spectral ranges [19, 89, 61, 8, 16]. In the

infrared, silicon is transparent and was often used. It has the one of the highest refractive indices occurring in nature ($n = 3.5$ in the near infrared), therefore readily produces high-index films needed for the omnidirectional reflection.

Omnidirectional band gaps were reported in porous silicon interference mirrors, fabricated by electrochemical etching of silicon wafers with a variable current [4]. The material removal occurs most rapidly on the boundary where bulk crystal is exposed to the electrolyte, because porous silicon has much higher resistivity to current. The boundary moves into the depth of the wafer, leaving behind porous structure, filled with the electrolyte. The higher the current is, the higher the porosity of this structure, allowing one to make variable density films. The porosity cannot be very small, because the electrolyte has to diffuse through the pores and remove material from the film depth. Therefore, highest refractive indices of porous silicon mirrors are relatively small, in the range of 1.22 to 2.43 [81]. Larger average index and index contrasts were achieved with GLAD where the maximum film density was close to the bulk density of silicon [61]. The mirrors were fabricated, and had a maximum index $n = 3.6$ in the near infrared, and an omnidirectional reflection band.

In the visible spectrum, the selection of high index materials is more limited than in infrared. Omnidirectional reflection was achieved on the distributed Bragg reflectors composed of the alternating silica (glass) and tin sulfide, deposited by thermal and by electron beam evaporation [89]. Besides this work, successful realizations of omnidirectional mirrors in the visible are scarce. It is interesting, therefore, to study the potential of GLAD films as omnidirectional mirrors in the visible range. The highest index material available to GLAD and transparent in the visible, is titanium dioxide. Because GLAD produces films in a wide range of porosities and maximum densities close to the bulk material, titanium dioxide could be used to form mirrors with a maximum index close to 2.4. Experimentally it was shown that in titania vertical post films, a refractive index range from $n_{min} = 1.16$ to $n_{max} = 2.23$ is possible [39]. The advantage of GLAD as a single-material fabrication method is obvious, but the optical anisotropy of the columnar structure is also important. Researchers that employed GLAD for silicon omnidirectional mirrors indicated that the film's anisotropy positively affects the omnidirectional bandwidth [61], but did not study the extent of the associated improvement and the limits where it is substantial.

The goal of this chapter is to analyze the role of film's anisotropy in omnidirectional reflection, and to define the limits for refractive indices and film porosities. In the following sections, the model of a rugate columnar filter will be described and simulation results will be discussed and compared to experiment. Similarly to the previous chapter, a focus will be on the films with intercolumnar distances small compared to the light wavelength, and optical response similar to that of a uniform anisotropic index-graded film.

3.2 Interference mirrors and omnidirectional reflection

Interference mirrors are designed as multilayer films, normally composed of transparent dielectrics. They can have various refractive index profiles described by either harmonic or aperiodic functions. Distributed Bragg Reflectors are the simplest of them. Each period is made of two quarter wave plates with identical optical thickness. The ratio between their linear thicknesses is defined as: $n_1 d_1 = n_2 d_2 = \lambda/4$, where λ is the band gap centre wavelength. The profile of the DBR mirror is shown on Figure 3.1 together with sinusoidal and Gaussian profiles considered in this work.

The approximate width of the DBR mirror band gap at normal incidence can be found using a coupled mode theory [145]:

$$\left(\frac{\Delta\omega}{\omega_c}\right)_{DBR} = \frac{|\epsilon_1|}{\epsilon_0} = \frac{4}{\pi} \frac{|n_1 - n_2|}{n_1 + n_2} \quad (3.1)$$

where ω_c is a centre frequency of the band gap, and ϵ_0 and ϵ_1 are the first two Fourier coefficients of the refractive index profile. The band gap of these mirrors is among the widest, but as we will see further it may collapse faster than in rugate films at high incidence angles, and usually is surrounded by strong satellite reflection peaks.

In rugate films, the refractive index varies continuously through the film, without abrupt changes present in the DBR. The classical examples of rugate films are mirrors with a sinusoidal index profile. Their obvious difference from the DBR films is the absence of the high order terms in the Fourier expansion of their index profile. This reduces both satellite oscillations and higher order band gaps, and therefore helps one to avoid the unwanted reflections. The lowest band gap width

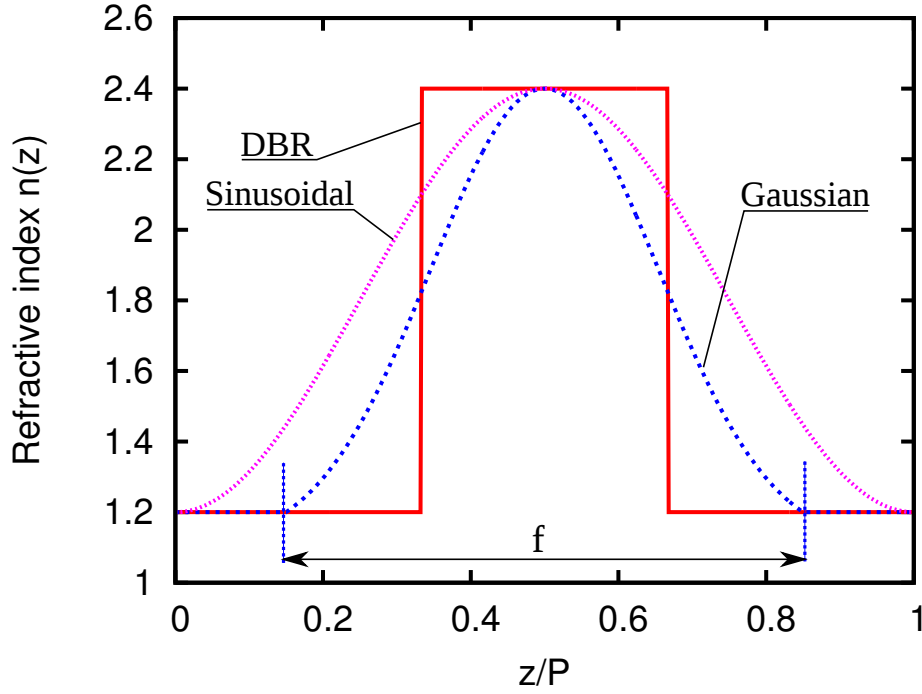


Figure 3.1: Refractive index as a function of position for a single period of sinusoidal, DBR and Gaussian interference mirrors.

is also slightly smaller than in the DBR film:

$$\left(\frac{\Delta\omega}{\omega_c}\right)_{SIN} = \frac{|n_1 - n_2|}{n_1 + n_2} \quad (3.2)$$

Rugate film with profiles other than sinusoidal can avoid high order band gaps entirely, as for example, in an exponential-sinusoidal profile described by the following function:

$$\ln[n(z)] = Q + T \cdot \sin\left(\frac{2\pi z}{P}\right) \quad (3.3)$$

where

$$Q = \frac{\ln(n_{max}) + \ln(n_{min})}{2}$$

$$T = \frac{\ln(n_{max}) - \ln(n_{min})}{2}$$

and P is the index variation pitch.

When looking for the omnidirectional band gaps, the DBR profile may be the most obvious choice, because it has a wide normal incidence band gap, but rugate films may have a lower blueshift with incidence angle, as we will see later.

3.2.1 Omnidirectional band gap

The omnidirectional band gap is defined as a spectral distance between the blue band gap edge at normal incidence and red edge at grazing incidence. Interference mirrors are usually rotationally symmetric in the substrate plane, therefore the band gap is polarization independent at normal incidence. At higher incidence angles, the band gap position and width change differently for s- and p-polarizations. The s-polarized light has an electric vector parallel to the film surface, and p-polarized light has the electric vector in the tilt plane, as shown on Figure 3.2. Both band gaps blueshift with increasing angle, but the p-polarized band width decreases faster than the s-polarized, and the gap disappears at the Brewster angle. Because the p-polarized band gap collapses and shifts faster than the s-polarized, it determines the presence or absence of the omnidirectional reflection band.

The following conditions were defined in prior research as requirements for omnidirectional reflection [20, 21]: (i) large refractive index contrast $|n_2 - n_1|$ helps keep the gap open by making the band gap wide, and (ii) large average refractive index is required to minimize the band blueshift with angle, and to keep the propagation angle in the film smaller than the Brewster angle. The Brewster angle poses a fundamental limit on the lowest refractive index of the film but the conditions are also restricted by a band gap blueshift. We can also show that the omnidirectional band width does not increase continuously increasing refractive index contrast, and disappears when this contrast is large. The simplest example where the restrictions posed by the Brewster angle are seen is a DBR mirror. At the Brewster angle p-polarized light passes from one layer of the film to another without reflection, and no interference occurs. For a DBR mirror composed of the alternating layers n_1 and n_2 and submerged in cladding n_0 this angle can be easily calculated:

$$i_B = \arcsin \left(\frac{n_1 n_2}{n_0 \sqrt{n_1^2 + n_2^2}} \right) \quad (3.4)$$

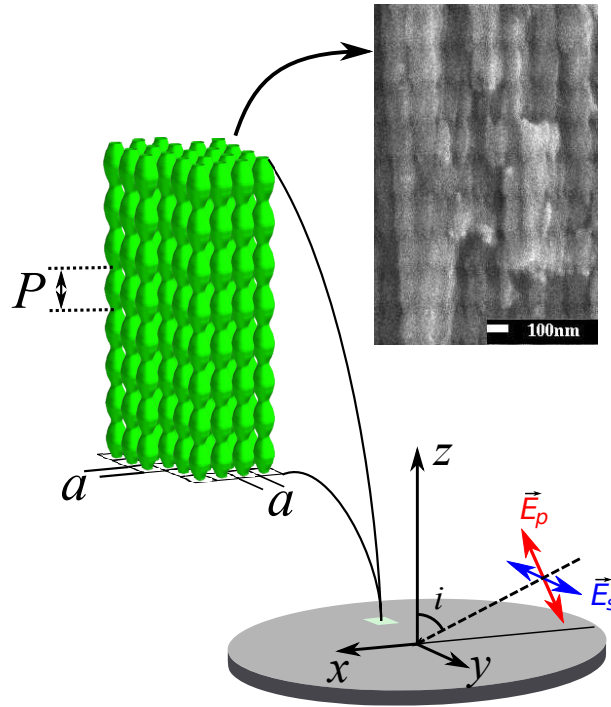


Figure 3.2: The model and SEM image of the index-graded columnar thin film.

Figure 3.3 shows the product $n_0 \sin(i_B)$ as a function of n_1 and n_2 for DBR film. The value $\sin(i_B) = 1$ corresponds to grazing incidence. Modes with $n_0 \sin(i) > 1$ exist in the film but do not have corresponding modes in the incident light. To have an omnidirectional reflection one would like, thus, to have $n_0 \sin(i_B) > 1$. Clearly, if either of the two layers has a refractive index too close to n_0 , omnidirectional reflection will not be observed.

Experimentally, with high refractive index materials, up to 50% wide omnidirectional reflection bands were observed in the infrared on alternating layers of PbTe ($n = 5.27$ at $6.969 \mu\text{m}$ wavelength) and EuTe ($n = 2.29$) [8]. Materials available in the visible range, however, produce omnidirectional reflection bands that are usually less than 10%. Stacks of multiple mirrors are sometimes used to increase the reflection band width. For example, two mirrors that have 10% wide omnidirectional band gaps overlapping by 10% will have a combined reflection band 19% wide. Stacking many mirrors one can get a very large band width,

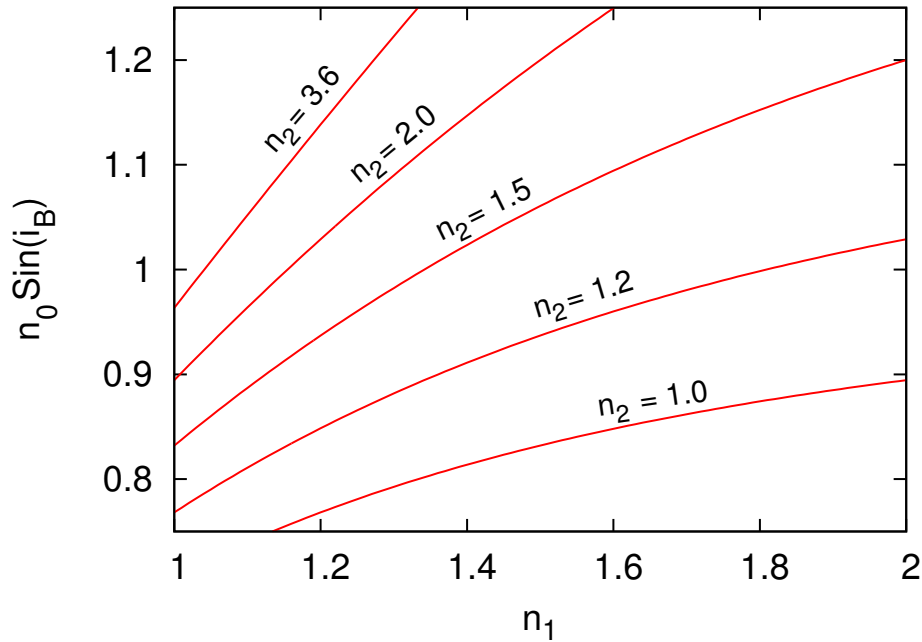


Figure 3.3: Brewster angle in a DBR film as a function of n_1 and n_2 .

covering potentially the whole visible or spectrum and more [148, 89, 57, 84]. The disadvantage of such a stacking approach is a large total film thickness, and high fabrication cost and complexity. Absorption in these thick films can also be an issue. Therefore it is important to maximize the reflection band width in a single mirror, if possible.

Mirrors with a DBR profile generally tend to outperform rugate index profiles in the films composed of isotropic layers, as can be seen from expressions (3.1) and (3.2). Several authors claimed, however, that the Gaussian index profile may produce even wider omnidirectional reflection bands, at least in the range of parameters they used [3, 4, 27, 26]. It is not clear why these authors restricted the total optical thickness of the film to a constant value while optimizing the film in [3]. If they did not, the performance of DBR films would obviously be better than shown. By keeping the optical thickness constant, and increasing the maximum refractive index, they pushed the minimum index of DBR films below the limit defined by equation (3.4), and suppressed the omnidirectional band gap.

Even though performance of the Gaussian films may not be better than that of DBR films, as it was claimed, the Gaussian profile still worth investigating, because

it can produce larger refractive index variance (r.m.s deviation from average) than sinusoidal profile with the same index contrast, but has no discontinuities like the DBR profile. In the Gaussian profile, the refractive index varies continuously following the Gaussian distribution. This function is aperiodic, and has to be truncated at some distance from the peak. When this truncation distance is smaller than the half-pitch of the film, the rest is filled with the low index material close to the refractive index at the truncation point. The derivative of the function is discontinuous, but the function itself is not, therefore fewer defects and scattering can be expected in Gaussian GLAD films than in DBR GLAD.

3.2.2 Modelling and simulation

Angle resolved band gap positions and reflection spectra were simulated using FDTD and FDFD methods. Bloch periodic boundary conditions were used only in the film plane, when simulated in FDTD, and in all directions when simulated in the frequency domain. Because the wavevectors k_x and k_y are not equal to zero at oblique incidence, time-domain simulation is restricted to a single frequency at a time, and multiple simulations must be carried to cover a range of wavelengths. Time-domain simulations are therefore time consuming at oblique angles.

The frequency-domain method is much faster than FDTD at oblique incidence and therefore has been preferred, except for the simulations of transmission spectra at normal incidence. To calculate the band gap positions as a function of the incidence angle, in the frequency domain we need to relate the incident angle and wavevector direction inside the film. At normal incidence the wavevector obviously has the same direction inside and outside the film, and if substrate is in the XY plane, the band structure is calculated as a function of the vector $\vec{k} = (0 \ 0 \ k_z)^T$. If the film is a uniform isotropic slab, the relation between the incidence angle and refracted angle is also easily found using Snell's law, but in columnar films this relation is not obvious. To find it, we can use the fact that the film is composed of the densely packed columns, with the intercolumnar distance much smaller than the light wavelength. Such a film can be treated as a stack of infinitely thin layers of a uniform anisotropic material, with different dielectric constants in each layer. The wavevector component tangential to the surface then remains constant

throughout the film satisfying the boundary condition for electric field:

$$\hat{n} \times (\vec{E}_1 - \vec{E}_2) = 0,$$

where \hat{n} is a unit vector normal to the surface. Because the tangential wavevector component is the same outside and inside the film, any internal propagation wavevector can be related to the incidence angle.

To calculate a band gap position as a function of incidence angle, consider an infinitely periodic film with unit cell dimensions $s_x = a$, $s_y = a$, and $s_z = P$, where $s_x, s_y \ll \lambda$. Let also consider the light incident in the XZ plane, so that $k_y = 0$. Because s_x and s_y are small we can assume that the wavevector component tangential to film's surface remains constant throughout the film: $k_\tau = k_x = \text{const}$. The reciprocal lattice has unit vectors $\hat{g}_z = 2\pi/s_z$, $\hat{g}_x = 2\pi/s_x$, and $\hat{g}_y = 2\pi/s_y$.

A set of dispersion relations along the directions $\hat{k}^{(0)} \dots \hat{k}^{(m)}$ from the point Γ ($\vec{k} = 0$) to the edge of the unit cell (see Figure 3.4) is then calculated. Each dispersion relation shows the band structure along a given direction $\hat{k}^{(l)}$. If band gap exists in this direction, the band gap edges $\omega_1^{(l)}$ and $\omega_2^{(l)}$ are located at the corresponding $k_{x1}^{(l)}$ and $k_{x2}^{(l)}$. The amplitude of the open space wavevector k_0 is easily determined as $k_0 = \omega/c$, where c is speed of light, and the incidence angle is related to k_0 as $k_x = k_0 \sin(i)$. With $k_{x1}^{(l)}$ and $k_{x2}^{(l)}$ known, this gives two incidence angles, corresponding to band edges $\omega_1^{(l)}$ and $\omega_2^{(l)}$:

$$i_{1,2}^{(l)} = \arcsin(k_{x1,2}^{(l)}/\omega_{1,2}^{(l)}). \quad (3.5)$$

For each direction $\hat{k}^{(l)}$ in the film, a pair of frequencies indicating the band gap position and the associated incidence angles are obtained. It is important that these positions are calculated in the assumption of small intercolumnar distances. The method will be invalid for the films where columns stand far apart from each other, such as for square spiral photonic crystals, discussed in the next chapter.

3.2.3 Transfer matrix method

The method described above accurately predicts the band gap position as a function of incidence angle for densely packed columns, as well as for the isotropic and anisotropic uniform index-graded films. Another method used to analyze band

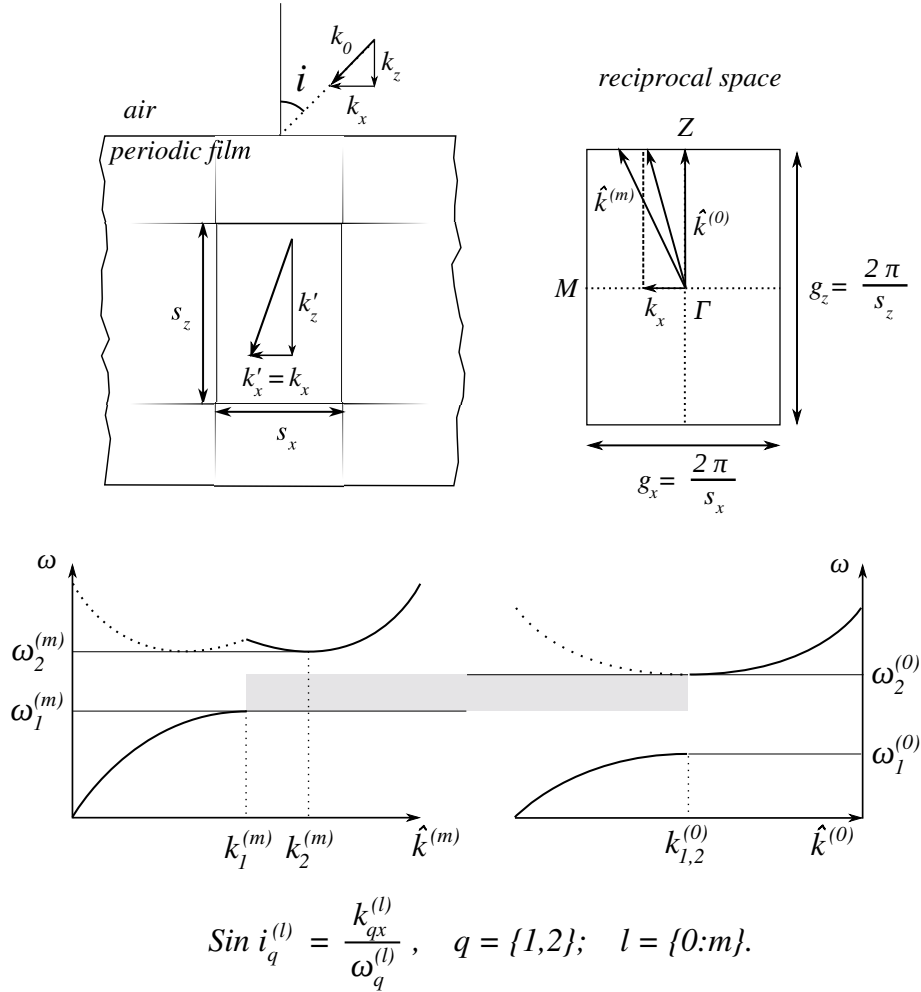


Figure 3.4: FDFD model for the oblique incidence band gap calculations.

gap positions and calculate transmittances/reflectances of the isotropic films is the transfer matrix (TM) method [10]. This method gives the exact solution for multilayer films and has been used to verify the simulated results.

Consider a multilayer film consisting of a series of uniform isotropic slabs separated by planar boundaries $\{1 \cdot \cdot N, N + 1, \cdot \cdot \cdot\}$. The incident plane wave is characterized by the incidence angle i , amplitude E_i and polarization (s or p). On each boundary, the wave is partially reflected, and partially transmitted, and its propagation angle changes according to the Snell's law, as shown on Figure 3.5. For the s-polarized light (transverse electric) the boundary condition for the electric

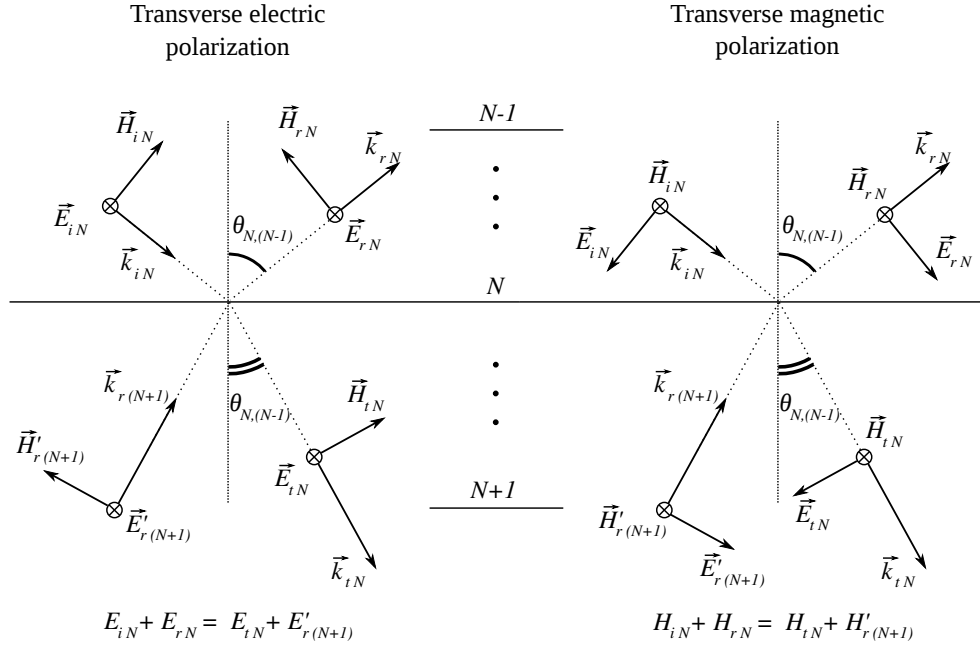


Figure 3.5: Field notations on the periodic boundaries in the transfer matrix method.

field at each boundary N can be written as:

$$E_N = E_{iN} + E_{rN} = E_{tN} + E'_{r(N+1)}, \quad (3.6)$$

where E_{iN} is the amplitude of tangential component of light incident on the boundary from above, E_{rN} is the reflected amplitude, E_{tN} is the transmitted amplitude, and $E'_{r(N+1)}$ is the reflected amplitude from the next boundary, phase-shifted after travelling the distance between these boundaries:

$$E'_{r(N+1)} = E_{r(N+1)} e^{-jkh}$$

and

$$E_{iN} = E_{t(N-1)} e^{-jkh}.$$

If the medium is nonmagnetic, the s-polarized magnetic field tangential components satisfy the following condition:

$$\begin{aligned}
H_N &= \sqrt{\frac{\epsilon_0}{\mu_0}} \cdot (E_{iN} - E_{rN}) \cdot n_{(N-1),N} \cdot \cos(\theta_{(N-1),N}) = \\
&= \sqrt{\frac{\epsilon_0}{\mu_0}} \cdot E_{tN} \cdot n_{N,(N+1)} \cdot \cos(\theta_{N,(N+1)}),
\end{aligned}$$

where $n_{(N-1),N}$ is the refractive index (complex in general) of the slab between boundaries $(N-1)$ and N , and $\theta_{(N-1),N}$ is propagation angle in this slab.

By solving these boundary equations with respect to $E_{(N+1)}$ and $H_{(N+1)}$ we can relate fields on N -th and $(N+1)$ -th boundaries through the matrix equation:

$$\begin{pmatrix} E_N \\ H_N \end{pmatrix} = \begin{pmatrix} \cos(\phi) & \frac{j \sin(\phi)}{Y_N} \\ Y_N j \sin(\phi) & \cos(\phi) \end{pmatrix} \cdot \begin{pmatrix} E_{N+1} \\ H_{N+1} \end{pmatrix} = M_N \cdot \begin{pmatrix} E_{N+1} \\ H_{N+1} \end{pmatrix}, \quad (3.7)$$

where $Y_N = \sqrt{\epsilon_0/\mu_0} \cdot n_{N,(N+1)} \cdot \cos(\theta_{N,(N+1)})$, and $\phi = k_0 \cdot n_{N,(N+1)} \cdot \cos(\theta_{N,(N+1)})$. The matrix M_N is called a characteristic matrix. This matrix is written for s-polarized (TE) light. Using the duality of the electric and magnetic fields, for the p-polarized (transverse magnetic) light characteristic matrix it can be obtained by simply swapping all occurrences of E with H and ϵ with μ in the above equations.

If the film has K layers, the characteristic matrix of this system is defined as a product of the matrices:

$$M = M_1 M_2 \dots M_{K-1}. \quad (3.8)$$

This matrix contains information about transmittance, reflectance, and phase shift of the transmitted light. The transmittance and reflectance are found as $T = t \cdot t^*$ and $R = \frac{Y_s}{Y_0} r \cdot r^*$, where

$$t = \frac{E_{tK}}{E_{i1}} = \frac{2Y_0}{Y_0 m_{11} + Y_0 Y_s m_{12} + m_{21} + Y_s m_{22}} \quad (3.9)$$

and

$$r = \frac{E_{rK}}{E_{i1}} = \frac{Y_0 m_{11} + Y_0 Y_s m_{12} - m_{21} - Y_s m_{22}}{Y_0 m_{11} + Y_0 Y_s m_{12} + m_{21} + Y_s m_{22}} \quad (3.10)$$

$Y_0 = \sqrt{\epsilon_0/\mu_0} \cdot n_0 \cdot \cos(i)$ and $Y_s = \sqrt{\epsilon_0/\mu_0} \cdot n_s \cdot \cos(\theta_s)$ are the admittances of the material that covers the film and of the substrate, respectively. Here n_0 and n_s are the refractive indices of the substrates above and below the film, i is the incidence

angle, and θ_s is the refraction angle for the substrate.

The transfer matrix method provides an analytical solution for isotropic index-graded thin films including those made of dispersive and absorptive materials. Due to the ease of implementation, it will be often employed in this thesis where the isotropic index-graded films are considered. This method can be extended for anisotropic materials, but then it becomes much more complicated. FD simulations accurately describe anisotropic dielectric films, therefore we will limit the transfer matrix calculations to isotropic cases, and use finite-difference modelling to describe anisotropic columnar films.

3.3 Columnar interference filters: the model

GLAD-fabricated columnar interference filters usually have intercolumnar distances smaller than 100 nm; therefore, in numerical simulations the random array can be replaced with a square array of columns. The model of the vertical post structure is shown on a Figure 3.2. The array basis vectors are aligned with X and Y axes, and the incident light is split into two orthogonal polarizations: p-polarized with the electric vector in the XZ plane, and s-polarized with the electric vector parallel to the Y axis. The incidence angle i is measured from the Z axis, in the XZ plane.

The column geometry is characterized by a variable radius R , vertical pitch of radius variation P and the intercolumnar distance a . The intercolumnar distance can be chosen arbitrarily as long as it stays much smaller than the wavelength of light. It has been fixed at $a = 100$ nm in the simulations. To verify the validity of the effective medium assumption, the dispersion relations were calculated for the whole range of column radii from $R \rightarrow 0$ to $R \rightarrow a/\sqrt{2}$ corresponding to the bulk material. The effective refractive index was calculated from the slope of the dispersion curve $\omega(k)$ in the long wavelength regime: $n_{eff} = k/\omega$. FDFD calculations have shown that the dispersion relations are linear at wavelengths larger than approximately $2.5a$ for all possible column diameters, and the effective refractive index in the long wavelength limit does not depend on a . The principal refractive indices and film density (f) were calculated for each columnar array and approximated with the Maxwell-Garnett approximation [86] complemented with the correction terms as follows:

$$f(n) = f_{MG}(n) + f_0 + \sum_{m=1}^7 f_m \sin(m\pi(n-1)/n_{TiO_2} - 1) \quad (3.11)$$

$$f_{MG}(n) = \frac{(2n_0^2 + n_{TiO_2}^2)(n^2 - n_0^2)}{(n_{TiO_2}^2 - n_0^2)(n^2 + 2n_{TiO_2}^2)}$$

where f_m are the coefficients of the expansion, listed in the Table 3.1, and $n_0 = 1$ is refractive index of air.

m	f_m
0	$3.25 \cdot 10^{-3}$
1	0
2	$3.56 \cdot 10^{-2}$
3	$-8.97 \cdot 10^{-3}$
4	$3.16 \cdot 10^{-3}$
5	$2.69 \cdot 10^{-3}$
6	$-7.34 \cdot 10^{-4}$
7	$-1.20 \cdot 10^{-3}$

Table 3.1: Coefficients for the series expressing TiO_2 film density as a function of the effective refractive index.

Figure 3.6 shows FDFD calculated principal refractive indices for the TiO_2 columns arranged in a square lattice as a function of film relative density f . The extraordinary refractive index n_e is higher than the ordinary n_o , and the anisotropy ($n_e - n_o$) peaks at $f \approx 47\%$. At very small and large densities the refractive index becomes close to that of air and of the TiO_2 respectively, and the anisotropy decreases. The Maxwell-Garnett approximation is plotted together with the FDFD calculated indices, and appears very close to the ordinary refractive index. Good agreement between the approximation and simulated ordinary refractive index is expected, because the Maxwell-Garnett approximation describes an array of spheres or cylinders, and the GLAD film is composed of such an array.

At normal incidence, only the ordinary refractive index affects the light passing through the film; therefore, both in the experiment and in simulations the ordinary refractive index was used to design an index profile. The extraordinary index is not proportional to the ordinary one as a function of film density, and therefore does not merely represent a scaled copy the ordinary index profile. Three index profiles were considered, shown on Figure 3.1. The DBR profile consists of an alternating

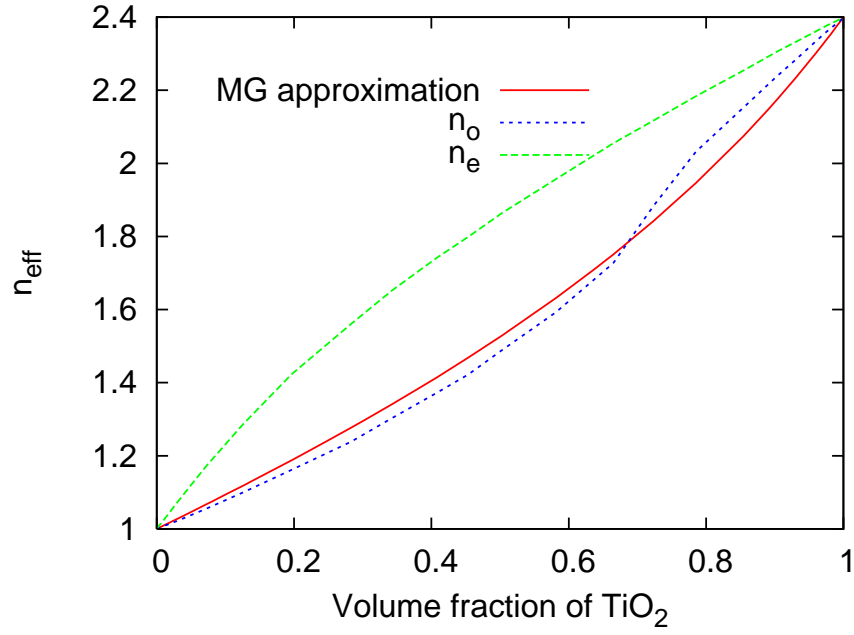


Figure 3.6: FDFD calculated ordinary and extraordinary refractive index for the vertical post film as a function of the relative film density.

sequence of high and low index layers with a fraction of high index material

$$\delta = P \frac{n_{min}}{n_{max} + n_{min}}. \quad (3.12)$$

The sinusoidal profile was the one fabricated in the experiments, defined as:

$$n_{sin}(z) = \frac{n_{min} + n_{max}}{2} + \frac{n_{min} - n_{max}}{2} \sin\left(\frac{2\pi z}{P}\right), \quad (3.13)$$

In the Gaussian profile, following the approach of previous authors [4, 26, 27], each period of the film was divided into two sections A and B, one described by a Gaussian function, and the other one occupied by a constant index material. The index profile in a section A is defined as

$$n_A(z) = n_0 + \Delta n \cdot e^{-\frac{(z-P/2)^2}{(4qP\sigma)^2}}, \quad (3.14)$$

where q is a fraction of pitch P occupied by the Gaussian function. In section B, the refractive index is constant $n_B(z) = n_0 + \Delta n \cdot \exp[-1/(16\sigma)^2]$, equal to the

index in the Gaussian profile on the edge of section A [4]. This is slightly different from the definition in the prior research, where this index was up to 5% lower than on the edge of the section A, giving slightly higher index contrast, but introducing a small discontinuity into the profile.

In the frequency domain, a single period of the film was considered and a simulation cell size was $(d_x, d_y, d_z) = (a, a, P)$. In the time domain, the same cell was repeated 16 times along the Z axis. The glass substrate was taken into account in the time-domain simulations, but shown very little difference compared to a free standing film. A grid size with resolution $\Delta = 5$ nm yielded accurate results, and even lower resolution could be used.

3.4 Omnidirectional band gap in isotropic and in columnar films

The band gap properties of the isotropic index-graded films can be easily calculated with the transfer matrix formalism. Therefore, first we consider the isotropic index-graded films to see the limits, where the omnidirectional reflection is observed. Figure 3.7 shows s- and p-polarized band gap edges as a function of incidence angle for the DBR profile with the maximum index $n_{max} = 2.4$, minimum index $n_{min} = 1.5$, and pitch $P = 200$ nm. Band gaps of both polarizations coincide at normal incidence and blueshift with the increasing incidence angle. Approaching the Brewster angle, the p-polarized band gap shrinks faster than s-polarized, but remains within its boundaries. The 3.8% wide omnidirectional reflection band exists between 643 nm and 668 nm where the band gap covers both polarizations at all incidence angles. The data for the isotropic films were obtained using both transfer matrix formalism and FDFD, and both methods gave nearly identical results, with the observed difference in the positions of band gap edges less than 0.7%.

Figure 3.8 shows the omnidirectional reflection band width for the isotropic DBR, sinusoidal and Gaussian films as a function of the minimum refractive index n_{min} . The maximum refractive index of the films is $n_{max} = 2.4$ and Gaussian profile is optimized for the maximum band width ($\sigma = 0.22$ and $q = 1$). In all refractive index profiles, the omnidirectional reflection band width increases with

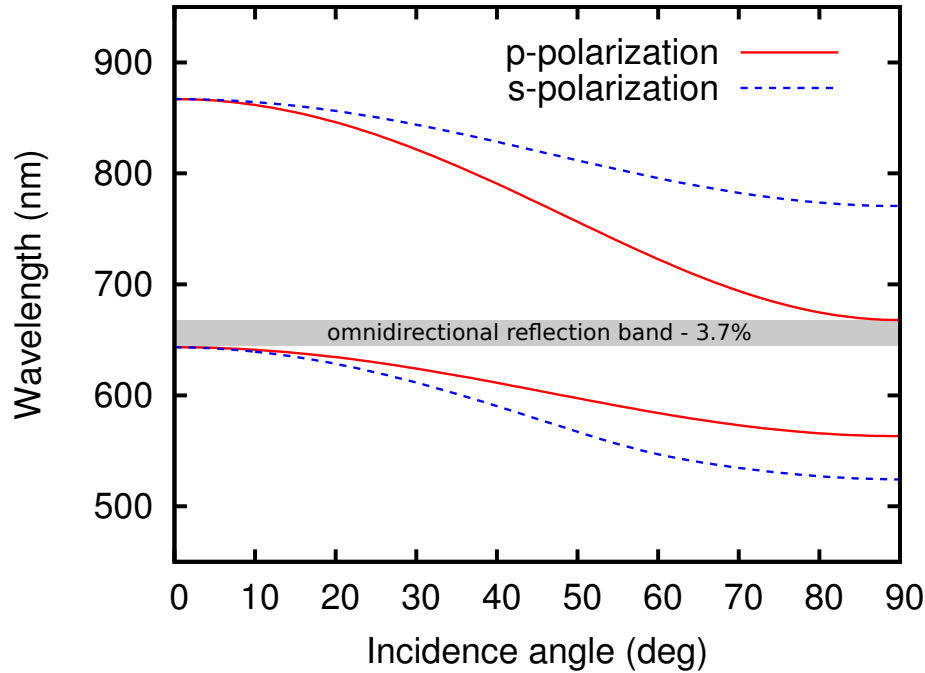


Figure 3.7: FDFD/TM calculated band gap positions for s- and p-polarized light in isotropic DBR film as a function of incidence angle ($n_{min} = 1.5$, $n_{max} = 2.4$).

the refractive index contrast ($n_{max} - n_{min}$) to a certain point and then decreases. The index contrasts higher than optimal suppress the omnidirectional reflection at $n_{min} < 1.28$ for the DBR profile, and $n_{min} < 1.17$ for the sinusoidal profile. This result has not yet been pointed out in the literature, where high index contrasts were usually pursued but low index values close to that of air were not considered. We can see, however, that even the isotropic index profiles lose their omnidirectional reflective properties when the index contrast is high. This band gap collapse is caused by the decrease in the Brewster angle at low values of n_{min} .

Gaussian and sinusoidal profiles have almost the same omnidirectional band width, peaking at about 2%. The DBR profile outperforms them, but still the omnidirectional band width does not exceed 4%. The DBR profile band width peaks at larger n_{min} than Gaussian or sinusoidal, and with increasing index contrast (decreasing n_{min}) collapses much faster. In rugate films, the Brewster angle is larger than in the DBR with the same index contrast. Therefore, their band gaps shrink less with the incidence angle. Despite a smaller normal incidence band

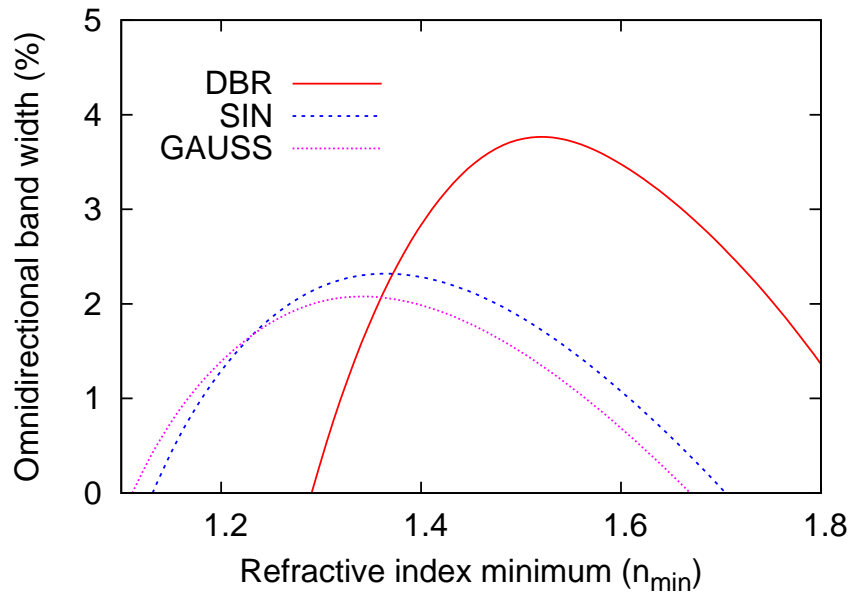


Figure 3.8: FDFD/TM calculated omnidirectional band width as a function of n_{min} for the isotropic films with $n_{max} = 2.4$.

gap at normal incidence, the omnidirectional reflection is achieved.

For the larger maximum refractive index values, the omnidirectional band width increases, while qualitative relationships remain unchanged. Figure 3.9 shows the reflection band width as a function of n_{min} for $n_{max} = 2.5$. The peak band width increased to 6.5% for DBR profile, and almost to 5% for the Gaussian and sinusoidal profiles. The Gaussian profile still peaks slightly lower than the sinusoidal one, and both are outperformed by a DBR profile.

In the anisotropic thin films, as Figure 3.10 shows, the omnidirectional band gap is substantially wider. The figure shows the reflection band width for the variable radius titanium dioxide columns ($n_{TiO_2} = 2.4$). The film's ordinary refractive index varies from n_{min} to $n_{max} = 2.4$ following DBR, sinusoidal and Gaussian index profiles. Even though these profiles are the same as those used for the isotropic films, the DBR mirror now has the omnidirectional band width 14.5%, while sinusoidal and Gaussian profiles peak at nearly the same, 10.5%. The band width increased by a factor of three to four compared to the isotropic films. Gaussian and sinusoidal profiles still have an almost identical optical response, and the

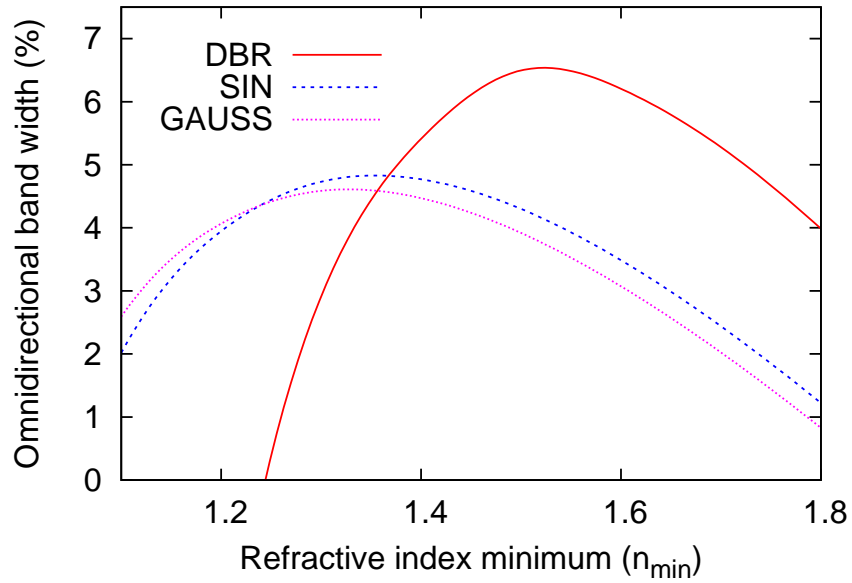


Figure 3.9: FDFD calculated omnidirectional band width as a function of n_{min} for the isotropic films with $n_{max} = 2.5$.

DBR profile still peaks at higher n_{min} than the rugate profiles. Compared to the isotropic analogs the band width is maximized at lower n_{min} ($n_{min} \approx 1.22$ with sinusoidal/Gaussian profiles and $n_{min} = 1.3$ with the DBR profile). In the isotropic films these values were $n_{min} = 1.35$ and $n_{min} \approx 1.5$ correspondingly.

The better performance of the anisotropic thin films is achieved due to the high extraordinary index affecting p-polarized light at oblique incidence. At oblique incidence, the effective index for p-polarized light increases and the band gap blueshift slows down. The s-polarized band gap, however, remains the same as in the isotropic film because the s-polarized effective film's index does not change with the incidence angle.

3.5 Experimental realization of the columnar mirror

Theoretical work presented here has been done in collaboration with Matthew Hawkey, who fabricated and characterized the films. The film which is described below had sixteen periods and its SEM image is included on the Figure 3.2. The

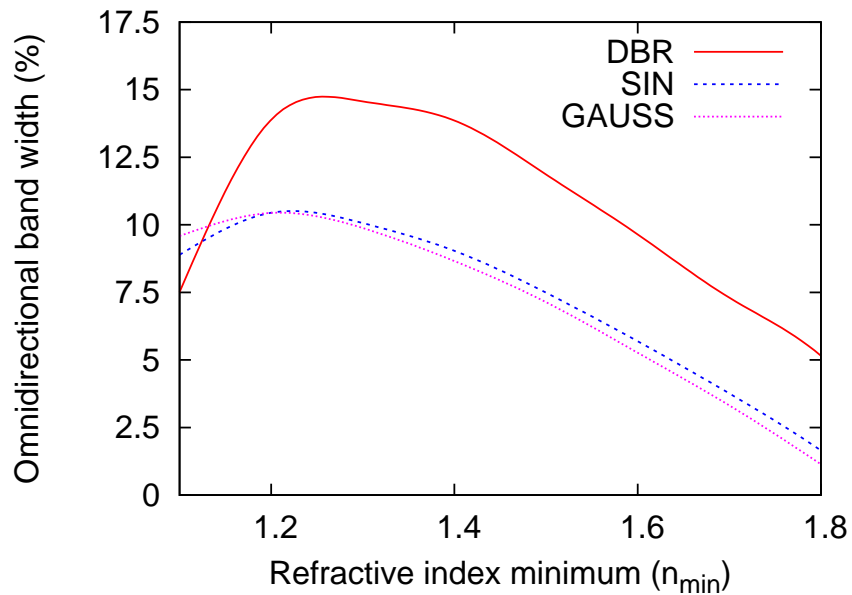


Figure 3.10: FDTD calculated omnidirectional band width as a function of n_{\min} for the GLAD columnar films with $n_{\max} = 2.4$.

film was fabricated at a continuous substrate rotation and variable deposition angle to imprint sinusoidally variable refractive index. To relate the effective refractive index to the deposition angle, a series of vertical post films were prepared at deposition angles ranging from 40° to 86° , and their ordinary refractive index was measured using a variable angle spectroscopic ellipsometer (V-VASE) [39]. This relation was then used to create a sinusoidal refractive index profile. Films were deposited at a background pressure of $8 \cdot 10^{-5}$ Torr and then annealed for 12 h at 70° C in air to ensure a stoichiometric film composition. The angle resolved transmittance of s- and p-polarized light was measured from 400 to 900 nm at incidence angles between 0° to 70° in 5° intervals. The collimated output from a fibre-coupled tungsten-halogen lamp (Ocean Optics LS-1) was passed through a ~ 1 mm wide aperture, polarized and after passing through the sample, collected by a fibre coupled spectrometer (Ocean Optics USB2000). The measured spectral intensity was normalized to the intensity with the sample removed.

Figure 3.11 shows the FDTD simulated and measured normal incidence transmittance spectra for sixteen periods of the columnar rugate filter with the ordinary

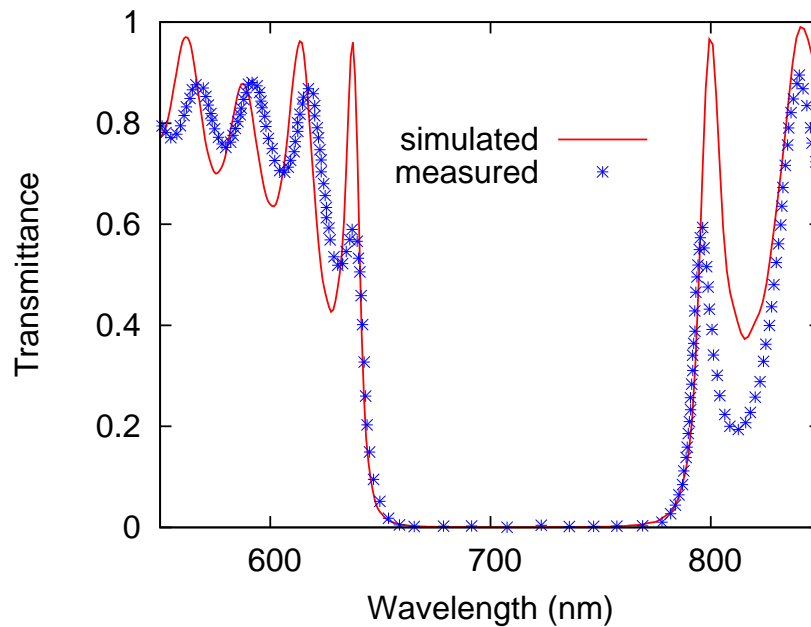


Figure 3.11: Experimentally measured and FDTD simulated normal transmission through sixteen periods of the columnar film with sinusoidal index profile on quartz substrate (from SEM data: $n_{min} = 1.54$ and $n_{max} = 2.32$).

refractive index varying between $n_{min} = 1.52$ to $n_{max} = 2.32$. The pitch of index variation was determined from the SEM image: $P = 178$ nm. Transfer-matrix calculated spectra for 16 periods of this index profile show $\sim 2.7\%$ transmission on the band gap edges at normal incidence. Using this value we can locate band gap edges in the measured spectrum at 648 nm and 778 nm respectively. Simulated data are in good agreement with the experiment both in terms of the band gap width and position, and the Fabry-Perot oscillations surrounding the gap. At short wavelengths the simulated Fabry-Perot oscillations stand slightly wider apart than measured, because the simulated film material was assumed to be nondispersive and nonabsorptive, while in practice the titania refractive index increases at short wavelengths, and makes film's optical thickness slightly larger.

In Figure 3.12, FDFD calculated and experimentally measured band gap positions are given as a function of the incidence angle. The experimental data were measured only up to a 70° incidence angle, but simulated band gaps cover the whole range of angles and show the omnidirectional reflection band from 648 nm

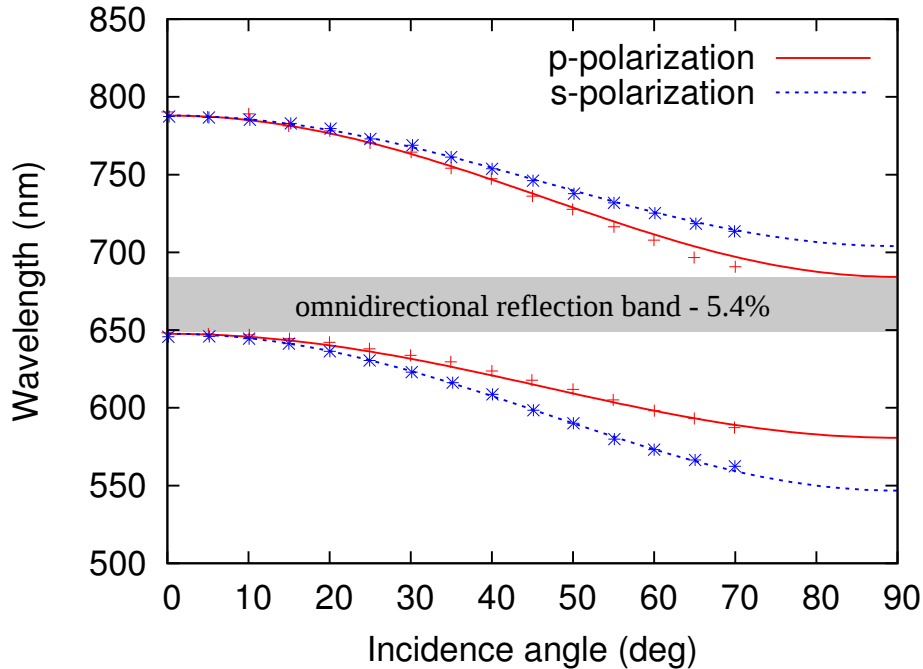


Figure 3.12: Experimentally measured (dots) and FDFD calculated (lines) band gap positions as a function of incidence angle for the same film as on Figure 3.11.

to 684 nm. The relative width of this band is 5.4% of the centre wavelength. The omnidirectional reflection band does not appear in the analogous isotropic film, as shown in Figure 3.13. This figure shows p-polarized band gaps for the sinusoidal film with $n_{min} = 1.52$ and $n_{max} = 2.32$, one for the columnar film and the second for the isotropic one. In the columnar film, the p-polarized band gap remains relatively wide at large incidence angles, and also blueshifts slightly slower.

Good agreement between theory and experiment indicates the validity of theoretical assumptions and gives some confidence in the simulated results at angles exceeding the measured range. Also the good agreement between theory and experiment provides grounds for a theoretical optimization of thin film architecture, which will be discussed next.

3.6 Band gap optimization

We have seen already that the omnidirectional reflection band is maximized at a certain value of n_{min} , depending on n_{max} and on the choice of function describing

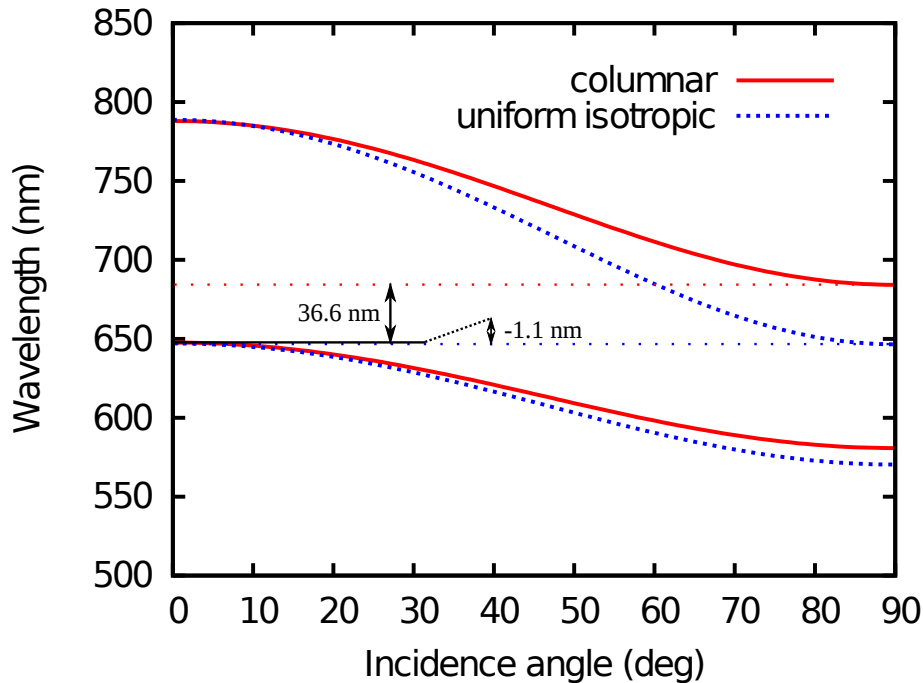


Figure 3.13: P-polarized band gap positions as a function of incidence angle compared between the isotropic and columnar films with the identical sinusoidal index profile ($n_{min} = 1.54$, $n_{max} = 2.32$)

the index profile. With this in mind, achieving the highest omnidirectional band width is not just a question of maximizing the refractive index and index contrast, but a question of finding their optimal combination. The choice of the index profile also matters. The DBR profile outperforms rugate profiles both in uniform and in anisotropic films, but in GLAD deposition, abrupt changes in the deposition angle may induce column growth defects, which will increase the diffuse scattering. The sinusoidal profile has no discontinuities but also has a relatively small band width, and the same can be said about the Gaussian profile.

A number of parameters that can be optimized to improve the filter varies for different profiles. However, all of them are characterized by a vertical pitch P , and maximum and minimum indices. Among these parameters, pitch does not influence the relative band width. Maximum index is defined by the choice of deposited material and in the visible range titanium dioxide gives one of the highest values.

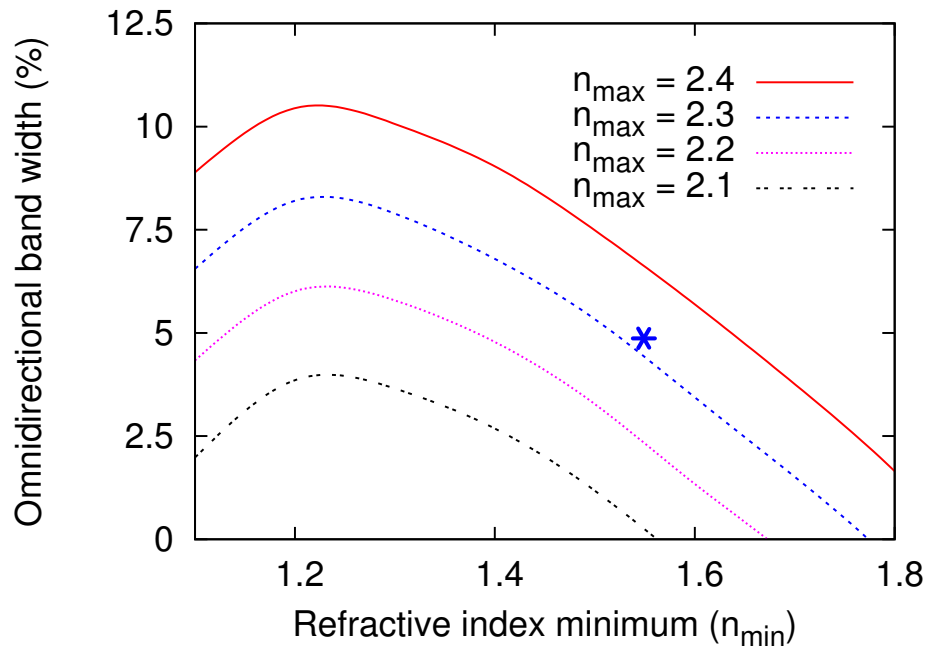


Figure 3.14: FDFD calculated omnidirectional band width as a function of n_{min} and n_{max} for the columnar films with sinusoidal index profile. Star indicates the position of experimentally fabricated film.

Figure 3.14 shows the omnidirectional band width as a function of n_{min} and n_{max} for the columnar film with the sinusoidal index profile. The width increases linearly with the maximum index n_{max} and peaks at $n_{min} \approx 1.22$ regardless of the n_{max} value. The experimentally fabricated film is shown with a star on this diagram, shifted rightwards with respect to the optimal index contrast. The highest refractive index in the fabricated GLAD film is close to the one of bulk TiO_2 , but the minimum refractive index is still high. If n_{min} is optimized, the band width can increase by least 50% of the present experimental value.

The Gaussian profile provides more freedom for optimization, since one can vary the pulse width together with the minimum and maximum index values. The Gaussian rugate film described by Figure 3.10 was optimized for the maximum band width in the isotropic index-graded films. The values of q and σ in that configuration were $q = 1$ and $\sigma = 0.22$ and they become different in the optimized columnar film. Because q and σ stand in the equation as a product, each of them affect the pulse width in the same way, with the only difference that reducing

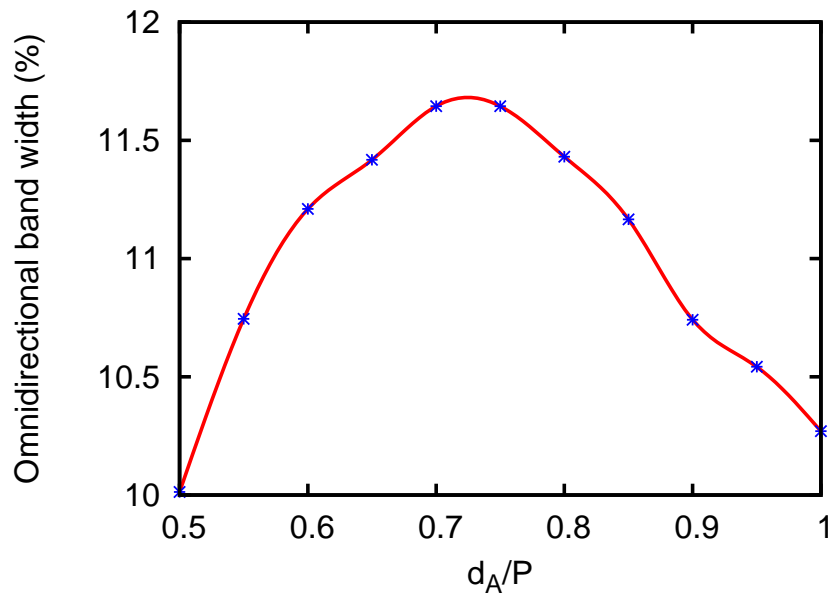


Figure 3.15: FDFD calculated omnidirectional band width as a function of the parameter q for the Gaussian index-graded columnar film ($n_{min} = 1.25$, $n_{max} = 2.4$, $\sigma = 0.22$, points are interpolated with cubic splines). See Section 3.3 for the description of the Gaussian profile model.

q moves the truncation points closer to the pulse centre. Figure 3.15 shows the omnidirectional band width as a function of pulse width q , while the variance is fixed at $\sigma = 0.22$. The band width improves with q decreased and peaks at $q = 0.72$, smaller than optimal in the isotropic film. This is caused by the nonlinear dependence of film anisotropy on density. At very low and high refractive indices, the anisotropy is small, as the index approaches that of the bulk material or of the air. A decreased pulse width, however, improves the reflection band by increasing the film's anisotropy. The reflection band width as a function of σ is also described by a bell curve as shown on a Figure 3.16. From this graph we can see that the optimal parameters of the Gaussian TiO_2 columnar mirror are $q = 1$, and $\sigma = 0.15$ if $n_{min} = 1.25$ and $n_{max} = 2.4$. This structure gives a relative band width of 12.1%, which falls almost in the middle between the sinusoidal rugate films (10.5%) and DBR films (14.5%).

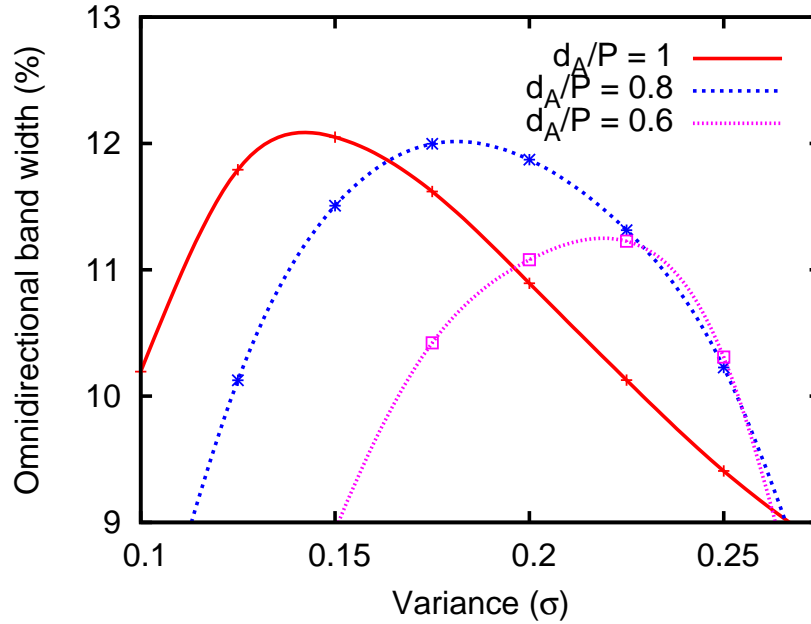


Figure 3.16: Omnidirectional band width as a function of σ the Gaussian index-graded columnar films ($n_{min} = 1.25$, $n_{max} = 2.4$, points are interpolated with cubic splines).

	Isotropic uniform	Anisotropic columns
DBR	3.8% ($n_{min} = 1.52$)	14.5% ($n_{min} = 1.28$)
Sinusoidal	2.3% ($n_{min} = 1.36$)	10.5% ($n_{min} = 1.22$)
Gaussian	2.0% ($n_{min} = 1.34$)	12.1% ($n_{min} = 1.20$)

Table 3.2: Maximum reflection band widths for isotropic and anisotropic index-graded mirrors with $n_{max} = 2.4$.

3.7 Chapter summary

The anisotropy of columnar films substantially enhances omnidirectional reflection from 1D periodic index-graded films. In titanium dioxide columnar films, the reflection band width is more than three times larger than in the isotropic analogs for the DBR index profile, and up to four times larger for the sinusoidal and Gaussian profiles. In this light, GLAD provides a unique opportunity to create anisotropic index-graded films with arbitrary index variation, significantly improving the angular dependence of the reflection spectra. Currently the fabricated index-graded mirror with a sinusoidal profile has a 5.4% wide omnidirectional band gap as the

refractive index contrast is only $\Delta n = 0.8$. The optimal index contrast $\Delta n = 1.15$ would show reflection bands up to 10.5% wide. With the DBR profile the band width is further improved up to 14.5%. Potentially it can be even larger if multiple materials are used in the deposition. For example, titanium dioxide can be used to deposit a high index layer with relatively low anisotropy but high index, and columnar silica deposited as an anisotropic low-index layer.

The findings of this chapter are rather general and not limited to the GLAD technique. Any anisotropic material with high values of the extraordinary index used in the interference film will stabilize the band gap spectral position and potentially improve the omnidirectional band gap. The GLAD method, however, provides the most straightforward fabrication base for anisotropic thin films. The spectral range of these films is limited by the intercolumnar distance, which has to be small compared to the wavelength of interest. In GLAD-deposited titanium dioxide films, these distances usually fall below 100 nm, making films usable from near ultraviolet to any longer wavelength where the material is transparent.

At shorter wavelengths, the interference of light scattered from individual columns comes into play, and approximations made for rugate mirrors and for s-shaped polarizers are no longer valid. Randomly distributed columns at short wavelengths produce excessive scattering, but if columns are ordered on the substrate, new properties arise because of this periodicity. The following chapter will address films with widely spaced periodically arranged columns, which serve as photonic crystals. Specifically, the chapter will be about square spirals, which have been known for a decade as one of the effective photonic crystal architectures.

Chapter 4

Square spiral photonic crystals with a visible band gap ¹

4.1 Motivation

The square-spiral photonic crystal was first proposed and simulated by Toader et al. in 2001 [122, 123]. This structure utilizes crystallographic symmetry of a diamond lattice, which is known to produce wide 3D photonic band gaps, with the widest band gaps observed in the network of cylindrical bonds, connecting the adjacent nodes of the diamond lattice [43, 44]. The square spiral arms connect nodes in the diamond lattice, which do not necessarily have to be the nearest neighbours. If the spiral arms connect n-th nearest lattice nodes, such an architecture is classified as a diamond:n square spiral. The original and subsequent works by Toader considered diamond:1, diamond:3 and diamond:5 square spirals, concluding that diamond:5 architecture produces the widest 3D photonic band gap among those three types.

Diamond:1 square spiral is the easiest to fabricate by GLAD, since the structure's column tilts fall into the range attainable with the GLAD technique. The GLAD fabrication method has certain advantages over other techniques of square spiral fabrication: fabrication speed, long range order of columns, and the ability to cover large areas in a single deposition step. Among the other methods, direct laser writing also produces high quality square spiral crystals. This method covers

¹A version of this chapter has been published in Ref. [68].

an almost unrestricted range of column tilts and allows one to include point and line defects into the crystal, but remains time consuming and therefore not suitable for mass-production [106].

In theoretical works by Toader, it has been shown that any transparent material with refractive index larger than $n = 2.2$ is suitable for fabrication of square spiral photonic crystal with full 3D band gap. The larger the refractive index is, the wider this band gap will be. For this reason in early fabrication works silicon was used as column material, since it has high refractive index $n = 3.6$ at telecommunications wavelengths [62, 63, 56]. Fabrication of square spiral photonic crystals becomes more challenging in the visible spectral range, where the lattice constant of the crystal is around the one third of that in the telecommunications range. Design tolerances also become more stringent as the selection of transparent materials is limited to dielectrics with relatively low refractive indices. One of the best suitable materials in this range is titanium dioxide (TiO_2).

This chapter investigates the influence of a number of geometrical parameters of GLAD fabricated square spirals on 3D band gap formation, with a goal of optimizing the crystal architecture but staying close to the limits of GLAD fabrication technique. Issues which have not been addressed in previous theoretical works, such as effects of column cross-section geometry and potential of column density variation, will be discussed. The work was done as a collaboration between the author of this manuscript on a theoretical side and researchers in the GLAD laboratory at the University of Alberta. Substrates were prepared and square spiral film was deposited by Joshua Krabbe, and then optically characterized by Dr. Michael Taschuk. The author, on his side, theoretically investigated the experimental results, and developed the recommendations on the square spiral optimization in a framework of the current deposition capabilities.

4.2 Fabrication procedure

In square spiral photonic crystals, the columns are arranged on a substrate in a square array. This requires substrate patterning, to create the initial array of protrusions, from which columns grow. Several seeding methods can be mentioned, such as electron beam lithography, self assembly of nano-spheres, photolithography, or nanoimprint lithography [64, 63, 151, 23, 36]. Electron beam lithography

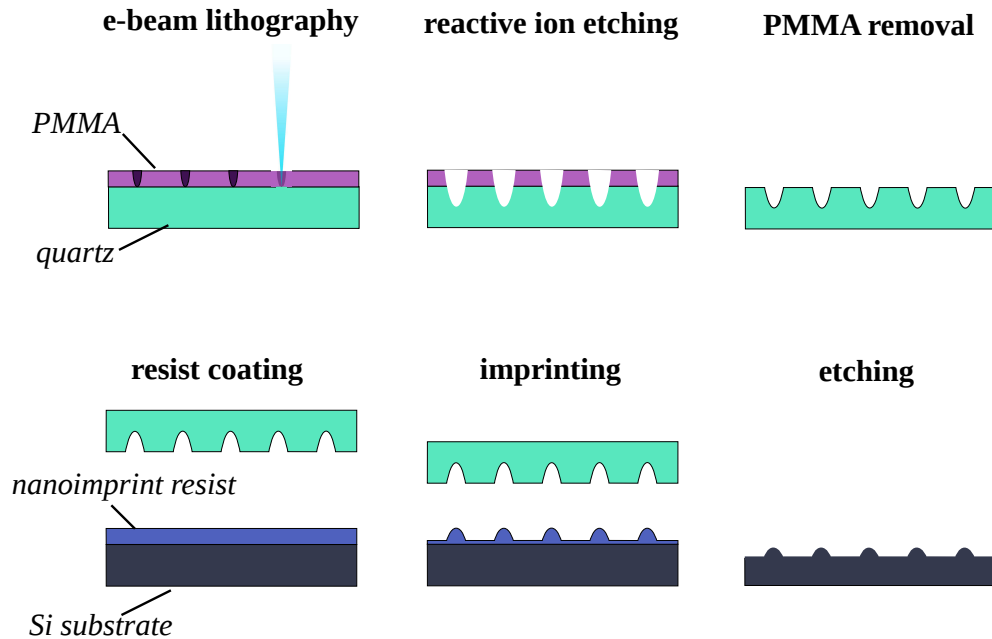


Figure 4.1: The process flow for nanoimprint lithography

provides good quality arrays, but prohibitive in fabrication speed and not suitable for mass production. Self-assembly techniques, on the other hand, can cover large substrate areas, but lack long-range seed order, and usually produce hexagonal seed arrays, while square spiral photonic crystal requires a square array. Laser direct write method produces good results, but like the e-beam lithography, it is limited to small scales and costly.

In this work, nanoimprint lithography was used. It is among the best candidates for square seed arrays, since it is able to cover large substrate areas with good long range order, and it can produce the lattice of seeds with spacings on the order of hundreds of nanometers, needed for the band gap in the visible range. This choice has been motivated not only by the large substrate areas covered by nanoimprint, but also by the economical advantage over photolithography, since nanoimprint method does not use costly projection equipment.

Figure 4.1 shows the process flow for the nanoimprint stamp fabrication and subsequent imprinting process. Nanoimprint stamps were fabricated on quartz plates using a Raith 150 electron-beam lithography system. One-eighth inch thick (3.18 mm) quartz plates were diced into 20 mm squares, cleaned, and coated with

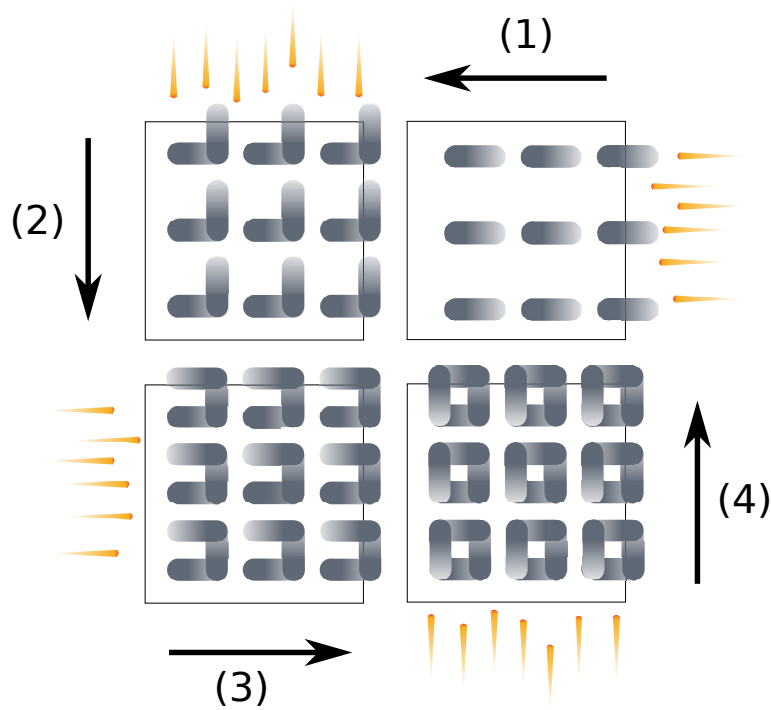


Figure 4.2: Deposition of a single square spiral period.

polymethyl-metacrylate (PMMA). A square array of dots was then patterned on the resist using the Raith 150. One 5 mm wide circular area was patterned with lattice spacing 320 nm and a number of 1 mm wide square stamps were produced with the lattice spacings from 80 to 400 nm. This range of lattice constants potentially can be used to deposit square spiral crystals with band gap centered anywhere between ~ 150 nm and ~ 750 nm.

The pattern of dots was transferred onto the quartz plate through 25 second etch process using a Surface Technology Systems reactive ion etch system. After cleaning and drying, the nanoimprint stamps were treated with perchlorsilane vapour, to make them highly hydrophobic and limit resist adhesion during the imprint process.

The arrays of seeds were later imprinted onto silicon wafers coated with thermoplastic NanoImprint lithography resist (NXR-1025 2.5%) using a Nanonex universal imprinter system.

After the substrate was patterned with the square array of seeds, each period of

square spiral was deposited in four sequential steps, between which the substrate was rotated by $\delta\phi = 90^\circ$, as shown in a Figure 4.2. Four periods of TiO_2 square spiral were deposited on the array of seeds with 320 nm spacing. To prevent column broadening and bifurcation, the PhiSweep technique (see Chapter 1) was employed with 8 sweeps per one square spiral arm. Sweep angle of 26.5° was used as it maximizes shadowing between the columns and was shown to be optimal for the square spiral fabrication [115]. The deposition angle was kept constant at $\alpha = 86^\circ$.

4.3 Simulation and structure optimization

4.3.1 The model

Theoretical results described here are based on diamond:1 architectures, since they can be readily fabricated by GLAD method. Square spiral photonic crystals potentially exhibit a full 3D band gap between 4th and 5th bands, but if the column geometry is not optimal or the refractive index is too low, these bands overlap. We studied both direct and inverted structures, since the direct structures were experimentally fabricated, and inverted architectures have the material distribution more favourable for a 3D band gap formation. Inverted structure fabrication requires filling the porous film with a desired material and then etching away the columnar matrix that has originally been deposited by the GLAD method. In the model, the direct structures were represented by TiO_2 columns surrounded by air (or vacuum), and the inverted structures were built as arrays of air columns in a TiO_2 matrix.

The film's geometry was characterized by the lattice constant a , arm swing A , film volumetric density f_v and the column cross-section shape, as shown on Figure 4.3. It is also convenient to introduce the dimensionless parameters $\tilde{A} = A/a$, $\tilde{P} = P/a$, since for the optimized column geometry they will remain constant even when the seed lattice constant is changed. The volumetric density f_v is defined as a fraction of the crystal volume occupied by the column material, or as a ratio of crystal density to the bulk material's density. In simulations, the column cross-section was approximated as elliptical in the substrate plane with the ratio of major to minor axis $\eta = w_{\parallel}/w_{\perp}$, where w_{\parallel} is a cross-section width in

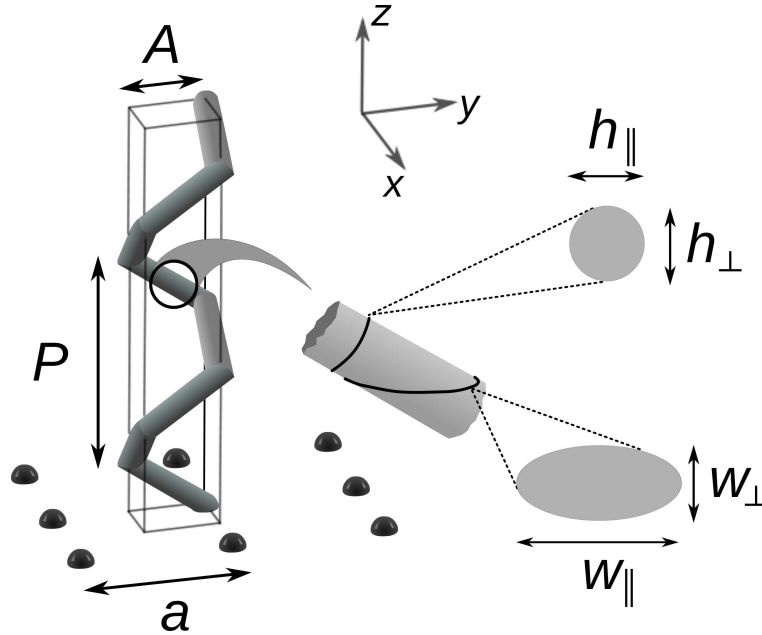


Figure 4.3: The model of square spiral

the column tilt plane, and w_{\perp} is a cross-section width normal to this plane. The cross-section in the plane normal to the column axis is then elliptical too, with the ratio of major to minor axis $\zeta = h_{\parallel}/h_{\perp}$, where h_{\parallel} and h_{\perp} are related to w_{\parallel} and w_{\perp} as:

$$h_{\parallel} = w_{\parallel} / \sqrt{\frac{16A^2}{P^2} + 1}; \quad h_{\perp} = w_{\perp}.$$

GLAD columns tend to have a cross-section elongated normally to the column tilt plane, but since square spirals were deposited with PhiSweep motion, cross-sections closer to circular can be expected. For this reason, when investigating the experimental film, we considered the column's cross-section to be circular. Silicon substrate and hemispherical seeds were taken into account, because the reflectivity is considerably affected by substrate presence, and the dielectric function for crystalline silicon [126] was approximated with the Lorentz approximation in FDTD. Both in the deposited film and in simulated columns, the spiral arm adjacent to the substrate was tilted in YZ plane, and spiral arms on the film's surface were tilted in XZ plane.

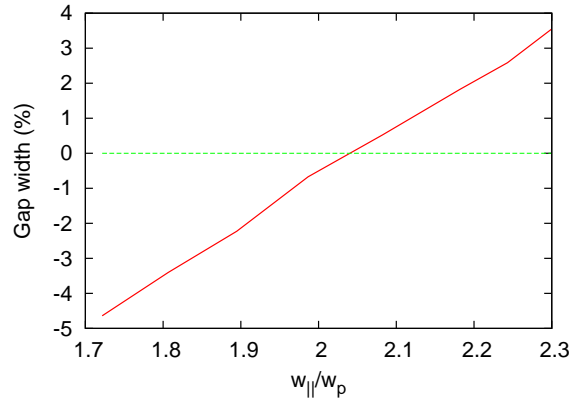


Figure 4.4: FDTD calculated band gap width as a function of cross-section elongation in the substrate plane for a direct square spiral optimized at $w_{||}/w_{\perp} = 2.3$ ($\zeta = 1$)

4.3.2 The role of column cross-section

In Ref. [122, 123] it was shown that photonic band gaps as wide as 5% can be produced in TiO_2 square spirals with diamond:1 architecture and circular arm cross-section in the plane normal to the column arm ($\zeta = 1$). Taking into account that the geometry in this work has been optimized for the silicon columns, TiO_2 columns can be further adjusted to produce even larger band gap. Wider 3D band gaps were found, for example, for columns with rectangular cross-sections and for the inverted columns [123]. These results, however, hold only as long as $\zeta = 1$. Figure 4.4 shows the simulated relative width of 3D photonic band gap (and band overlap, where this value is negative) as a function of cross-section broadening η for the TiO_2 spiral optimized for $\eta = 2.3$ ($\zeta = 1$). At $\eta = 2.3$ the band gap is close to 3.3% according to our simulations and with decreasing η its width decreases, and 3D band gap closes at $\eta < 2.04$. High value $\eta = 2.3$ can not be directly fabricated by the GLAD technique so far, and column cross-sections typical for GLAD films will not produce a complete 3D band gap unless more powerful techniques are developed to modify the cross-section geometry.

Inverted photonic crystals present much wider band gaps than their direct counterparts, therefore, the 3D band gap is easier to achieve. The dependence of the 3D band gap width on η in inverted square spirals is shown in Figure 4.5.

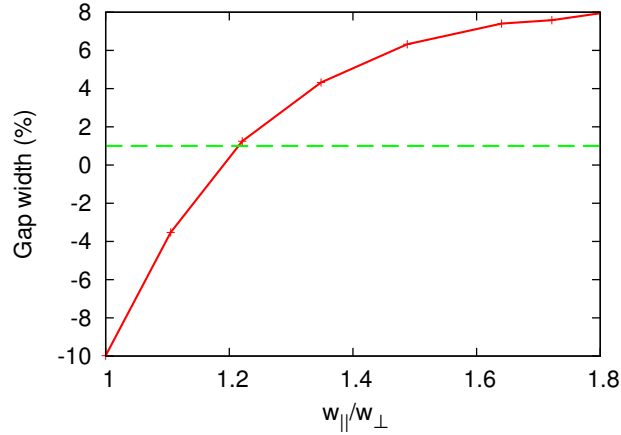


Figure 4.5: FDTD calculated band gap width as a function of cross-section elongation in substrate plane for direct and inverted square spirals optimized at $w_{\parallel}/w_{\perp} = 1.5$

Like in the direct architecture, the band gap width increases as the cross-sections become more elongated in the direction of the arm tilt. This structure has been optimized at $\eta = 1.5$, and characterized by the relative arm swing $\tilde{A} = 0.59$; vertical pitch $\tilde{P} = 1.5$, relative film density $f_v^{inv} = 28\%$, and column refractive index $n = 2.4$. The lowest value of η , needed for the full 3D band gap is then $\eta = 1.22$, much lower than that in the direct structures. The relative density of the corresponding direct structure is $f_v = 72\%$, is substantially larger than the density of the film described by the previous figure. However, the reduced arm swing \tilde{A} in the inverse columns requires lower deposition angle, which will increase the deposited GLAD film density. It is also possible to adjust the film's volume density after deposition, which was experimentally demonstrated for silicon microstructures. When silicon columns were oxidized, the total volume of the solid increased, because of the lower density of silicon dioxide [116].

4.3.3 Reflectivity of the square spiral films: comparison to the experiment

FDTD-simulated reflection spectra were compared to the experimental measurements for the film prepared by GLAD deposition combined with nanoimprint lithography of seeds. SEM image of TiO_2 square spiral, presented on Figure 4.6,

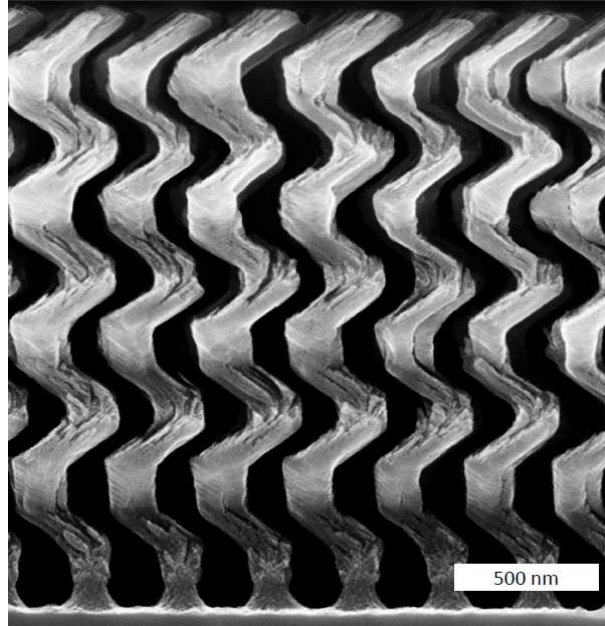


Figure 4.6: SEM image of the square spiral (courtesy of Joshua Krabbe)

was used to determine the experimental column geometry. From the SEM image, and by comparing simulated and measured reflectivity, the following values were found for the fabricated square spirals: vertical pitch $P = 470 \pm 5$ nm, arm swing $A = 170 \pm 7$ nm, lattice constant $a = 315 \pm 5$ nm, and titania volume fraction $f_v = 26 \pm 2\%$. S- and p-polarized reflection spectra were measured using variable wavelength spectroscopic ellipsometry for incidence angles ranging from 20° to 70° , and azimuth angles from 0° to 90° from the tilt plane of the arm nearest to the substrate.

Figure 4.7 shows the FDTD-simulated and experimentally measured p-polarized reflectance for four periods of square spiral deposited on a silicon substrate. The incidence angle is 20° from substrate normal, and the azimuth is 0° as measured from the tilt plane of the nearest to the substrate arm. The cross-section elongation $\eta = 1$ has been taken, based on the SEM image analysis, and on the assumption that PhiSweep deposited columns have a cross-section close to circular.

The simulated reflectance for nonabsorptive TiO_2 columns is substantially higher than the measured one, but all peak positions are in a good agreement with the measurements. This indicates that while geometry in the model accu-

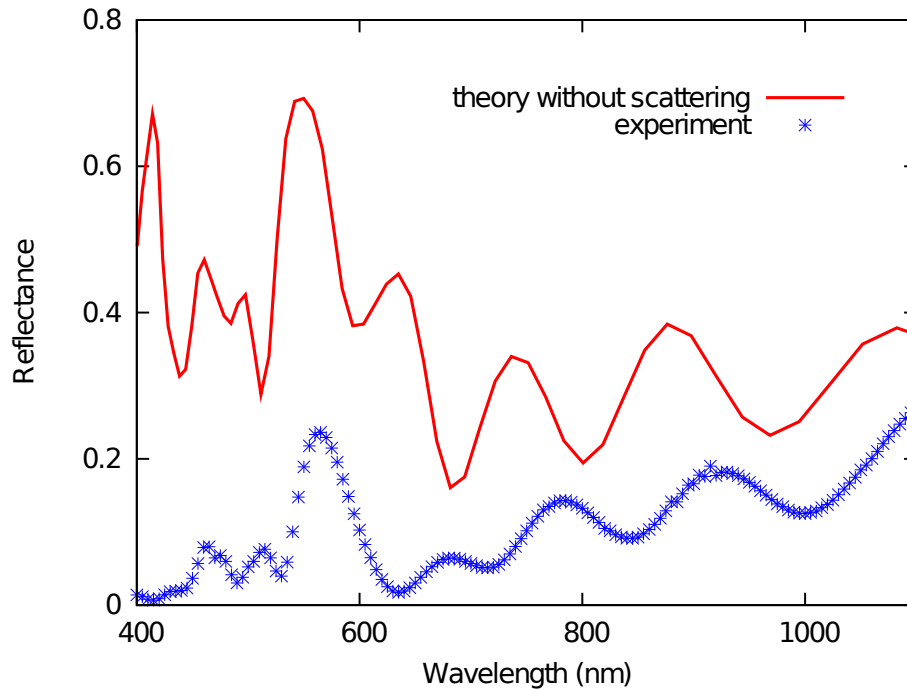


Figure 4.7: Simulated and experimental reflection spectra at 20° angle of incidence for p-polarized light.

rately represents the fabricated one, columns have a source of extinction, other than absorption in the column material, or in the substrate. The reflectivity loss can be explained by high scattering losses in the square spiral columns. Indeed, the intercolumnar distance is comparable to the wavelength, therefore random deviations in column positions will cause a diffuse scattering. As SEM image indicates, the column surface is also far from smooth, and may cause substantial diffuse scattering. The equipment used during the film characterization measured a specular reflectivity, and did not detect the diffusely scattered light, which ultimately reduced the measured reflection.

Accounting for the column roughness and growth disorders can be a very challenging task in simulations, but it is possible to describe the diffuse scattering losses by an artificial absorption coefficient, using the following considerations. The film's measured reflectance gradually decreases with the decreasing wavelength, therefore we can suggest that the dominant scattering mechanism is the Rayleigh scattering. In the GLAD square spirals, it occurs on the column surface roughness, as well

as on the density fluctuations inside the columns. Scattered light follows random paths in the film; therefore, we can consider that it does not participate in the formation of specular reflection spectrum.

Assuming that the light is scattered on the refractive index fluctuations, and that the characteristic scale of these irregularities is substantially smaller than light wavelength, one can introduce an artificial absorption coefficient as a measure of scattering loss [78]:

$$\alpha_s = \frac{8\pi^3}{3\lambda^4} \langle (\Delta\epsilon)^2 \rangle v_\epsilon$$

where $\langle (\Delta\epsilon)^2 \rangle$ is a dispersion of the dielectric constant ϵ , and v_ϵ is fluctuation correlation volume. The constants $\langle (\Delta\epsilon)^2 \rangle$ and v_ϵ are not known, but their product can be found by fitting the experimental data. The material's refractive index is then expressed as $n(\lambda) = n_0(\lambda) + j\sigma/\lambda^3$, where σ is an unknown coefficient, found by fitting the experimental data.

Because scattering occurs in the photonic crystal it is worth discussing the validity of the given approximation. On macroscopic level, scattering probability depends on the density of photonic states in the crystal: within photonic band gaps scattering is forbidden in some or in all directions, while on their edges, where group velocity is small, scattering probability is high. We introduce scattering extinction on the microscopic level, and in this way, its dependence on the density of states is naturally accounted for in the simulation. For example, in the directions where density of photonic states is low, light propagation is not supported, and scattering will be small. Conversely, where group velocity is small, scattering loss will be strong due to longer light interaction with the photonic crystal. The key assumption here is that any scattered light has an extremely small probability of being returned into specular reflected component, detected in observations. Different methods and expressions were developed for situations, where scattered light does not escape detection, such as in photonic crystal waveguides [51, 97].

Figure 4.8 shows the FDTD simulated reflectance at s- and p- polarizations for the columns with $\sigma = 0.175$ [eV⁻³]. The reflectance is in a good agreement with the experiment except for the shortest wavelengths, where the scattering features become comparable to wavelength and Rayleigh approximation is inaccurate. Simulated p-polarized reflectance in the band gap is approximately equal to the experimentally measured, while the simulated s-polarized reflectance in the band

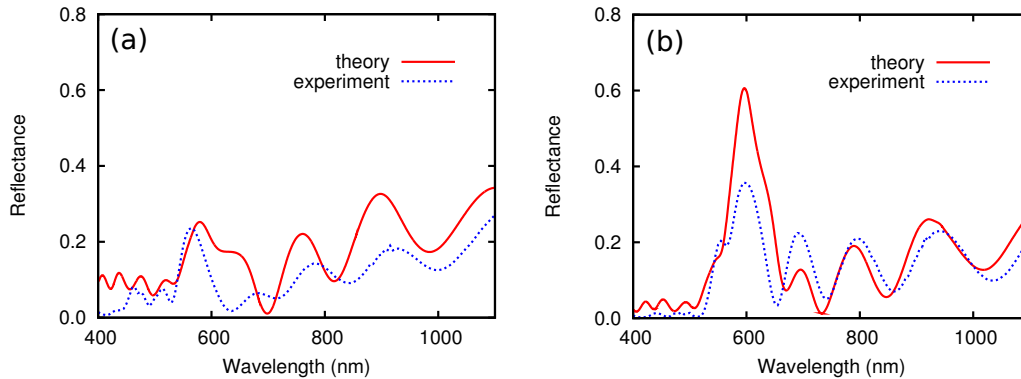


Figure 4.8: Simulated and experimental reflection spectra at 20° angle of incidence for p-polarized (a), and for s-polarized light (b)

gap is higher than the measured one.

Silicon seeds on the substrate also influence the reflection, but to a much smaller extent than diffuse scattering. Simulations with seeds have shown that silicon seeds slightly reduce the reflectivity as a whole, but their influence is strongest at longer wavelengths. At long wavelengths, the layer of seeds acts as an antireflective buffer between the columns and the substrate, since its refractive index is between the refractive index of porous titania, and bulk silicon. It reduces the reflection from the substrate and, consequently, increases the absorption in it. At wavelengths of the photonic band gap and shorter, Rayleigh scattering is so strong that relatively little light reaches the substrate after the first pass, therefore seeds have almost no impact on the blue end of the reflection spectra.

The reflectivity from the fabricated square spirals is relatively small in the band gap, because only four periods of the spiral were grown. The band gap development is shown on a Figure 4.9 with the increasing number of spiral turns. This figure shows the FDTD simulated x- and y-polarized reflectances for 4 and 10 turns of the square spiral at normal incidence. To see the picture unobscured by scattering, the simulations were done for nonabsorbing titania columns with the refractive index $n = 2.4$. We can see that at four turns, the band gap is poorly defined and severely distorted by Fabry-Perot resonances.

Despite the rotational symmetry of the square spiral columns and normal incidence, the x- and y-polarized reflectance spectra have different patterns of Fabry-Perot resonances. The difference is due to the film's anisotropy on the boundaries

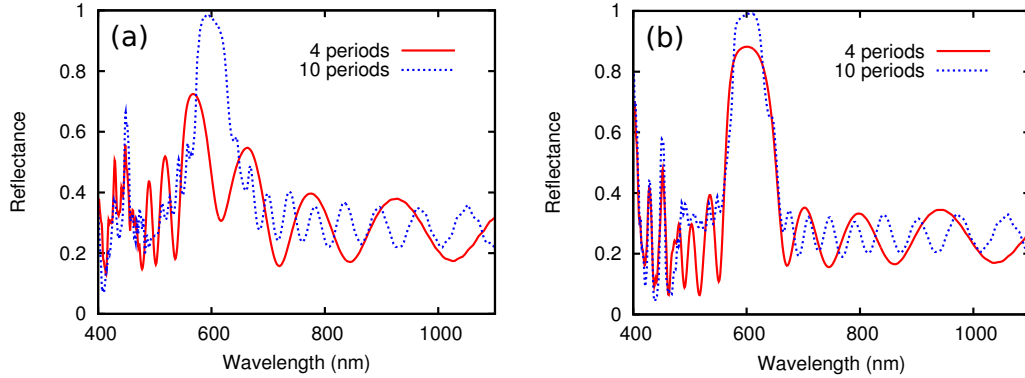


Figure 4.9: FDTD simulated p-polarized (a) and s-polarized (b) reflectance at normal incidence from 4- and 10-period square spiral film. Column geometry is fitted to the experimentally fabricated structure.

with the substrate and air. Working as polarization-dependent antireflective coatings, these portions of the crystal create different patterns of Fabry-Perot resonances for x- and y-polarized light. The x-polarized reflection band is suppressed by the resonant mode around $\lambda = 600$ nm, while the y-polarized mode has reflection above 80% even with four spiral turns. At 10 turns, band gaps are much better defined and the difference between the x- and y-polarized reflectances decreases.

Besides having a distinct band gap at normal incidence, the structure needs to preserve this band gap at all other propagation directions to be considered a true photonic crystal. Figure 4.10 shows simulated and measured p-polarized reflectivity as a function of altitude (angle measured from substrate plane to the incident beam) and wavelength, and Figure 4.11 shows simulated reflectivity for the s-polarized light. The simulated reflectivity is given for the film with the scattering strength $\sigma = 0.175 eV^{-3}$. We can see that the band gap does not cover any single frequency in the whole range of altitudes, indicating that it is not a full 3D band gap. The FDFD calculated band diagram of the same square spiral, shown on Figure 4.12, confirms this. The gap between the 4th and the 5th bands exists in the directions ΓZ , ΓR and ΓX , but in all of them it is centered at different frequencies. Also there is no band gap between 4th and 5th bands for the ΓA and ΓM directions.

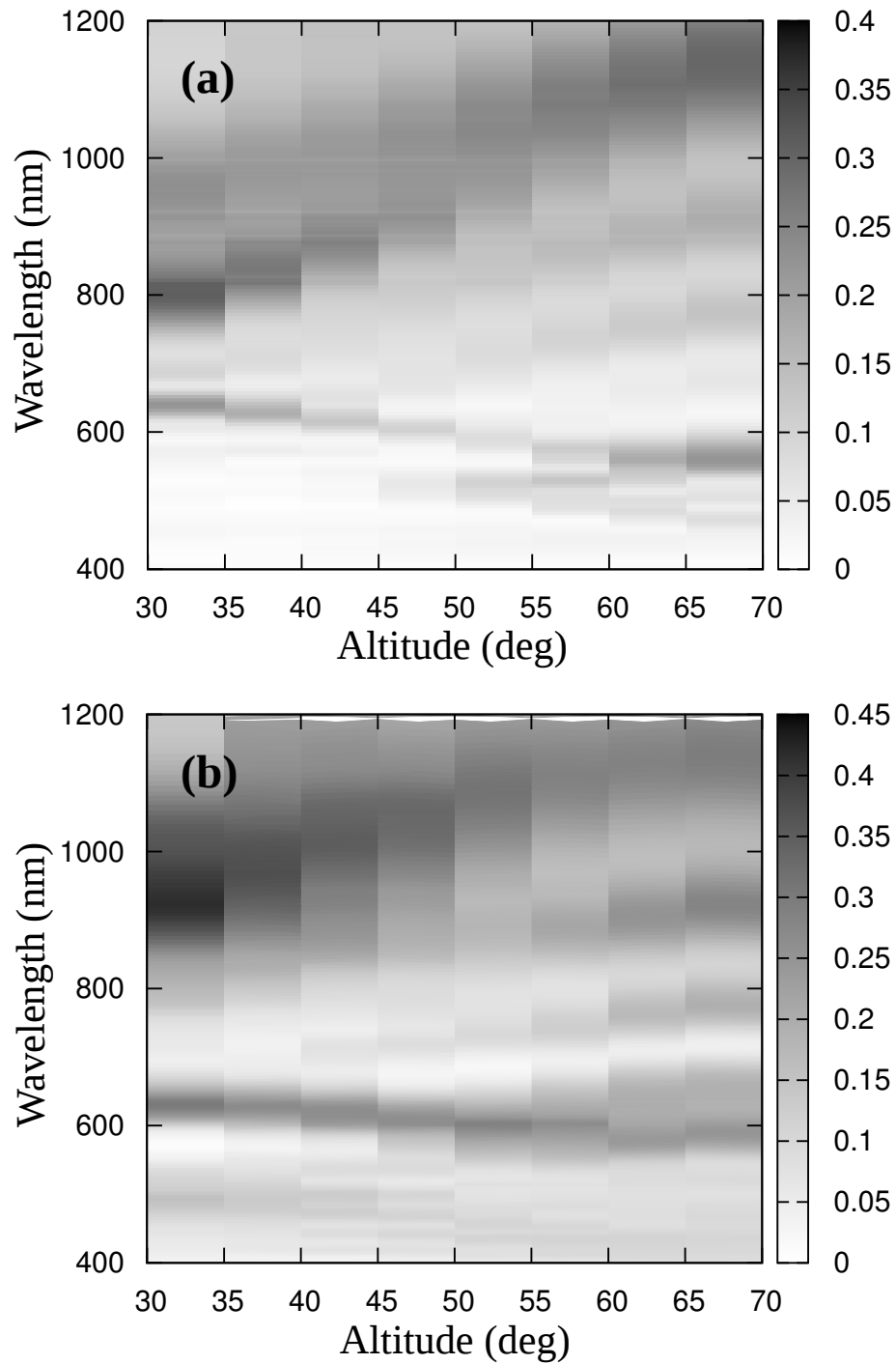


Figure 4.10: Measured (a) and FDTD simulated (b) p-polarized reflectance as a function of incidence angle and wavelength. Pitch $P = 468$ nm, lattice constant $a = 314$ nm, arm swing $A = 164$ nm and filling fraction $f_v = 25\%$ (circular column cross-section).

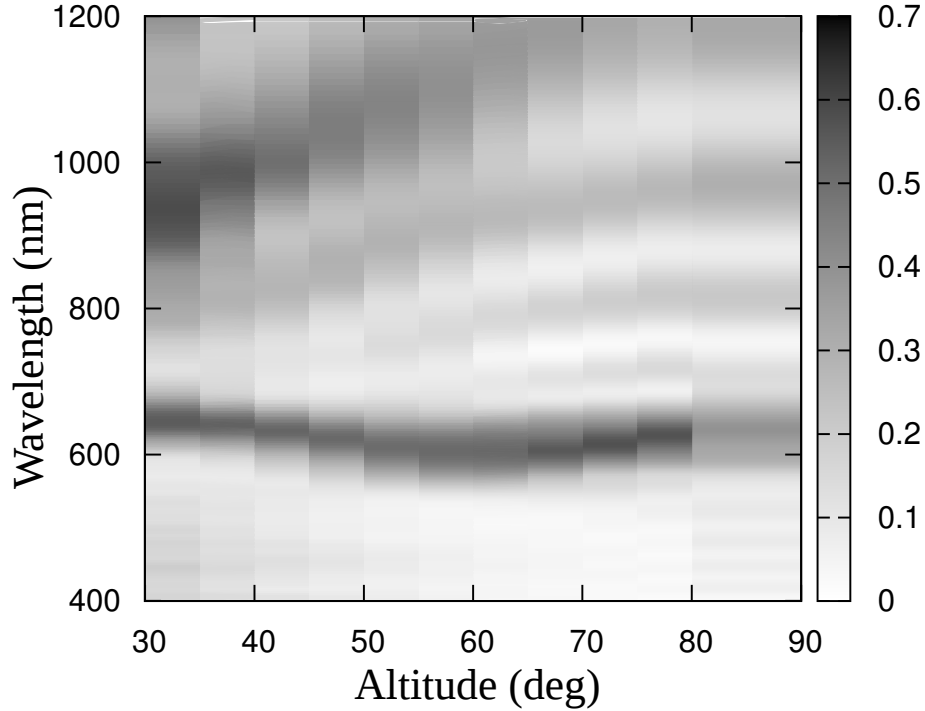


Figure 4.11: FDTD simulated s-polarized reflectance as a function of incidence angle and wavelength for the fabricated film.

4.3.4 Band gap optimization and inverted square spirals

The fabricated structure can be still optimized in terms of column cross-section and density to improve the band gap. A series of frequency domain calculations were performed to optimize the titanium dioxide square spirals, and for the circular cross-sections the overlap between the 4th and 5th bands was minimized at the volume fraction of TiO_2 $f_v = 35\%$. However, this overlap is still as large as 12% of the wavelength. Therefore, with circular cross-sections, titania square spirals do not possess a 3D band gap.

As we have seen in Figure 4.5, the inverted square spirals require much less elongated cross-sections, therefore fall closer to the range accessible with GLAD method. Figure 4.13 shows the band structure for the optimized inverted square spirals at cross-section broadening $\eta = 1.5$. These columns with optimized relative pitch $\tilde{P} = 1.5$, arm swing $\tilde{A} = 0.59$ and volume fraction of titania $f_v^{inv} = 28\%$, have a 5.3% wide 3D band gap, limited by the 5th band in ΓR direction, and by the 4th

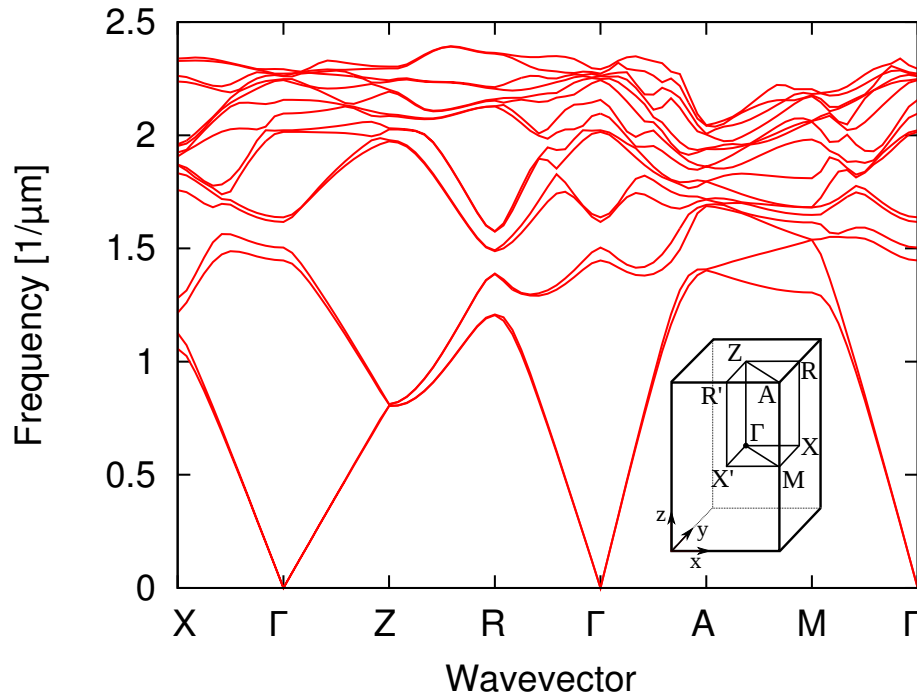


Figure 4.12: FDFD band structure for the experimentally fabricated square spirals.

band in ΓA direction. Inverse square spirals were previously produced from silica by oxidizing silicon columns [116]. This process has not been used for TiO_2 , and neither have the titanium square spirals ever been fabricated. However, the ability of silicon columns to change volume, as they are oxidized, can be potentially used wherein the direct structure of the optimal density will be produced by oxidizing silicon columns, and then filled with titanium dioxide to form the inverted crystal.

4.3.5 Improving the 3D band gap by density redistribution in the film

A diamond lattice of closely packed spheres and its inverse derivative have band gaps up to 27.3% wide (for the inverted diamond lattice of spheres in the matrix with dielectric constant 11.9) [123], which is wider than the band gap in the optimized square spirals made of the same material. Material in square spirals is evenly distributed along the column, but if it is redistributed and concentrated around lattice nodes, one may expect that the photonic crystal performance will be close

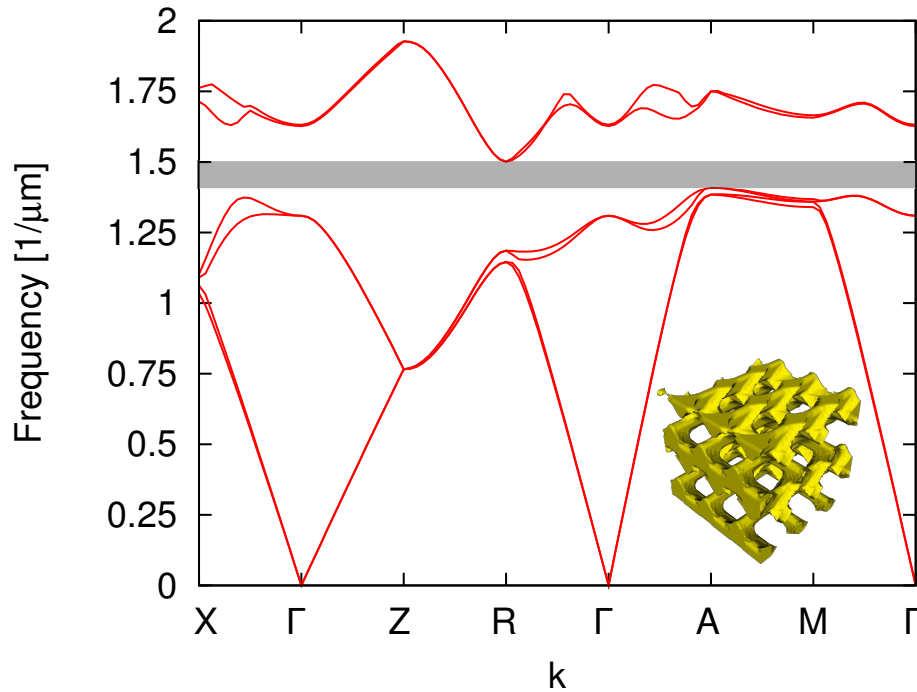


Figure 4.13: FDFD band structure for the inverted titania square spiral optimized for $\eta = 1.5$.

to the one of diamond lattice of spheres. The structure's band gap properties, thus may improve. Exploiting such a material redistribution to improve the 3D band gap in the TiO_2 square spiral is of particular interest, since band gap width in this structure is narrow, and even small deviations of spiral geometry from the optimal lead to the band gap closure.

Film density can be varied by varying the deposition angle. But if the deposition angle is varied, the column tilt angle also changes following the equation (1.1). The slow-corner method may be used to build up material at the corners of the spiral without altering the column tilt. In this method, the transition from one arm to the other in the square spiral corner is done gradually, rather than as an abrupt 90° turn, allowing for a more gradual transition and resulting in fewer defects [63]. Larger material accumulation at the spiral corners comes as a side effect of this technique. For simplicity, let consider straight column arms regardless of the variable column density, assuming that (i) if density variation is small, column tilt will not significantly vary; (ii) if density variation is large, the main influence

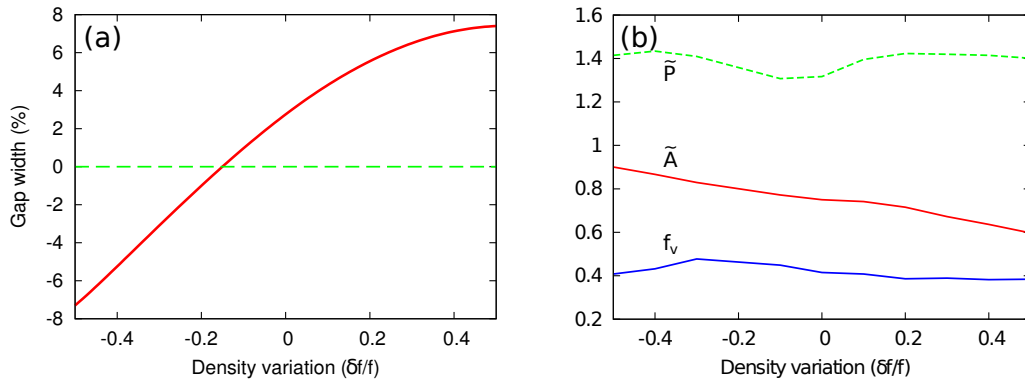


Figure 4.14: FDFD calculated band gap width (a) and optimized geometry (b) for the direct square spiral as a function of density variation along the substrate normal.

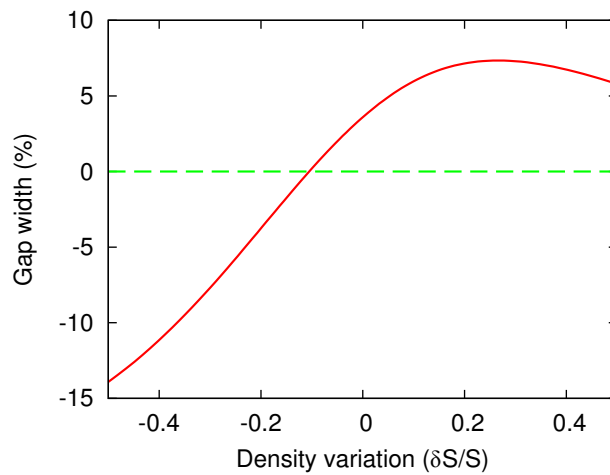


Figure 4.15: Band gap width as function of density variation for the inverted structure

on the band gap would be from dense parts, thus changing the tilt of connecting bars will not change the result qualitatively. In the model, the film's volumetric density was varied along the substrate normal as $f(z) = f_v[1 + \delta f \cos(\frac{8\pi z}{P})]$, where z is vertical coordinate in nanometers.

Figure 4.14(a) shows the relative band gap width as a function of δf for the direct square spiral with cross-section elongation factor $\eta = 2.3$ ($\zeta = 1$). At positive δf values, the material is concentrated around the arm joints, which correspond to the nodes of the diamond lattice. At negative values of δf , material is concentrated

in the arms, rather than on the joints. The 3D band gap width increases with positive δf , and decreases when $\delta f < 0$, indicating that material concentration around the spiral bends is favourable for 3D band gap formation. The band gap width saturates at 7.3% for the higher positive values of $\delta f \approx 0.5$.

In general, the optimal combination of arm swing, pitch, and film density depends on the distribution of material along the arms. Therefore, the square spiral geometry was optimized for each δf value shown on Figure 4.14. Figure 4.14(b) shows the optimized values of arm swing, pitch and density as a function of δf . The average optimized film density remains approximately constant, close to 40% of a bulk TiO_2 density, and the pitch \tilde{P} is increasing both at positive and negative δf values. The relative arm swing \tilde{A} on the other hand, gradually decreases with increasing δf , becoming close to $\tilde{A} = 0.9$ at $\delta f = -0.5$ and $\tilde{A} = 0.6$ at $\delta f = 0.5$. Smaller values of \tilde{A} may be more favourable for the GLAD fabrication, since with smaller column tilt one can have a wider control over the film density and cross-section shape. PhiSweep and spin-pause techniques are most capable of modifying the cross-section geometry and film density at smaller column tilts.

The dependence of 3D band gap width on the column density variation was also calculated for an inverted square spiral with a cross-section elongation $\eta = 1.5$. The result is similar to the one obtained for the direct structure, but here with the increasing δf the band gap width reaches maximum at $\delta f = 0.22$ and decreases at higher values.

4.4 Chapter summary

As we can see from the discussion above, design and fabrication of the square spiral photonic crystal in the visible spectral range is challenging due to the small refractive index contrast and inability of modern fabrication techniques to reach the optimized parameter range, especially with respect to the column cross-section geometries. Focusing on the inverted architectures, and varying the film's density, however, allowed us to optimize the architecture further and to bring it close to the fabrication capabilities of GLAD technique. Films with variable density have nonzero 3D band gaps even at small cross-section elongations falling into the range of PhiSweep technique. The GLAD method is armed with a number of techniques, that allow to control fine features of the column geometry. These

would allow one to further adjust the material distribution and cross-section shape. By combining the advanced GLAD methods and numerical modelling we can now foresee successful realization of square spiral photonic crystal with the band gap in the visible range.

Chapter 5

Metals in GLAD films and refractive index engineering

5.1 Motivation

In chapters 2 and 3, dense column arrays were used to design films with anisotropic effective dielectric constant, and polarization dependent band gap properties. Since these films were made with dielectrics, the values of their principal refractive indices occupied the range between the refractive index of column material and the refractive index of air, and the films did not have any magnetic response.

The motivation of this chapter was to consider a three-dimensional GLAD architecture as a support for ordered metal particles, and to extend their dielectric and band gap properties beyond the range that can be attained with solely dielectric columns. Metals have a negative real part of the dielectric permittivity, characteristic of systems with free electrons in their crystal lattice. When they are mixed with dielectrics the composites may have a wide range dielectric constants – from negative to positive, allowing one to engineer a desired refractive index. Unbound electrons, which move freely in response to the applied electric field, are also responsible for the composite’s magnetic response.

Such composites might be used, for example, as transparent conductors, the demand for which increased with advent of touch screen and flat panel displays. The electrical circuitry of these displays inevitably absorbs part of the passing light and reduces the image brightness. Conductive materials that are transparent to

the visible light solve this problem. Several conductive oxides were discovered in the last decades of the twentieth century, such as indium tin oxide (ITO), fluorine doped tin oxide (FTO), and indium zinc oxide (IZO) [32]. A growing problem with them, however, is high price and scarcity of indium.

Conductive nanowire networks emerged recently as a cheaper alternative to ITO films [83]. They are built of silver or carbon nanofibres loosely covering the substrate surface. With an appropriate surface density of conductive filaments most of the light is transmitted, and the conductivity is sufficiently high. In other applications, such as solar cells, current travels normally to the surface, and three-dimensional transparent networks may be required. Here, GLAD films have a potential due to their columnar structure. Mixed with metals they may be conductive and transparent at the same time. It was shown both theoretically and experimentally that arrays of metallic posts can be highly transparent in the infrared and red visible frequencies [31]. The conductivity of metal posts can be much higher than that of randomly linked networks, because they create direct current pathways from top to the bottom of the film. This can be used to collect and transport electric charges in relatively thick solar cells without losing too much incident light to absorption.

Another interesting role for the 3D structured metals is metamaterials with a negative refractive index. In these materials, both dielectric permittivity ϵ and magnetic permeability μ are negative. The refractive index, defined as a square root of their product $n = -\sqrt{\mu\epsilon}$, is then real but negative. The negative sign appears due to a negative direction of the energy flow, since with negative ϵ and μ , the Poynting vector is antiparallel to the wavevector \vec{k} [133, 132]. Due to the negative refraction, light rays coming from a point above a planar surface are focused on the opposite side of this surface. Thus, negative index slab acts as a superlens, free of many optical aberrations. These lenses are promising for photolithography where they can transfer an image to the photoresist at a high resolution [95].

Metamaterials have nonzero magnetic susceptibility due to the current loops in structured metal arrays. Metal particles act as magnetic atoms that are able to polarize magnetically in response to time-varying electric field. The first experimental realization of metamaterial with negative refractive index has been made at microwave frequencies in a form of a 3D array of metal loops mixed with the

array of straight wires [109]. The loops acted as magnetic atoms, leading to a negative permeability, while wires ensured a negative dielectric permittivity. Negative permeabilities were later shown in the visible frequencies [77].

Refractive index engineering with metal-dielectric composites can definitely go beyond these examples, and can be used either to design high index materials, materials with wide flat absorption spectra [70, 7], or other materials with unusual values of permittivity and permeability. For this reason, metallic nanocomposites lately received a lot of attention from researchers. Numerous works study the resonant transmission and absorption in metamaterials [30, 31, 6], but relatively few address the effective dielectric properties and derive the effective permeability and permittivity explicitly. In [35], for example, dielectric constants were calculated by matching the impedance of uniform slab with known dielectric properties to the nanocomposite structure, and showed negative permeability at visible frequencies for one layer of periodically arranged metal particles. Their method requires a presence of strong magnetic response ($\mu \neq \mu_0$) in the composite, and therefore cannot be used for all nanostructured materials. The explicit values for μ and ϵ were also theoretically calculated for metallic photonic crystals using complex-band-structure calculations [125], as well as characteristic matrix formalism combined with transfer matrix scattering calculations [110].

Recently, negative refractive index was reported in GLAD deposited silver slanted posts [53]. These results, however, were given for only three wavelengths and therefore provide little information about any trend. It is also hard to judge the accuracy of these results from only three data points, and therefore they need both theoretical and experimental verification.

In this chapter, the FDTD simulation is combined with the characteristic matrix formalism to explicitly calculate the effective μ and ϵ for GLAD architectures. Simulations were used here to show the existence of the magnetic response in vertical post metallic structures and to analyze them in the prospect that these nanostructures can be fabricated in future as columnar GLAD films. Also, multilayer GLAD films were considered as band gap materials and as polarizers, and their experimental realization is discussed here and compared to the simulated results.

5.2 Dielectric properties of materials from transmission and reflection

Composite materials are characterized by effective dielectric permittivity $\tilde{\epsilon} = \epsilon_0\epsilon$ and magnetic permeability $\tilde{\mu} = \mu_0\mu$ (where ϵ_0 and μ_0 are permittivity and permeability of free space), if the elements of the composite and spacing between them are much smaller than the wavelength of interest. For spherical or elongated particles in a dielectric medium, the relative permittivity ϵ can be approximated with effective medium theories. These theories express the material's polarizability as a function of components' polarizabilities and their volume fractions. One of the most popular is the Maxwell-Garnet theory [86], giving a dielectric constant for a dilute arrangement of monodispersed spherical particles (or a square lattice of cylinders). Newer and more sophisticated theories, such as Bruggeman [12] and other approximations describe polydispersed systems and elliptical particles [82, 93]. All approximations, however, are limited to relatively simple particles such as spheres, ellipsoids and tubes. Complex geometries including helices, coils or combinations of different shapes are best described numerically.

In Chapter 3, FDFD calculated dispersion relations were used to find the refractive index of columns as a function of their volume fraction in the film. The dispersion relations only gave information about the refractive index $\sqrt{\mu\epsilon}$, but did not allow us to separate μ and ϵ . In dielectric structures, we can always assume $\mu = 1$, therefore, the information provided by dispersion relations is sufficient. In structures with metals, however, the magnetic permeability is not necessarily unity, because of the induced currents.

It is possible to find both ϵ and μ from the transmittance and reflectance of the slab of known thickness. Suppose we have a slab of a composite material of thickness d . A plane wave of frequency ω is passing normally through this slab. FDTD simulation gives transmitted $t = t' + j t''$ and reflected $r = r' + j r''$ amplitudes for this plane wave, which can be used with characteristic matrix formalism (Chapter 3) to find the slab characteristic admittance:

$$Y = \sqrt{\frac{\epsilon_0\epsilon}{\mu_0\mu}}$$

and refractive index:

$$n = \sqrt{\mu\epsilon}.$$

Assuming that the slab is surrounded by air on both sides the characteristic matrix expressions for transmittance and reflectance are written as:

$$t = \frac{2Y_0}{Y_0 \cos(\phi) + j\frac{Y_0^2}{Y} \sin(\phi) + jY \sin(\phi) + Y_0 \cos(\phi)} \quad (5.1)$$

$$r = \frac{Y_0 \cos(\phi) + j\frac{Y_0^2}{Y} \sin(\phi) - jY \sin(\phi) - Y_0 \cos(\phi)}{Y_0 \cos(\phi) + j\frac{Y_0^2}{Y} \sin(\phi) + jY \sin(\phi) + Y_0 \cos(\phi)}, \quad (5.2)$$

where $\phi = k_0 \cdot d \cdot \sqrt{\mu\epsilon}$, and $Y_0 = \sqrt{\epsilon_0/\mu_0}$. We can regroup the variables to write these expressions as:

$$2Y_0 \frac{1}{t} = Y_0 \sqrt{1-s^2} + j\frac{Y_0^2}{Y} s + jY s + Y_0 \sqrt{1-s^2} \quad (5.3)$$

$$2Y_0 \frac{r}{t} = Y_0 \sqrt{1-s^2} + j\frac{Y_0^2}{Y} s - jY s - Y_0 \sqrt{1-s^2}, \quad (5.4)$$

where $s = \sin(\phi)$. They have common terms with different signs, and can be substantially simplified by taking their sum and difference:

$$Y_0 \gamma = Y_0 \sqrt{1-s^2} + jY s \quad (5.5)$$

$$\sigma = \sqrt{1-s^2} + j\frac{2Y_0 s}{Y} \quad (5.6)$$

where:

$$\gamma = \frac{1-r}{t} \text{ and } \sigma = \frac{1+r}{t}.$$

Variables Y and s are now easily separated, giving a biquadratic equation for the slab characteristic admittance:

$$Y^4 \cdot (1 - \sigma^2) + Y^2 \cdot 2Y_0^2(\sigma^2 + \gamma^2 - \gamma\sigma - 1) + Y_0^4(1 - \gamma^2) = 0. \quad (5.7)$$

With known Y , the parameter s can be calculated as:

$$s = j\frac{Y Y_0}{Y_0^2 - Y^2}(\gamma - \sigma). \quad (5.8)$$

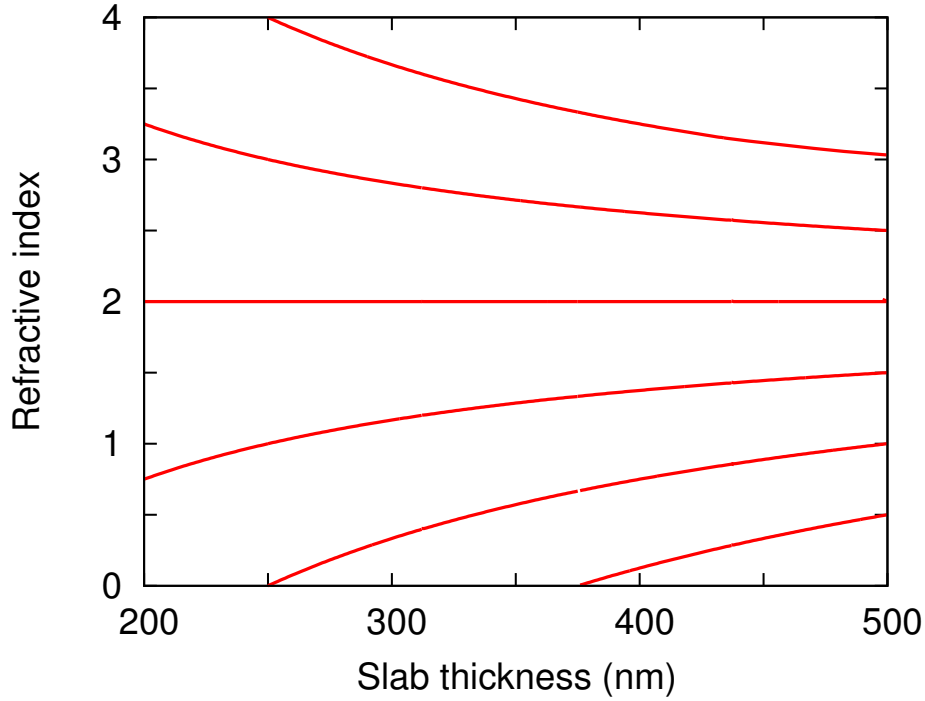


Figure 5.1: Solutions of characteristic matrix equations for a 200 nm thick slab with refractive index $n = 2$.

The admittance Y is a material property, therefore it is uniquely determined and does not depend on the slab thickness. The refractive index, however, has a spectrum of solutions:

$$n_{eff} = \frac{\arcsin(s) + 2\pi m}{k_0 d},$$

only one of which is a true solution. The solution for n_{eff} can be refined if two slabs of different thickness are considered. The true index is the one that does not change with slab thickness d , as illustrated on Figure 5.1. Also when the dielectric function is calculated as a function of wavelength, the true solution will often (but not always) converge to a constant value at $\lambda \rightarrow \infty$. In practice, the value of m cannot always be found from numerical solutions, due to simulation inaccuracy, especially where the dielectric function does not converge to a constant at $\lambda \rightarrow \infty$.

Instead of determining n_{eff} from the transfer matrix equations, it is sometimes practical to find it from dispersion relations, as a slope of the dispersion curve:

$$\sqrt{\epsilon\mu} = c k/\omega.$$

The later is uniquely defined, and can be used in conjunction with Y to determine ϵ and μ . When used only for the admittance Y , the characteristic matrix equations are simplified by considering the reflection from a planar slab of infinite thickness. The equations then reduce to a well known formula:

$$Y = Y_0 \frac{1 - r}{1 + r}. \quad (5.9)$$

In FDTD, the reflection from such a slab can be simulated if the slab boundary opposite to the light source is submerged into the absorbing PML layer. The wave is then suppressed before reaching this boundary, and does not participate in the reflection.

Submerging the boundary in PML layer, however, has its own disadvantages. PML has a numerical reflection coefficient, which is lowest at normal incidence. If the slab is uniform and continuous, the wavefront remains planar, but if the slab consists of particles, they scatter light at angles to the PML surface, increasing the numerical reflection. Especially where fields change abruptly, such as near the surface of metal particles, this causes a significant numerical error. The problem is alleviated if the PML absorption coefficient is turned on gradually over a long distance. In the limit where PML increases over an infinite distance the numerical reflection vanishes according to the adiabatic theorem. This, however, requires very thick PML layers.

5.2.1 Effective medium approximations

A number of theories exist that express the effective dielectric properties of composite materials in terms of their components' fractions, and the particle aspect ratio. These theories are based on an assumption that the composite material can be divided in cells much smaller than the wavelength of light. Then if the composite around any of these cells is replaced with an effective medium with an appropriate dielectric constant, light will pass through this cell without scattering. Mathematically, this means that the scattering amplitude from a single particle surrounded by ϵ_{eff} has to be equal to zero in the direction of the incident beam.

Two frequently used effective medium theories are Maxwell-Garnett and Brug-

geman approximations. The Maxwell-Garnett approximation can be derived¹ if a unit cell is treated as an ellipsoidal particle of medium A coated with a shell of medium B [93], and surrounded by a uniform medium ϵ_{eff} . The fraction of material A in the particle is equal to its fraction in the mixture. In a small particle limit, the effective dielectric constant satisfies an equation:

$$\frac{\epsilon_B - \epsilon_{eff}}{\epsilon_{eff} + L(\epsilon_B - \epsilon_{eff})} + f \frac{\epsilon_A - \epsilon_B}{\epsilon_B + L(\epsilon_A - \epsilon_B)} = 0 \quad (5.10)$$

where f is a fraction of material A in the composite, and L is a depolarization factor, depending on the particle aspect ratio. For spherical particles $L = 1/3$, while for thin discs $L = 1/2$. This formula is asymmetric with respect to materials A and B, and works well only in a small particle limit, where particles A are suspended in the host material B. The approximation becomes invalid when particles A are large and partially overlap with each other.

In the Bruggeman approximation, the unit cell is also represented as an ellipsoidal particle, but it is entirely composed of either material A or material B [12, 34, 93]. Scattering amplitudes S for the particles A and B are added, multiplied by the fractions of corresponding materials $S = fS(A) + (1 - f)S(B)$, and their sum is equated to zero:

$$f \frac{\epsilon_A - \epsilon_{eff}}{\epsilon_{eff} + L(\epsilon_A - \epsilon_{eff})} + (1 - f) \frac{\epsilon_B - \epsilon_{eff}}{\epsilon_{eff} + L(\epsilon_B - \epsilon_{eff})} = 0. \quad (5.11)$$

This approximation is symmetric with respect to materials A and B, and sometimes describes dense composites better than MG approximation.

These two approximations can produce considerably different results, pointing to the limitations of effective medium theories. Today, they are often replaced with numerical simulations, but remain popular as simple predictive tools, which help one design composite materials with desired dielectric properties.

Theories involving more complex particle shapes emerged in the later decades of the 20th century, including approximations for slanted post arrays [18]. It is worth mentioning here the approximation for hollow tubes, which was written for carbon nanotubes, and may be used for coated GLAD columns. The tube is

¹A number of derivations exist for the Maxwell-Garnett approximation including the original one by J. C. Maxwell Garnett [86, 104]

replaced with a uniform column that has an effective dielectric constant:

$$\epsilon_t = \epsilon_3 \frac{1 + K}{1 - K}, \quad (5.12)$$

where

$$K = \frac{(\epsilon_2 - \epsilon_1) \cdot (\epsilon_2 + \epsilon_3) \rho^2 - (\epsilon_2 - \epsilon_3) \cdot (\epsilon_2 + \epsilon_1)}{(\epsilon_2 - \epsilon_1) \cdot (\epsilon_2 - \epsilon_3) \rho^2 - (\epsilon_2 + \epsilon_3) \cdot (\epsilon_2 + \epsilon_1)},$$

$\rho = R_{in}/R_{out}$ is the ratio between inner and outer tube radius, and ϵ_1 , ϵ_2 , and ϵ_3 are the dielectric constants of tube core, tube wall, and tube surroundings respectively [82].

5.3 Refractive index engineering in the columnar metal films

At sufficiently long wavelengths, the material dispersion remains nearly constant in a wide spectral range. In dielectrics, only permittivity can be controlled at these frequencies, and magnetic susceptibility is nearly zero. In metals, we can expect that the magnetic response will present itself as well. At shorter wavelengths, light diffraction and interference come into play, but dielectric properties still can be described in terms of effective values. In principle, it is possible to assign an effective permittivity and permeability to a periodic structure, even within the band gap [1]. Because the dispersion relations are not continuous there, the structure may have a non-zero effective magnetic susceptibility, and negative refraction [117]. It is hard to admit these structures as true metamaterials, however, because at band gap frequencies, the wavefront of a plane wave is not preserved, and refracted light in photonic crystal represents Bloch waves rather than refracted plane waves. Therefore, it is desirable to observe the magnetic response at wavelengths exceeding the interparticle distance.

To analyze the effective dielectric and magnetic properties of closely packed metalodielectric composites, light transmission was simulated through the composite slabs of various thickness, and the characteristic matrix formalism was employed to find the permittivity and permeability. We can anticipate several possibilities depending on the combination of ϵ and μ . When both ϵ and μ are positive, the material is a conventional dielectric, but by changing the imaginary part of per-

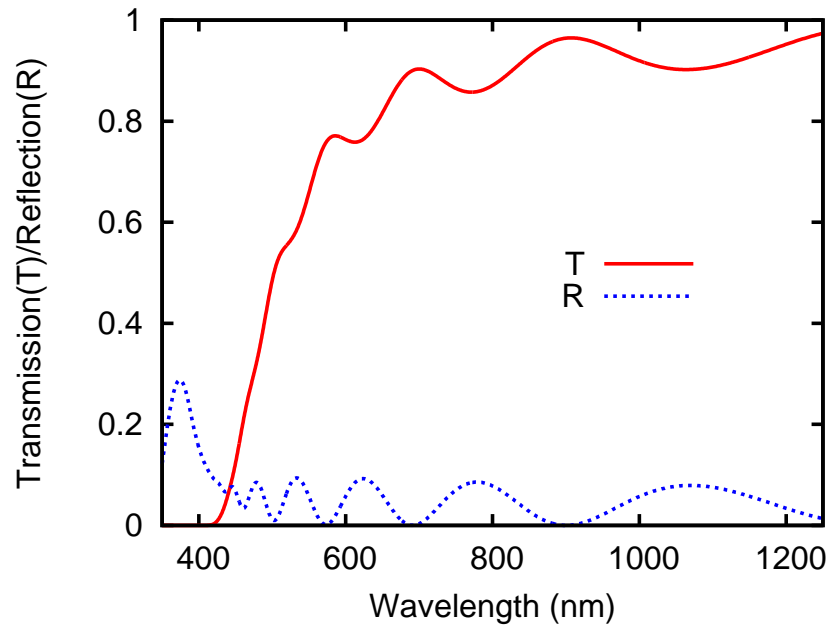


Figure 5.2: FDTD simulated transmission and reflection from the silver vertical posts in square array, with a lattice constant $a = 100$ nm and column diameter $D = 0.5a$.

mittivity and permeability, it is possible to control the absorption spectrum. The reflectivity becomes small if the real part of the composite's characteristic admittance is close to the free space admittance. If $Y \sim Y_0$ over a wide spectral range, and absorption is large, the structure will have a wide flat absorption spectrum, needed in black body emitters. The real part of the dielectric constant in these materials is typically close to, or below unity: $Re(\epsilon) = n^2 - k^2 \lesssim 1$. When both ϵ and μ have a negative sign, a negative reflection is possible.

5.3.1 Vertical posts

The simplest structure that can be considered as a metallic metamaterial, and accessible with GLAD technique, is an array of posts – tilted or vertical. Resonant absorption in arrays of vertical metallic posts has been considered in a number of works previously, since various methods exist that can be used to fabricate these structures [6, 31]. Therefore, it is well known that these arrays can be highly transparent in the infrared, and have an absorption band in the visible range. In

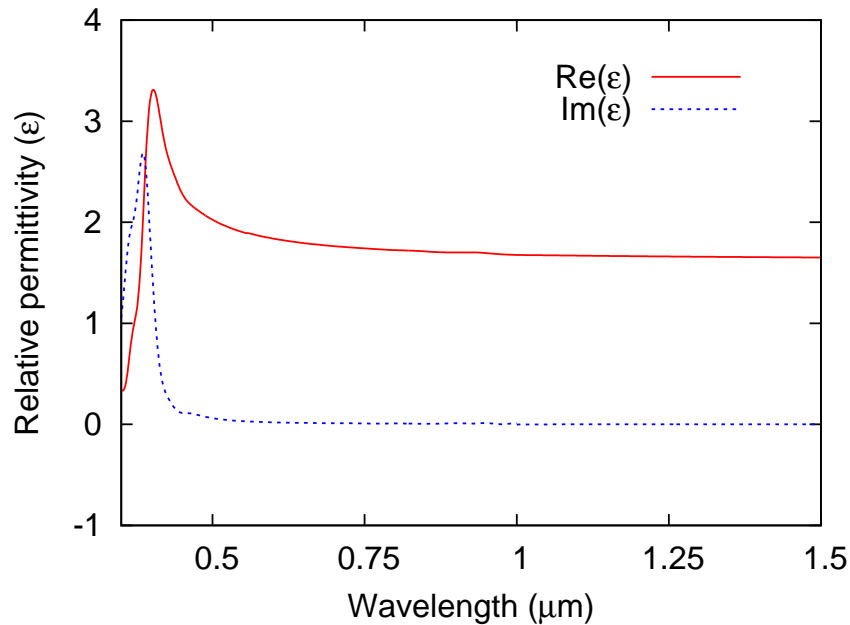


Figure 5.3: FDTD calculated dielectric permittivity for silver vertical posts in square array with lattice constant $a = 100$ nm and diameter $D = 0.5a$.

this thesis, the source of this absorption is addressed through the effective dielectric properties of these films.

Figure 5.2 gives the transmission and reflection from a $1\ \mu\text{m}$ thick vertical post film arranged in a square array with a lattice constant $a = 100$ nm. The film has high transmittance and low absorption in the infrared, but in the mid-visible and ultraviolet range the absorption increases. These properties can be understood if we take a look at the effective dielectric constant of silver posts. Figure 5.3 gives the real and imaginary parts of the effective dielectric constant, calculated using the equations (5.7-5.8). The real part of the permittivity asymptotically approaches a constant value $\epsilon_\infty = 1.63$ at long wavelengths, and its imaginary part is then vanishingly small. In the infrared, it is a weakly absorbing dielectric with a nearly constant refractive index $n = \sqrt{1.63}$. The dispersion increases at shorter wavelengths, and has a resonance absorption peak at 430 nm. At even shorter wavelengths the real part of the permittivity becomes smaller than one and smaller than the imaginary part, leading to high total absorption in this range. The resonance peak redshifts as the vertical posts become thicker and almost touching,

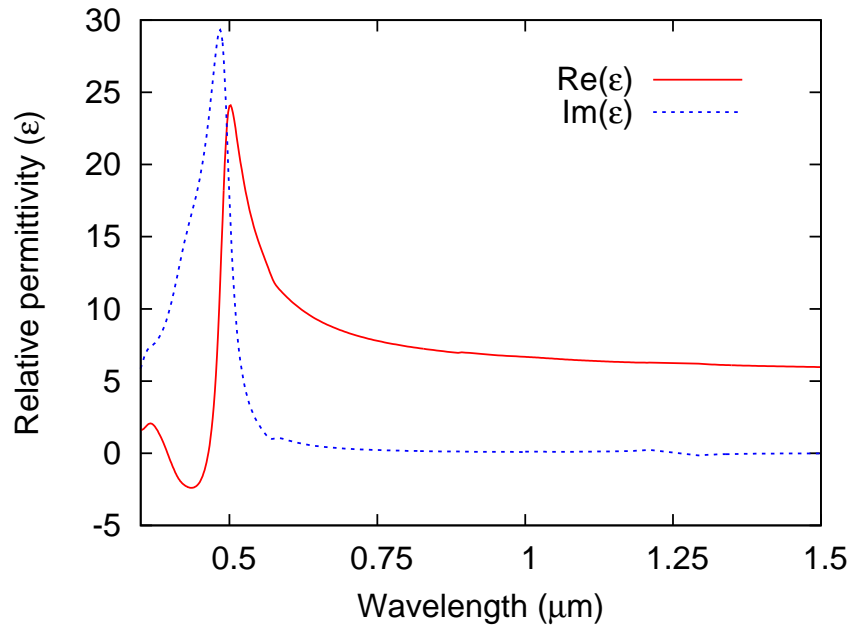


Figure 5.4: FDTD calculated dielectric permittivity for silver vertical posts in square array with lattice constant $a = 100$ nm and diameter $D = 0.9a$.

as shown in Figure 5.4. Here the column diameter is $D = 0.9a$ and we can see that the dielectric function briefly becomes smaller than zero on a blue side of the resonance, but positive further in the ultraviolet. In the dielectric limit ($\lambda \rightarrow \infty$) the permittivity is $\epsilon_\infty = 5.64$.

5.3.2 Effective medium approximation

To analyze the origin of the resonance, consider the dielectric function calculated with the effective medium approximation. As we can see in Figure 5.5, the effective medium theory agrees well with the simulation of Figure 5.4, therefore, we can use this model to analyze the resonance. The effective permittivity here was calculated using a Maxwell-Garnett approximation, and the same dielectric function of silver as in the FDTD simulation. The permittivity swing near the resonance is larger in the effective medium approximation than in the simulations, but in the dielectric limit, the permittivity is relatively close to the simulated: $\epsilon_\infty = 6.40$. As in the simulation, the permittivity on a blue side of the resonance becomes negative, and

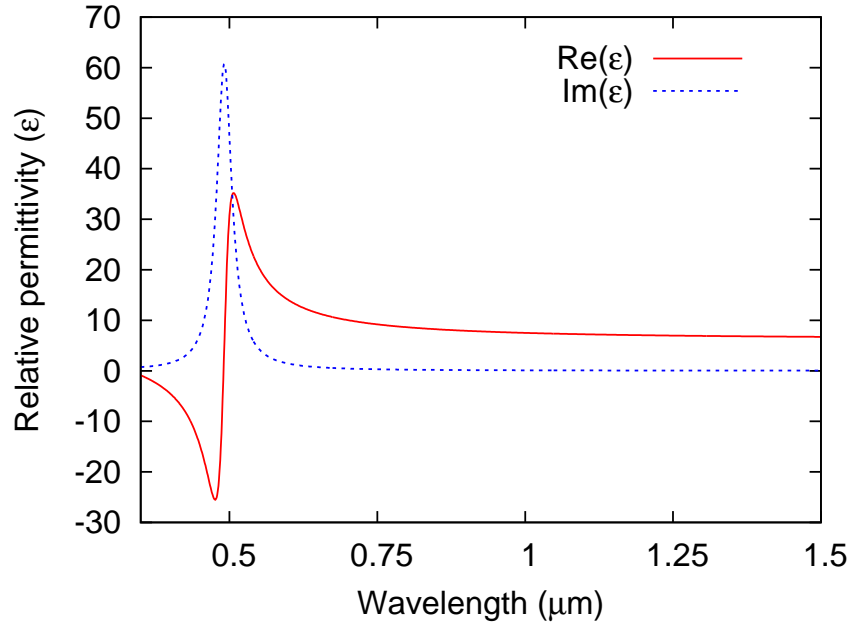


Figure 5.5: Effective medium approximation for the dielectric permittivity of silver vertical posts in square array with lattice constant $a = 100$ nm and diameter $D = 0.9a$.

then gradually “recovers” at shorter wavelengths.

The resonance is located close to the spectral band where silver loses its metallic properties due to the inter-band absorption. It is, therefore, not obvious whether the peak is produced by the plasma resonance, or by silver bound charges. To eliminate this ambiguity, consider the effective dielectric function of the vertical posts made of nonabsorbing metal with the same plasma frequency as in silver (dielectric function, shown on Figure 5.6(b)). The dielectric function of this metal is described by a Drude model:

$$\epsilon_m = \epsilon_\infty \left(1 - \frac{\omega_p^2}{\omega^2 - j\gamma\omega} \right), \quad (5.13)$$

where ω_p is plasma frequency, ϵ_∞ is the dielectric constant at infinitely high frequency, and γ is the relaxation frequency.

Figure 5.7 shows the effective medium approximation for the real part of the dielectric function of vertical posts, made from this nonabsorbing metal. Since

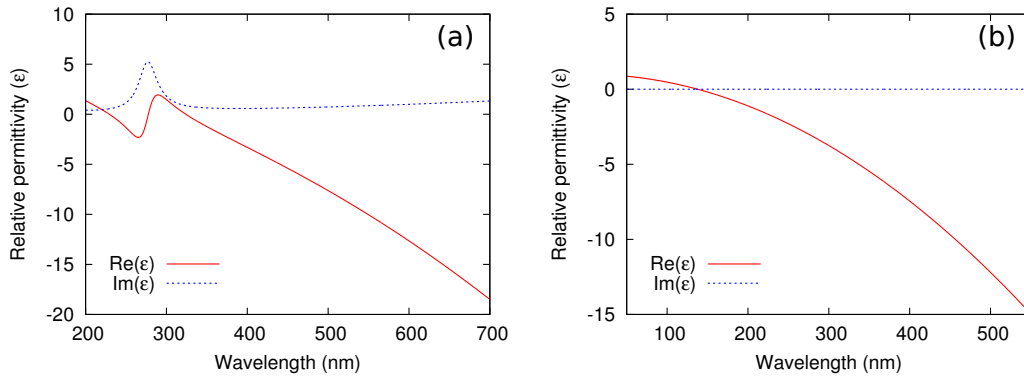


Figure 5.6: Dielectric function of silver (a), and of the Drude metal with the same plasma frequency $\omega_p = 9.01$ eV (b) (dielectric function for silver is taken from Ref. [99])

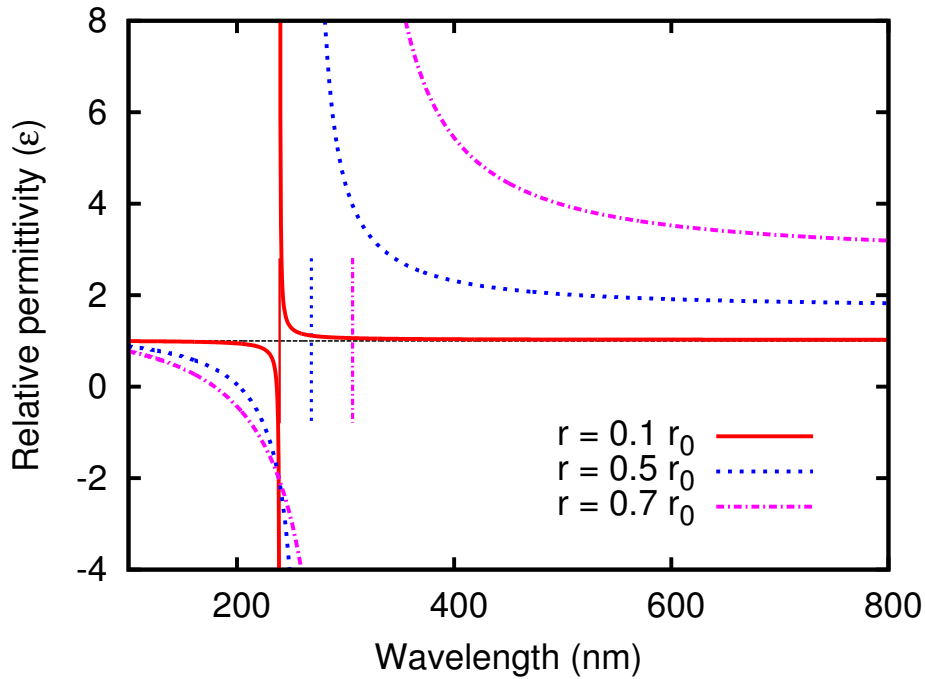


Figure 5.7: Effective medium approximation for the dielectric permittivity of vertical posts made of nonabsorptive metal with the plasma frequency of silver, calculated for material to void ratios $f = 0.1, 0.5$ and 0.7 . Vertical lines indicate the resonance wavelength for each graph.

there is no absorption, the imaginary part of the dielectric function is not shown. The real part of the effective permittivity has a distinct discontinuity, which red-shifts with the increasing post diameter. On the red side of this discontinuity, the derivative $d\epsilon/d\lambda$ is negative, and permittivity converges to a constant value. For all post diameters the infrared permittivity stays above $\epsilon = 1$. On the blue side of the resonance, the permittivity is strongly negative near the discontinuity, and converges to $\epsilon = 1$ from below, as λ decreases.

The resonant peak is representative of the absorption by bound charges in the dielectric media, but here charge is bound by the nanoparticle (column in our case). Effectively, the ordered array of columns responds to light as a dielectric composed of atoms with a certain inter-band frequency ω_1 . Substituting (5.13) into (5.10) we can express the effective permittivity for columns or spheres made of a Drude metal:

$$\epsilon_{col} = \epsilon_{cl} \left[A + \frac{B}{\omega_1^2 - \omega^2 - j\gamma\omega} \right], \quad (5.16)$$

where

$$A = \frac{1 + 2f - \epsilon_{cl}(2f - 2)}{1 - f + \epsilon_{cl}(2 + f)},$$

$$B = \frac{9f\epsilon_{cl}\omega_p^2}{(1 - f + \epsilon_{cl}(2 + f))^2},$$

$$\omega_1 = \frac{\omega_p(1 - f)}{1 - f + \epsilon_{cl}(2 + f)},$$

ϵ_{cl} is a relative permittivity of material that fills space between the columns, and f is the columns' volume fraction in the film. The damping constant γ in the composite remains the same as in the Drude metal, but the dielectric function does not have terms describing the unbound electron cloud. The resonance frequency ω_1 is proportional to the plasma frequency ω_p and depends on the columns' volume fraction. In the limit $f \rightarrow 0$, the resonance frequency approaches $\omega_1 \rightarrow \sqrt{\frac{\omega_p}{1+2\epsilon_{cl}}}$, which is $\sqrt{3}$ times smaller than ω_p if $\epsilon_{cl} = 1$. When $\lambda_p = 138$ nm, this gives $\lambda_1 = 2\pi c/\omega_1 = 238$ nm, as seen on Figure 5.7. When $f \rightarrow 1$, the approximation (5.16) gives $\omega_1 \rightarrow 0$, but the Maxwell-Garnett approximation is only accurate at small fractions f . Simulations show no resonance when columns overlap with each other, as surface plasma excitations can no longer travel between them.

The columnar metallic structure presents many opportunities for refractive

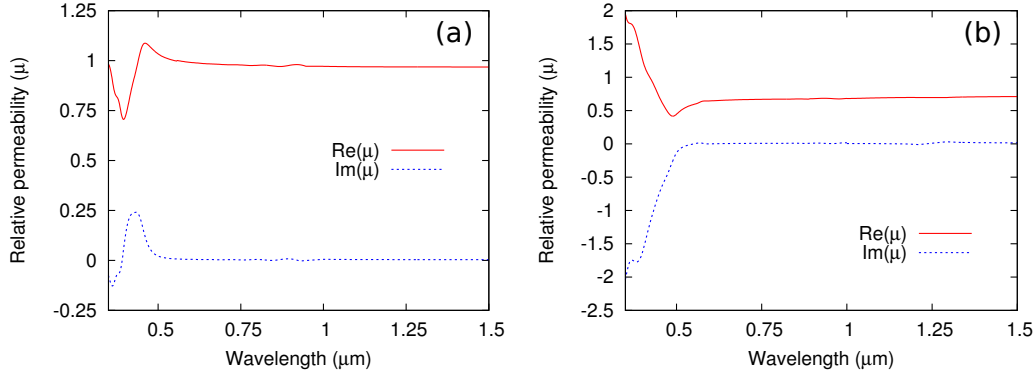


Figure 5.8: FDTD calculated magnetic permeability for silver vertical posts in square array with lattice constant $a = 100$ nm and diameter (a) $D = 0.5a$, and (b) $D = 0.9a$.

index engineering. At long wavelengths ($\omega \rightarrow 0$), it has a response of a nearly nonabsorbing dielectric with adjustable permittivity, while at wavelengths smaller than the resonance ($\omega \gg \omega_1$) the material is highly absorptive and nearly non-reflective, and can be used as a black body absorber. In the limits $\omega \rightarrow 0$ and $\omega \rightarrow \infty$, the effective dielectric constant becomes purely real:

$$\lim_{\omega \rightarrow 0} \epsilon_{col} = \epsilon_{cl} \frac{1 + f(1 - 2f) + \epsilon_{cl}[2(1 - f)^2 + 9f\omega_p]}{(1 - f)[1 - f + \epsilon_{cl}(2 + f)]}$$

and

$$\lim_{\omega \rightarrow \infty} \epsilon_{col} = \epsilon_{cl} \frac{1 + 2f + 2\epsilon_{cl}(1 - f)}{1 - f + \epsilon_{cl}(2 + f)}$$

and the absorption vanishes even if $\gamma \neq 0$. At small f this dielectric constant is close to ϵ_{cl} in both frequency limits.

5.3.3 Magnetic response

FDTD simulations go beyond the effective medium theory, as they predict the effective medium response even at large densities $f \rightarrow 1$, and describe the material's magnetic permeability. Figure 5.8 shows the magnetic permeability of a silver vertical post film as a function of wavelength for the same geometry as in Figures 5.3 and 5.4. The magnetic response oscillates near the resonance frequency, and at long wavelengths slowly increases, remaining below unity ($\mu_{eff} < 1$).

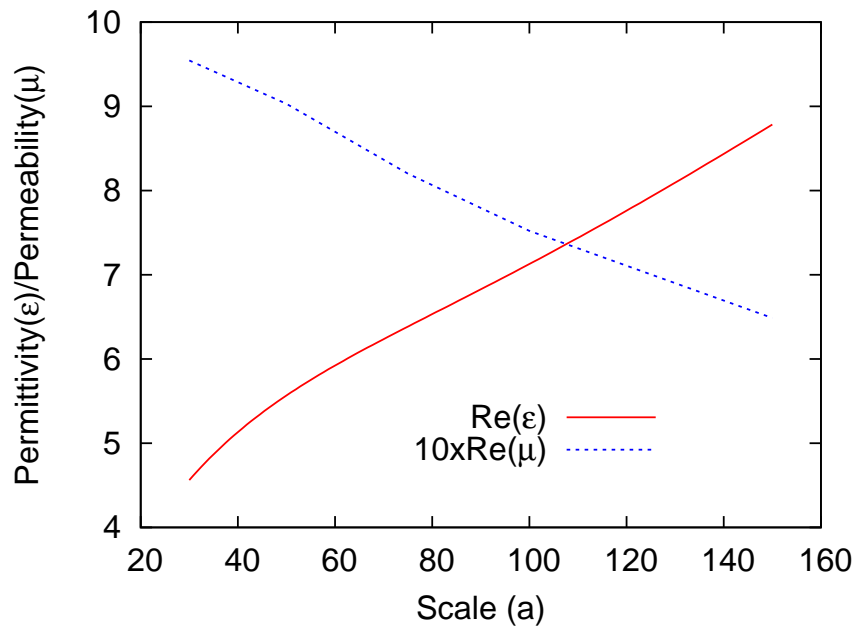


Figure 5.9: Permittivity and permeability of vertical posts as a function of intercolumnar distance (column diameter is $D = 0.9a$).

Unlike the effective medium approximation, simulations show that both permittivity and permeability depend on the intercolumnar distance, even if the volume fraction of metal in the film remains constant. Figure 5.9 shows the real part of the permittivity and permeability at $\lambda = 2000$ nm as functions of the intercolumnar distance a , while the column diameter is proportional to the intercolumnar distance: $D = 0.9a$. The smaller a is, the weaker is the magnetic response ($\mu \rightarrow 1$). The permittivity also decreases, whereas in the effective medium approximations it did not depend on scale. The parameter that remains constant, at least in a wide range of scale factors, is the refractive index $n = \sqrt{\mu\epsilon}$. At $\lambda = 2000$ nm, it remains close to $n \sim 2.3$ in the whole range between $a = 30$ nm and $a = 150$ nm. The change in the permittivity and permeability is due to the scale dependent magnetic response of the material. The magnetic response of the vertical post film can be interpreted as a result of circular currents in a shallow layer below the column surface. The electric field has time varying gradients both normal to the surface (due to the dipole interaction between columns) and parallel to the column (due to the field oscillation along the wavevector). These currents are similar to

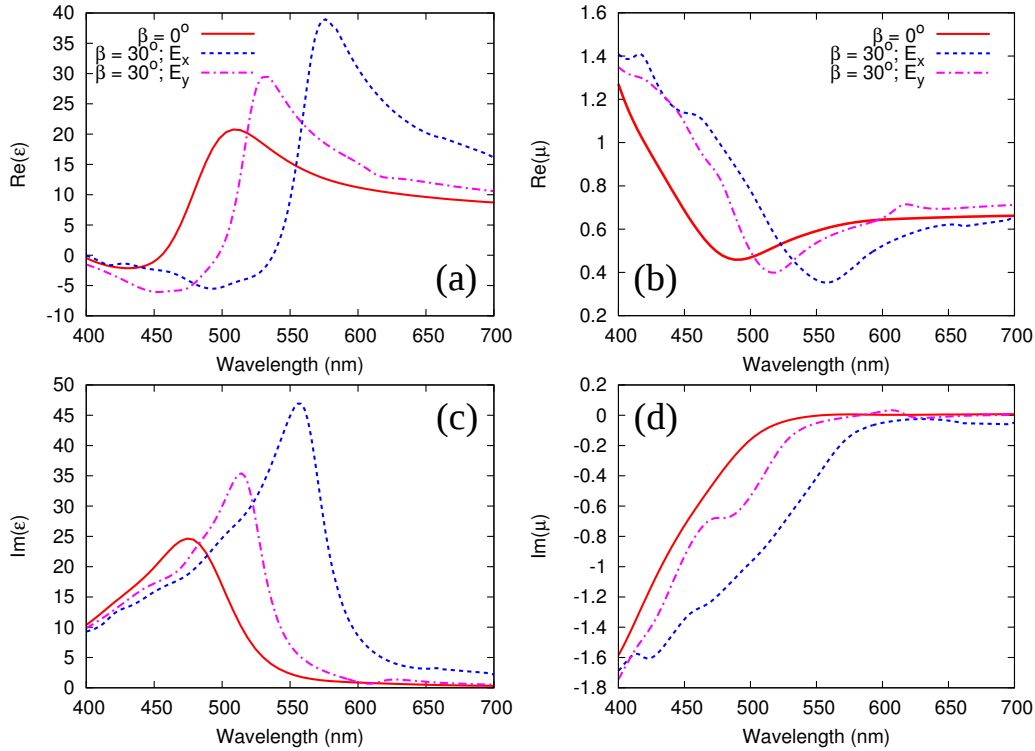


Figure 5.10: Permittivity [real (a) and imaginary (c)], and permeability [real (b) and imaginary (d)] for silver post tilted at $\beta = 0^\circ$ (vertical) and $\beta = 30^\circ$. Columns are arranged in a square array with lattice constant $a = 100$ nm, and column diameter $d = 0.9a$.

those responsible for a skin effect in metal wires. When the array is dense, the magnetic contours are too small to cause a significant magnetic response, but in large scale structures, or at high frequencies the magnetic susceptibility increases.

The dielectric and magnetic response of the columnar films is anisotropic, therefore it is polarization dependent in the arrays of slanted posts. Figure 5.10 shows μ and ϵ for vertical and slanted posts in two polarizations: E_x , where the electric vector is in plane of the column tilt; and E_y , where the electric vector is normal to this plane. Dielectric constant were calculated here at normal incidence for the columns arranged in a square array with lattice constant $a = 100$ nm, and column diameter $D = 90$ nm. The column cross-section is circular in a substrate plane for both vertical and slanted posts. Both, x- and y-polarized resonances are redshifted in slanted posts compared to the vertical columns, but the y-polarized

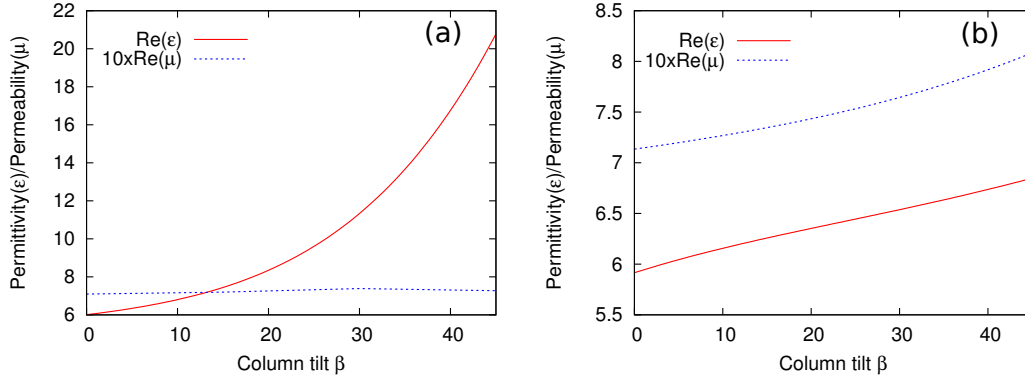


Figure 5.11: Permittivity (a) and permeability (b) of slanted posts as a function of column tilt at $\lambda = 1500$ nm ($a = 100$ nm, $D = 0.9a$).

dispersion is affected less by the column tilt. Near the resonance, the magnetic permeability decreases, but remains positive. It is smaller in tilted columns, as well as in columns of larger size (see Figure 5.9), suggesting that sufficiently large structure, consisting of highly tilted columns may have a negative permeability in a narrow spectral band. Such a large system was not simulated here due to its larger demand on computer memory and simulation times.

In the infrared, both ϵ and μ asymptotically converge to constant values. Figure 5.11 shows the real permittivity and permeability as functions of the column tilt β at wavelength $\lambda = 1500$ nm. In E_x polarization, the permittivity ϵ increases strongly with the column tilt, while in the orthogonal E_y polarization its change is relatively small. The infrared permeability is similar in both light polarizations, slightly increasing with the column tilt (since it is below unity, this means that the magnetic response decreases). As a consequence of a strong polarization selectivity in tilted columns, we can expect that the helically twisted columnar films will exhibit a circular Bragg phenomena, similarly to the dielectric films. The transmission and reflection from these structures is an interesting problem, apart from the effective dielectric properties of metallic composites, because their optical response depends not only on the effective dielectric constant of the film, but also on the surface roughness and plasmon excitation on the column tips. This question deserves a separate study, going beyond the limits of this chapter, and effective medium theories. Helical columns also may have a strong magnetic response and

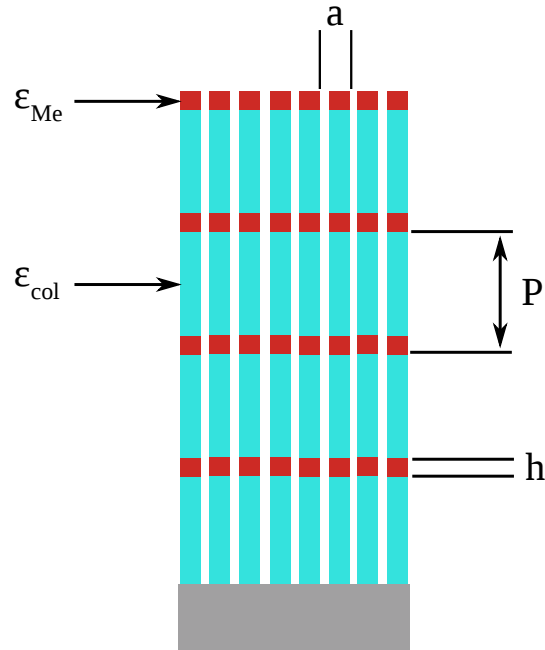


Figure 5.12: The theoretical model of vertical posts with metal inclusions.

were studied in the literature as candidates for negative index materials [30, 80].

5.4 Ordered particles in GLAD films

GLAD columns form an excellent matrix for three-dimensional arrays of metal particles. Because columns can be both vertical or tilted, and the tilt is easily varied during the column growth, particles can form various three-dimensional grids. As it was shown above, the array of metallic columns can have a very large refractive index values, therefore if it is included into the dielectric film in periodic layers, the film may produce strong band gaps. The optical anisotropy of metallic columns can also be used to design thin film polarizers.

Consider a model of a vertical post film with metal nanoparticles inserted in equidistantly spaced layers, as shown on a Figure 5.12. Such layers can be added into the film if the evaporant material is briefly switched from dielectric to metal. The whole deposition can be performed in a single deposition step, if two evaporant sources are employed, or in several deposition steps, if only one source is available at a time.

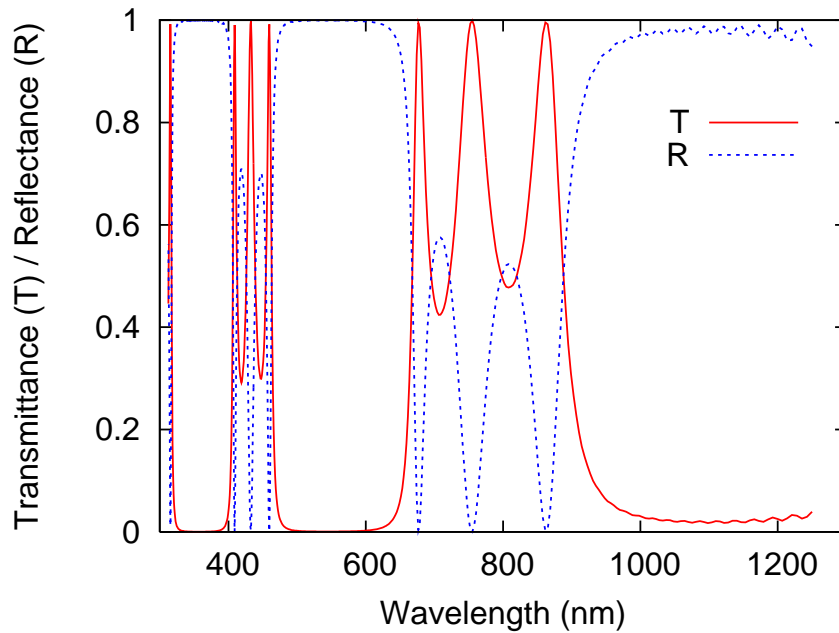


Figure 5.13: FDTD simulated transmission and reflection through four layers of nonabsorptive metal particles suspended in air (Vertical pitch $P = 500$ nm, in-plane particle separation $a = 120$ nm, particles are discs with radius $r = 50$ nm and height $h = 70$ nm).

5.4.1 Arrays of the ideal metal particles

To analyze these particle arrays it is convenient to consider a nonabsorptive “ideal” metal described by eq. (5.13) with plasma frequency much larger than any frequency of interest, and damping constant much smaller than plasma frequency. Then the transmission and reflection spectra are not affected by wavelength-dependent absorption. For the visible (and infrared) spectral range a plasma wavelength $2\pi c/\omega_p = 40$ nm was chosen with $\gamma = 10^{-5}\omega_p$. It is several times smaller than in realistic metals and damping constant is at least two orders smaller, therefore the visible spectral response of this material is similar to the mid-infrared response of silver or gold.

Figure 5.13 shows the transmission and reflection spectra in the visible spectral range for the four layers of nonabsorbing metallic particles arranged in arrays with lattice constant $a = 120$ nm. The distance between layers is 500 nm, and each particle is a disc with radius 50 nm and thickness 70 nm. Because the particles are

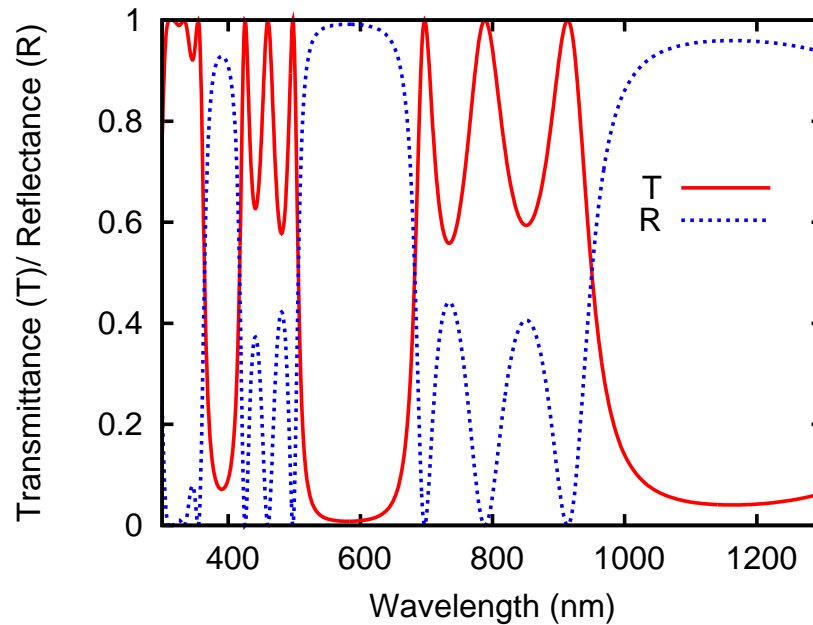


Figure 5.14: Transfer matrix calculated transmission and reflection through four layers of effective medium with dielectric constants obtained with Maxwell-Garnet approximation for the metal cylinders 50 nm in radius, separated by $a = 120$ nm (each layer is 70 nm thick and distance between layers is $P = 500$ nm).

nonabsorbing, the difference between the transmission and reflection intensities shows a simulation error, which was less than two percent along the simulated spectral range – highest near the band gap edges, where the group velocity is small. The spectrum shows a series of distinct band gaps, separated with a series of sharp transmission peaks. The peaks are Fabry-Perot resonances, and their number between each two gaps is $N - 1$, where N is a number of metal layers.

The notable difference between dielectric interference mirrors and periodic sequence of porous metal layers is a large width and depth of photonic band gaps achieved with a small number of reflecting surfaces. However, each layer of porous metal can be effectively represented as a dielectric slab. Figure 5.14 shows the transmission and reflection spectra for the four 70 nm thick layers of material with the refractive index calculated using the Maxwell-Garnett approximation. The spectra on Figures 5.13 and 5.14 are very similar. Because the nonabsorptive metal was used, imaginary part of the effective refractive index is close to zero,

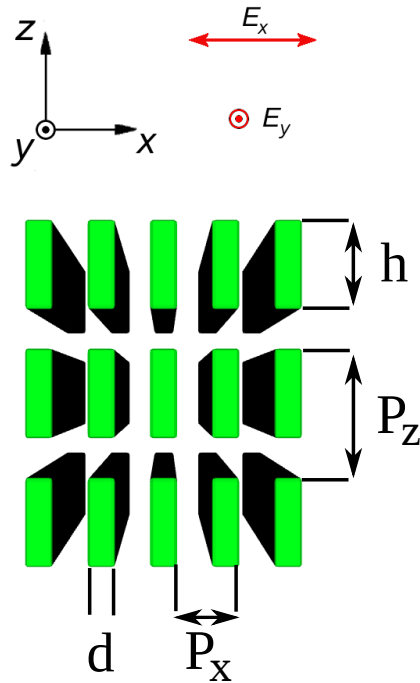


Figure 5.15: The model of multilayer nanoribbons, infinitely long along the Y axis.

and optical response of porous metal film is very close to that of a nonabsorptive dielectric.

Particle shape affects the transmission and can be used to design interesting polarizers with 3D nanoribbon arrays. Metallic nanoribbon arrays are well known for their polarizing properties: the ribbons do not support y-polarized light because they do not polarize in the Y direction. Consequently the y-polarized light is selectively reflected. They were considered previously in a form of a single layer polarizers, but in GLAD multilayer structures are possible [137].

Figure 5.16 shows the transmission for the x and y polarized light passing through four layers of nanoribbons made of nonabsorptive metal. The model of this geometry is given on Figure 5.15. Ribbons are stretching along the Y axis, have height $h = 70$ nm, width $d = 20$ nm, and pitch $P_x = 120$ nm and $P_z = 300$ nm. High transmission of the x-polarized light is contrasting to a total reflection the the y-polarized one, which is expected. However, when more than one layer of nanoribbons is present, narrow peaks of resonance transmission appear in y-polarization, surrounded by a wide bands of reflected frequencies. Peaks are

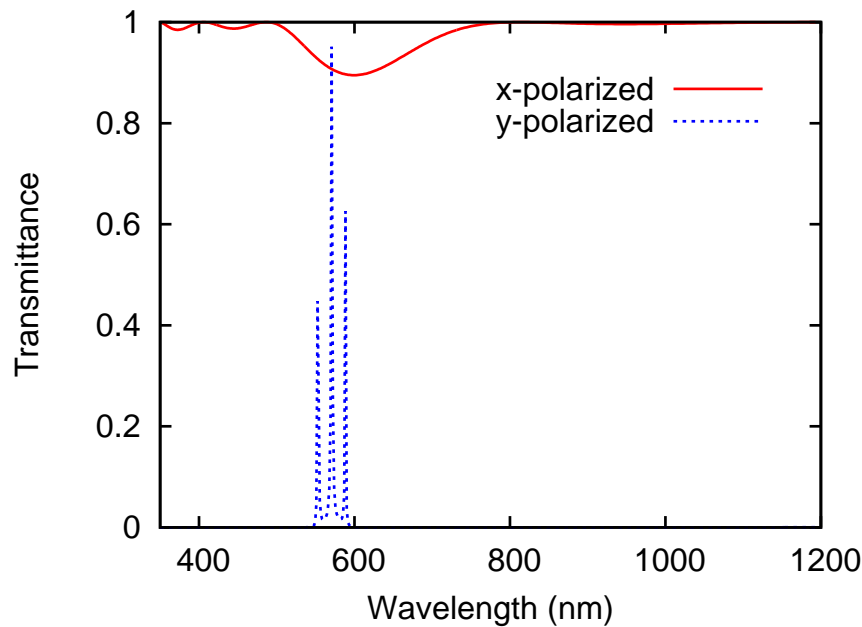


Figure 5.16: FDTD calculated transmission through four layers of nonabsorptive metallic ribbon arrays suspended in air (vertical pitch is $P = 300$ nm, horizontal pitch $P_x = 120$ nm, ribbon width 20 nm and height 70 nm).

closely spaced, and their number is equal to $(N - 1)$. In the current example three peaks are present because the film has four layers of metal.

The resonance in nanoribbon arrays is linked with a strong absorption. While the ribbon width remains small the peak transmittance in the resonances is high – provided the material is nonabsorptive. When the ribbon width increases, as we can see from Figure 5.17, the resonant y-polarized transmittance decreases, and eventually becomes undetectable. The distance between the resonant modes also decreases with the increasing d . Absorptive metals, such as silver, will strongly absorb light within the resonance peaks, therefore they can be exploited only in the far infrared, where they are nearly nonabsorptive. In the visible range, such ribbon arrays can be used as narrow band resonant absorbers.

The x-polarized transmission through the metal ribbons is high when the ribbons are thin in the x-direction, but the band gap forms as the ribbon width increases. Figure 5.18 shows the x-polarized transmission for ribbon widths $d = 20$, 40 nm and $d = 100$ nm. At large ribbon widths the band gap extends over the most

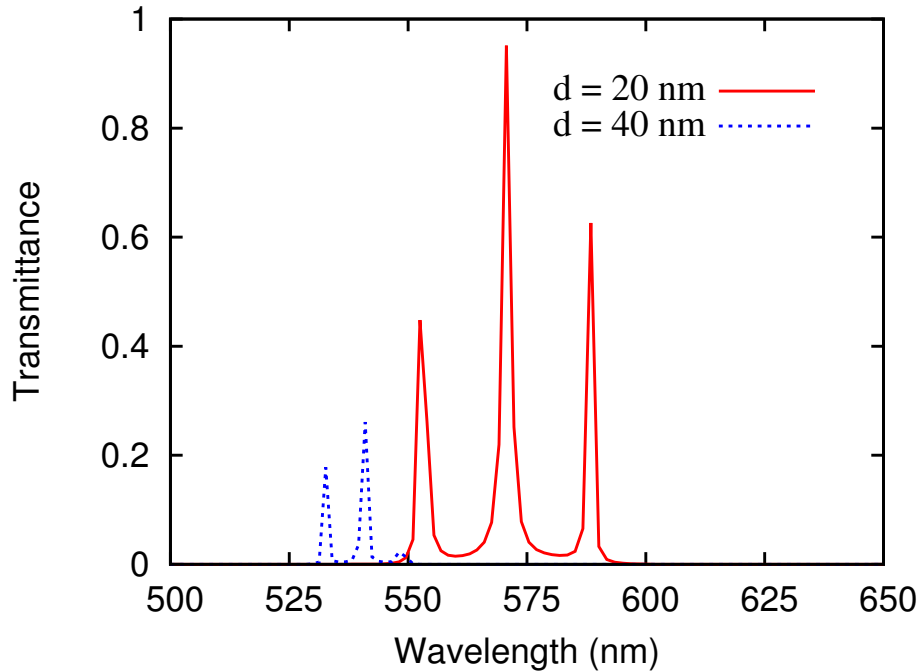


Figure 5.17: Y-polarized transmittance through four layers of nonabsorptive metallic ribbons of various width d .

of the spectrum, leaving only narrow bands of transmitted light. The y-polarized light at these geometries is completely reflected, and the resonant transmission lines are vanishingly small. Consequently with the large ribbon widths the structure acts as a narrow pass filter, exhibiting $(N - 1)$ transmission lines in x-polarization.

In a more realistic case, when the particles are supported by a dielectric vertical post column, the band gap positions redshift due to the increased optical thickness, but do not change qualitatively as shown on a Figure 5.19(a). Also, in practice, metals absorb visible light and the particles can deviate from the idealized cylindrical (or ribbon-like) shape. In GLAD columns, it is also possible that the particles can have a shape of a semispherical “cap”, because they are deposited on the column tops. Figure 5.19(b) shows the transmission spectra for semispherical inclusions in a titania vertical post film ($n_{TiO_2} = 2.4$), with the intercolumnar distance $a = 120$ nm, vertical pitch $P = 500$ nm and column radius $r = 50$ nm. At long wavelengths, the spectrum is relatively similar to that of cylindrical inclusions, but at short wavelengths, the band gaps for curved particles become irregularly

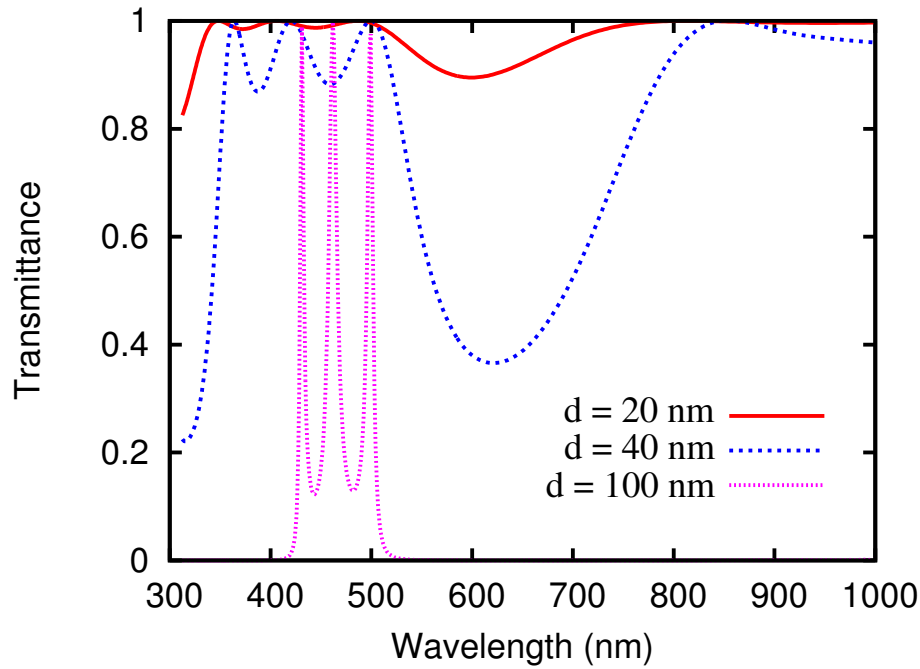


Figure 5.18: X-polarized transmittance through four layers of nonabsorptive metallic ribbons of various width d .

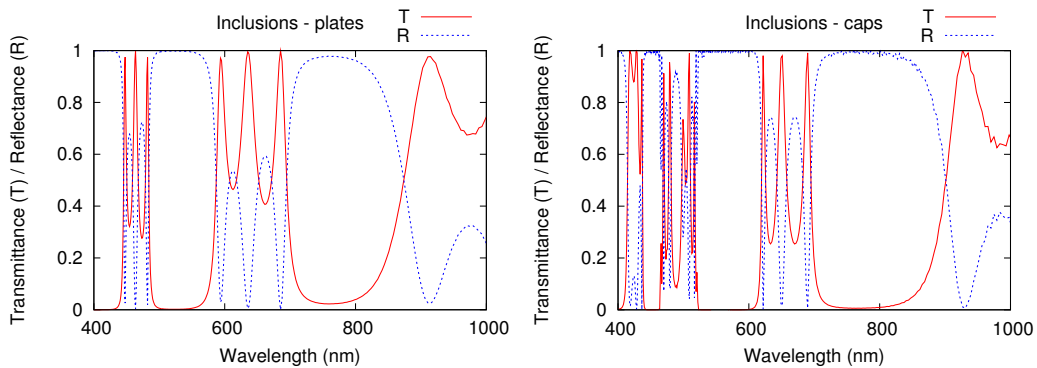


Figure 5.19: Transmittance through four layers of nonabsorptive metallic cylinders (left) and hemispherical caps (right) supported by TiO_2 columns.

spaced and transmission bands do not coincide with those of the cylindrical particles. The changes in the transmission spectrum can be associated with excitation of the surface modes on the curved particles, which are absent on the planar discs. At long wavelengths, particles polarize as a whole in the external field, and their

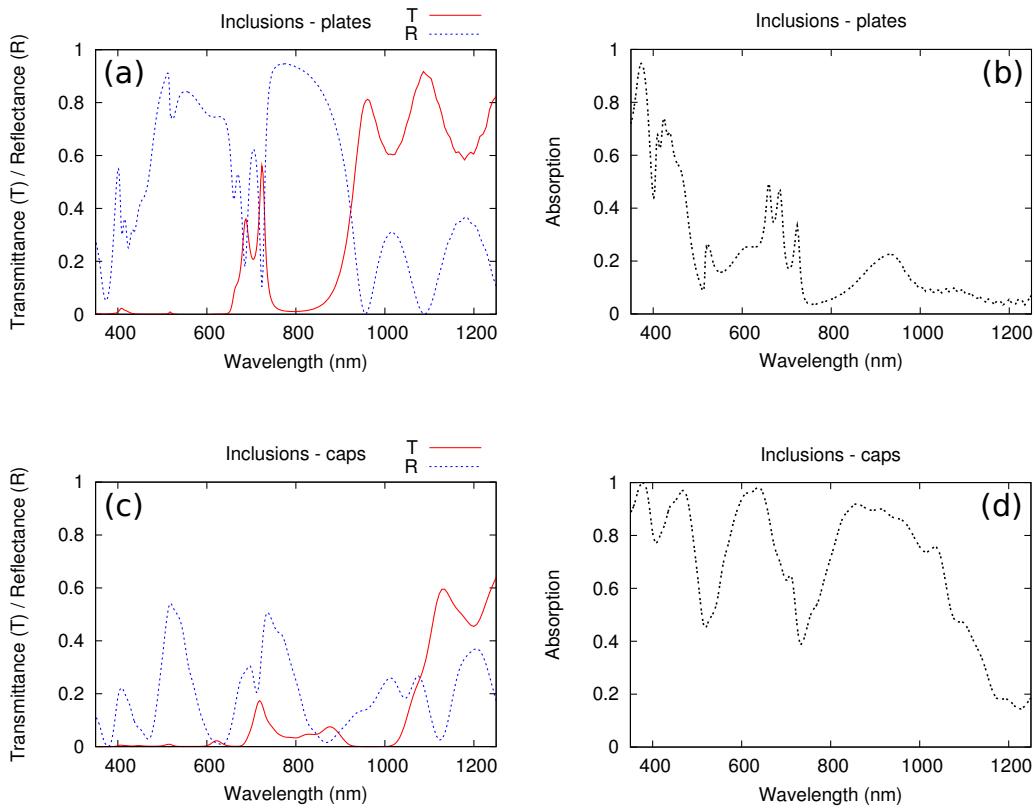


Figure 5.20: Transmittance through four layers of silver cylinders (left) and hemispherical caps (right) supported by TiO_2 columns.

shape is less significant, but at short wavelengths shape becomes important. The band gaps tend to be even slightly stronger when particles are curved, and the pass bands are slightly narrower than for cylindrical particles.

With idealized nonabsorbing metal the plasma wavelength is much shorter than any wavelength considered in simulation ($\lambda_p = 40$ nm in our model), therefore, the role of surface modes is not significant. This model is representative of noble metals at low frequencies of the infrared spectral range. In the visible, the plasma wavelength of many metals is still shorter than the shortest visible wavelength ($\lambda_p = 138$ nm for silver), but absorption is already strong. Figure 5.20 shows the transmission, reflection and absorption in titania vertical posts with four layers of 50 nm thick silver inclusions – the same geometry as presented on Figure 5.19. Absorption was defined as a difference between the incident flux and sum of the

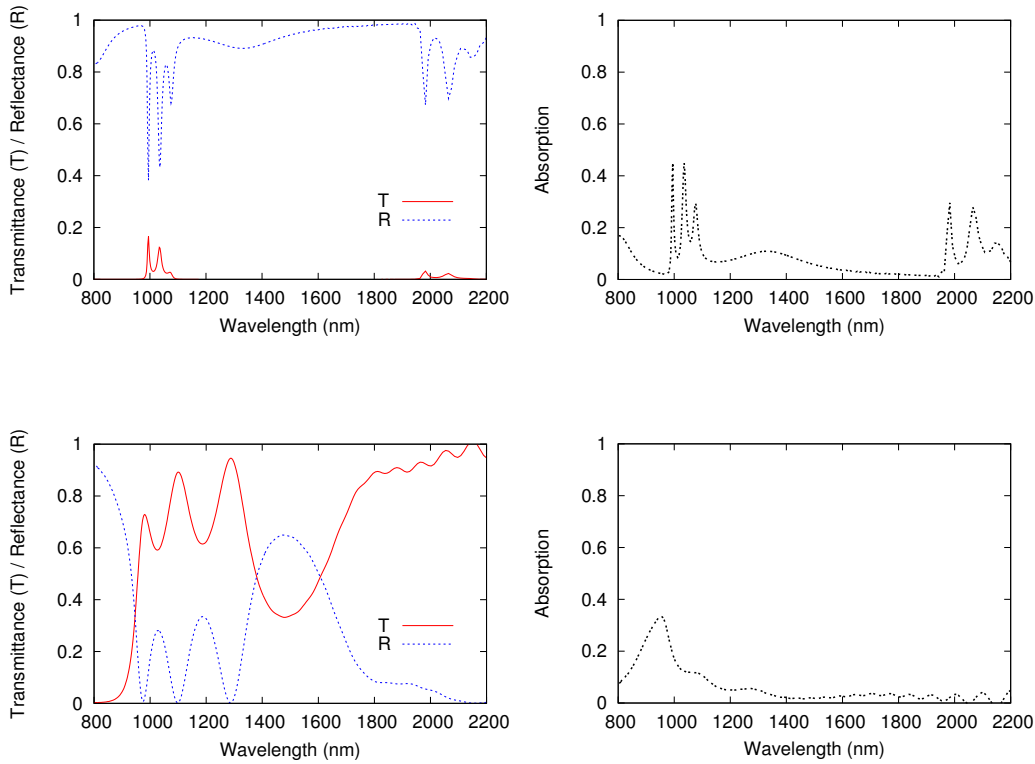


Figure 5.21: Transmission and absorption spectra for TiO_2 columns with four layers of silver inclusions at material to void ratio $f = 78.5\%$ (above) and $f = 54.5\%$ (below).

transmitted and reflected fluxes: $A = 1 - T - R$. The band gap at 800 nm is smaller than for the nonabsorbing metal, and the transmission is suppressed by absorption at wavelengths below 600 nm. The transmission band at 700 nm is still divided in separate resonant peaks if particles are cylindrical, but these peaks are washed out when particles are curved. The most significant difference between planar and curved particles is in the absorption rate. In the film with planar cylindrical particles, the absorption gradually increases with the decreasing wavelength, showing local maxima at transmission bands, and minima in the band gaps. The curved inclusions, however, have a different absorption spectrum with a series of peaks and valleys, extending into the infrared. This increased infrared absorption indicates a stronger light coupling to the surface plasmon modes, compared to the planar inclusions.

The unwanted absorption in silver arrays is less prominent at the near infrared.

Figure 5.21 shows the near infrared spectra for the same model as above for two different in-substrate lattice constants: $a = 100$ nm; and $a = 120$ nm. At $a = 100$ nm columns are touching each other, filling most of the space. Clearly at infrared wavelengths the absorption inside the band gap is much lower than in the visible, while absorption in the resonant transmission peaks remains relatively high. Also we can see that the band gap width depends inversely on the inter-particle distance.

The vertical post films with layers of metal are among the easiest to fabricate, and rotational symmetry is readily transferred to the metal islands. Already in the case of metallic ribbons the fabrication results may not be consistent with predictions, because randomly positioned slanted posts do not form infinite ribbons, but irregularly spaced short ribbons. With these considerations GLAD columnar resonators were fabricated in the vertical post architecture, as will be described in the following section.

5.4.2 The experiment and transmission loss in granular metals

Vertical post films were fabricated by Douglas Gish in the Microfabrication facility of the university of Alberta. The film was numerically designed to have a resonant transmission/absorption line in the telecommunication range, close to $\lambda \sim 1400$ nm. The column radius was 100 nm, lattice constant of a square array $a = 240$ nm, and $h = 100$ nm thick metal cylinders were included in each column at a constant vertical interval $1 \mu\text{m}$.

The deposition was started with titanium dioxide and after reaching 1000 nm film depth, the deposition system was vented and the film was optically characterized. The metal film was deposited on the top, then the film was removed from deposition system, and transmittances were measured again. Then the process of dielectric deposition was repeated. Three layers of metal were deposited in total, and SEM image of the structure is shown beside the measured transmission spectrum on Figure 5.22.

Theoretical spectra were calculated for the film with geometry defined from SEM image and they are shown on a Figure 5.23. The filling fraction of the structure is $f = 35.2\%$, average distance between metal layers $P = 1065$ nm, average column diameter $D = 226$ nm, and intercolumnar distance $a = 315$ nm, as pro-

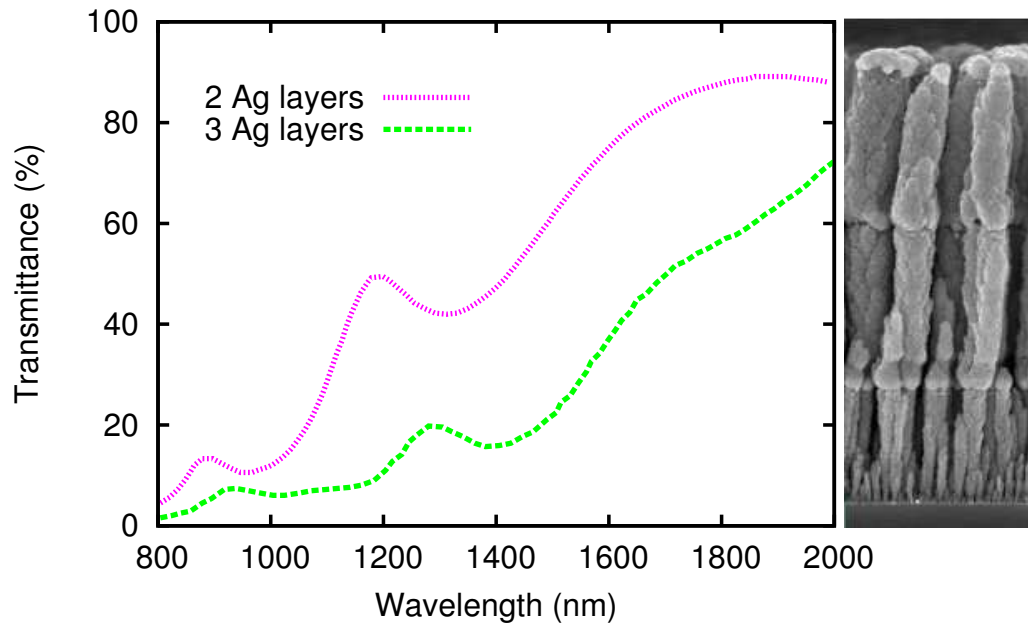


Figure 5.22: Experimentally measured transmission spectrum for the film with two and three layers of silver.

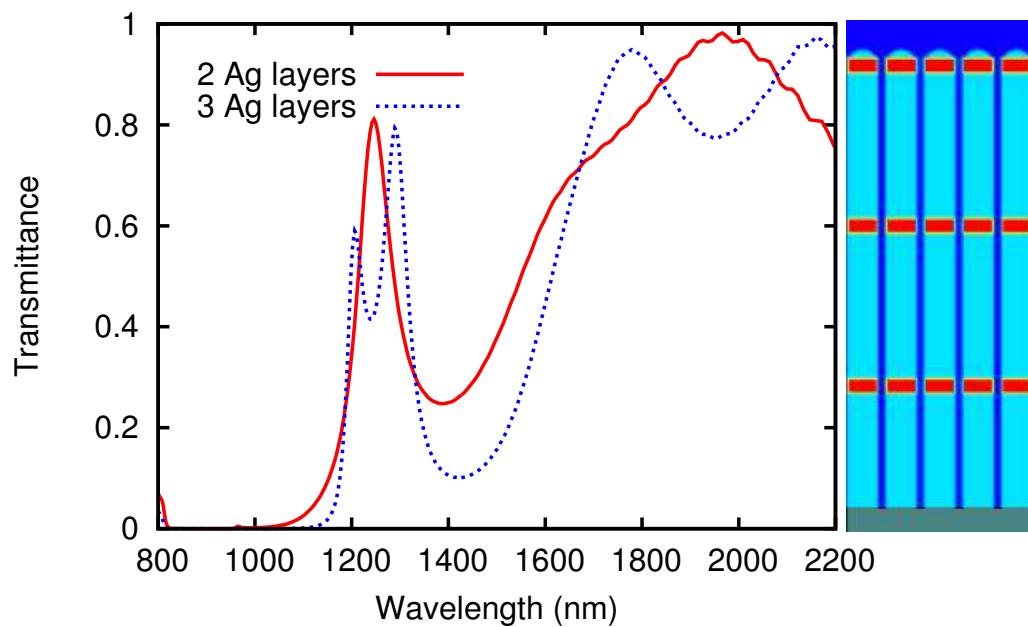


Figure 5.23: Simulated transmission through the experimentally fabricated film (geometry defined from SEM data).

jected on a square lattice. From SEM the thickness of metal layers is approximately 115 nm. The peak positions are in a relatively good agreement between theory and experiment, but the experimentally measured peak transmittances are much lower than simulated. Also, the film with three layers of porous metal does not show the predicted splitting in the resonance peak.

The transmission loss in the fabricated columns can be expected from the granular structure of the PVD deposited metal films. It was previously shown that electrochemically deposited gold nanorods have a granular nanocrystalline structure, which limits the electron mean free path and reduces the plasmon assisted transmission [6]. The same effect can be expected in the GLAD deposited metal films.

Assuming that the metal nanoparticles have a nanocrystalline structure with the domain size R the dielectric function of metal can be written as [14]:

$$\epsilon_g = \epsilon_m + \frac{j\gamma(L - R)}{\omega R - jL\gamma} \epsilon_D \quad (5.14)$$

where

$$\begin{aligned} \epsilon_m &= 1 + \epsilon_D + \epsilon_B \\ \epsilon_D &= -\frac{\omega_p^2 f}{\omega(\omega - j\gamma)} \\ \epsilon_B &= \sum_{i=1}^k \frac{f_i \omega_p^2}{(\omega_i^2 - \omega^2) + j\omega\gamma_i} \\ L &= \sqrt{\frac{2E_F}{m_e \gamma^2}} \end{aligned}$$

ϵ_g is a dielectric function of granular metal with bulk dielectric function ϵ_m ; γ and L are the relaxation frequency and mean free path of free electrons in the bulk metal; R is the nanocrystalline domain radius; ϵ_D is free electron contribution into the bulk metal dielectric function, where f is an effective fraction of free electrons in bulk metal; ϵ_B is a contribution of bound electrons, where k is a number of Lorentzian relaxations of bound electrons with frequency ω_i , strength f_i , and relaxation frequencies γ_i . Mean free path L is determined by the energy of Fermi level in a given metal E_F , electron mass m_e and relaxation frequency γ . With the Fermi energy levels $E_F = 5.49$ eV [5] and relaxation frequency $\gamma = 0.048$ eV

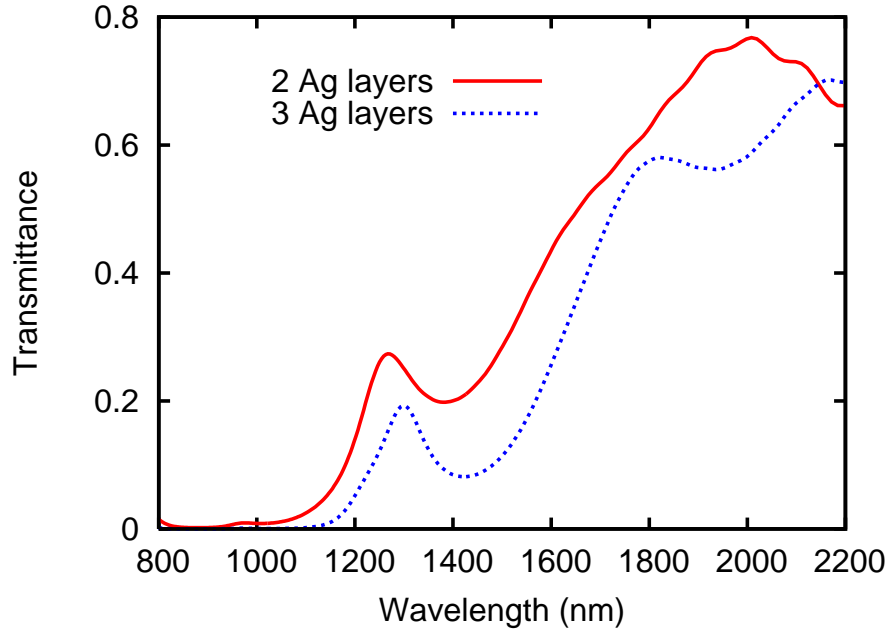


Figure 5.24: Simulated transmission through the experimentally fabricated film, taking into account granular crystalline structure of metal particles.

[99] bulk silver would have electron mean free path $L = 39$ nm.

In FDTD, this dielectric function has to be approximated with a Lorentz series, which can be done by fitting (5.14) with a new Lorentz approximation. The expressions can also be simplified for $R \ll L$. The relaxation frequency of free electrons in noble metals is much smaller than frequency of light in the visible and infrared spectrum, therefore in the limit $\gamma \rightarrow 0$ and $R \ll L$ the formula simplifies to:

$$\epsilon_g = 1 + \tilde{\epsilon}_D + \epsilon_B, \quad (5.15)$$

where

$$\tilde{\epsilon}_D = -\frac{\omega_p^2 f}{\omega(\omega - j\gamma')},$$

$$\gamma' = \gamma \frac{L}{R}.$$

The dielectric function (5.15) has been previously successfully used to describe the optical properties of golden nanorod arrays [6], and the grain size determined there was ~ 3 nm, much smaller than the mean free path ($L = 36$ nm for gold).

X-ray diffraction and transmission electron microscopy of uniform metal films give a larger (often much larger) values of mean grain diameters [150, 67], but as the grain diameters decrease with both film thickness and temperature [67], it will not be surprising to see small grains in the films that are composed of small metal particles, deposited at low temperatures.

Figure 5.24 shows the FDTD simulated transmittance for the film with the same geometry as in the experiment (figures 5.22 and 5.23) and nanocrystalline metal particles with domain radius $R = 2.5$ nm.

The simulated transmittance is now in much better agreement with the measured one, and the resonant peak does not split when three metal layers are used. The absence of resonant peak splitting is caused by increased loss: while resonance between the adjacent metal planes is strong enough to cause a small resonance peak, the long range interaction between layers that are not immediate neighbours is too weak. The resonant transmittance can potentially be improved by annealing the film, as it usually increases the size of nanocrystalline domains [6, 67, 150].

Granular structure of the metal particles can express itself in the other GLAD films composed of metals or containing metals as inclusions. The effects of metal nanocrystallinity gradually diminish at long wavelengths, but at the visible and near infrared, they have to be considered.

5.5 Chapter summary

Effective dielectric response of metal composites creates various possibilities for optical engineering even with a simple vertical post structure. The resonant absorption on metal particles, as well as their magnetic response near the Mie resonance, are well known and studied using both analytical and numerical methods. Here it has been shown that arranging these particles in 3D composites leads to spectral properties, that are usually not found in 2D structured metallic films. Metallic columns can be considered as metamaterials, with a relatively stable dielectric response over a wide infrared spectrum, and feature scales much smaller than wavelength. Each column responds to light as a large-scale atom, with its electronic properties determined by the geometry rather than by quantum-mechanical properties of atomic orbitals. The properties of these “atoms” can be tailored, rather than selected from a limited set of naturally existing species. As we have

seen, they can often be described by effective medium theory, and the same results can be expected from the Mie theory [152], as it is used in the derivation of effective medium approximations [93, 87]. Numerical models further predict the magnetic properties, and facilitate material design. Here we have shown how the magnetic and dielectric properties can be altered in simple columnar nanostructures, and supported our observations with analytical approximations. The magnetic response decreases with the decreasing scale of the structures, therefore many interesting phenomena, such as negative refraction, will fall close to the band gaps where scattering is strong. The complexity of the column can be further increased either to produce negative index materials, or materials with high absorption, or high index materials.

Interesting electromagnetic phenomena arise also due to long range interactions between ordered metal particles, if they are inserted as periodic layers in GLAD columnar films. Multiple layers of metallic strips have a prominent polarization selectivity, with wide band gaps in both polarizations and a number of resonant transmission peaks in one or another polarization, depending on the strip width and volume filling. Multiple resonant absorption (transmission) lines are also observed in rotationally symmetric vertical posts with metallic inclusions. One such vertical post structure, consisting of periodic layers of porous silver, sandwiched between layers of columnar TiO_2 , was fabricated and measured data were compared to simulations.

Chapter 6

Conclusions

6.1 Summary of findings

In this thesis, GLAD films were considered from three different perspectives: (i) as anisotropic index graded interference mirrors; (ii) as photonic crystals; and (iii) as metamaterials. Most of the applications, discussed here, were based on the band gap properties of periodic column arrays. When densely packed, columns were treated as effectively uniform anisotropic films, and their refractive index was determined from FDFD-calculated dispersion relations. Tilted GLAD columns are usually bianisotropic meaning that all three principle refractive indices are different in the film, and two optical axes can be introduced. This property was used to design birefringent thin film polarizers.

The polarizers were designed on the basis of s-shaped TiO_2 columns and simulated transmittances were compared to the transmittances of fabricated films. The column tilt was periodically varied in vertical plane, so that columns had mirror symmetry relative to this plane. Due to mirror symmetry, the band gap widths and positions were different for two orthogonal linear polarizations. Two forms of the anisotropy variation exist in these films: one is provided by an s-shaped column profile, and the other one by the column cross-section broadening in the substrate plane. Two sources of the anisotropy variation are competitive in their influence on the x-polarized band gap (x-polarized light had an electric vector oscillating in the mirror plane of s-shaped columns), and at a certain combination of tilt angle and cross-section elongation, the x-polarized band gap was completely

suppressed. This created a narrow band polarizer, transmitting the x-polarized light and reflecting the y-polarized one within the y-polarized band gap. The column geometry with the suppressed x-polarized band gap forms naturally due to the lack of shadowing in the Y direction, as was observed in the experiment.

Polarizing properties can be actively switched if the film is infiltrated with a liquid crystal, which makes its optical properties sensitive to the applied external field. Liquid crystals reduce the refractive index contrast and the band gap becomes considerably smaller than in the air-filled film. The porous nature of s-shaped polarizers, however, can be exploited not only with liquid crystals. We can expect that ambient changes, for example in humidity, will also affect the polarizing state of the film, which can be used for detection and measuring purposes. Band gap shift in response to the ambient conditions has been previously used for humidity sensing [40]. The spectral change has been detected either by spectroscopic measurements, when the defect mode was used, or by eye, when the gap shift was substantial enough to change the film's colour. With the polarizer, detection can be performed by measuring the polarization state of the transmitted light.

In Chapter 3, vertical post columns were considered that lacked polarization selectivity due to their rotational symmetry, but had high anisotropy. In the anisotropic films, where the extraordinary index is aligned normally to the film's surface and higher than the ordinary index, the band gap position becomes less dependent on the incidence angle than in the isotropic films. This was used here to create interference mirrors with omnidirectional reflection bands in the visible spectral range, based on TiO_2 columnar films. Three refractive index profiles were considered: (i) distributed Bragg reflectors, known to have the widest band gaps at normal incidence; (ii) sinusoidal - a classic index profile used in rugate interference filters; and (iii) Gaussian - the index profile that was recently claimed as a source of wide omnidirectional band gaps [4]. Anisotropic films have omnidirectional reflection bands up to four times wider than their isotropic analogs. Simulations performed in this thesis did not confirm the extraordinary properties of Gaussian index graded films, which had an omnidirectional reflection band comparable to that of sinusoidal profiles, and smaller than in the DBR profiles (in the works introducing Gaussian omnidirectional mirrors it was claimed that they perform better than DBR). It was further shown in this thesis that the refractive index contrast

has to be optimized to achieve the widest omnidirectional reflection, and with optimized index contrast the maximum omnidirectional band widths are 14.5% for DBR TiO₂ columns, 12% for Gaussian and 10.5% for sinusoidal profiles.

A different application of GLAD columnar films was studied in Chapter 4. Square spirals were considered as 3D photonic crystals with the band gaps in the visible spectral band. While the original design of square spiral photonic crystals by Toader et al. [123] indicated that the 3D band gap is possible with column refractive indices as low as $n_{col} \approx 2.2$, simulations carried in this thesis have shown that the column cross-section shape prevents the 3D band gap from forming in currently fabricated GLAD square spirals. Both simulations and the experiment have shown the presence of pseudogap, but not a three-dimensional band gap. The overlap between 4th and 5th bands is currently as large as 18%, as was shown in theoretical analysis of the fabricated film. When the column geometry was optimized, TiO₂ spirals with a circular cross-section showed a smaller overlap of 12%. The 3D band gap forms only when the in-substrate column cross-sections are elongated parallel to the column tilt plane. The cross-section broadening has to be as large as $w_{||}/w_{\perp} > 2.03$, which cannot be achieved with currently existing substrate motion algorithms.

Much smaller cross-section anisotropy ($w_{||}/w_{\perp} > 1.21$) is required in the inverted square spirals. Such an architecture was realized previously with silicon dioxide, and with templating techniques it may be fabricated in the future based on the titanium dioxide. The 3D band gap is also improved by material redistribution, increasing when the material concentrates around the nodes of square spiral. This assumes a periodic change in the film density during its vertical development. It may require a variable deposition angle and possibly cause non-optimal shadowing during column growth. Therefore, in practice, material redistribution in square spirals needs substantial experimental development.

Chapter 5 addressed the GLAD films as metamaterials carrying ordered arrays of metal nanoparticles. It was shown here that periodic layers of porous metal create a series of wide band gaps, and the effective refractive index of these layers can be described by a real positive dielectric constant of high value. The value of their effective permeability may significantly exceed the permeabilities of naturally occurring materials and weakly depend on wavelength. If metal particles in these layers are elongated they may exhibit interesting polarizing properties. The light

passing through long metal strips is usually not transmitted, if polarized parallel to them, but due to the capacitive coupling between multiple layers of strips, resonant transmission occurs. By changing the width of metallic strips and separation between them the geometry can be adjusted so that one polarization is transmitted and the other one reflected, except for a number of closely spaced transmission lines. These effects provide an opportunity for the various polarizer designs.

If the distance between metal particles is much smaller than the wavelength then, like dielectrics, they transmit light as effective media. Metallic vertical posts, studied here, have a response of an artificial material with a resonant absorption band located at frequency smaller than the plasma frequency for the metal they are made of. They have a nearly constant refractive index in a broad infrared spectral range, and a resonant peak typically in the mid visible band. Metallic vertical posts also have a noticeable magnetic response, with the magnetic permittivities smaller than unity. This magnetic response decreases ($\mu \rightarrow 1$) as the columns are scaled down. Larger magnetic response can be also expected in other nanoparticle geometries, such as helices, where better defined magnetic loops can be formed by induced currents, and these architectures should be considered in future research.

6.2 Challenges and future research

6.2.1 Scattering in GLAD films

A number of areas in GLAD research are yet not studied and can be addressed with numerical simulations. Scattering, for example, has been poorly studied due to its complex statistical nature. Scattering was encountered in this work in square spirals, where it reduced specular reflectivity at short wavelengths. The decline of reflectivity with wavelength suggested that the dominant process was the Rayleigh scattering on the irregularities in column density, and column surface roughness. It was taken into account in the form of an artificial extinction coefficient, which showed the loss in the intensity of specularly reflected light.

Scattering extinction depends on the root mean square fluctuation of the dielectric function, and on the correlation length of its fluctuation. If these statistical values can be derived from the column morphology, scattering strength can be calculated analytically for the densely packed anisotropic GLAD films. On Fig-

ure 2.11 of Chapter 2, the measured transmission declines at wavelengths where TiO_2 absorption is small, suggesting that taking scattering into account may be a valuable addition to the optical simulation of s-shaped columnar films. Studies of column morphology have already been done for vertical posts in a work of K. Krause et al. [69].

Scattering on GLAD films can be useful where light has to be deflected, or coupled to a waveguide. Since GLAD films have large flexibility in their column geometry, it may be possible to use them for designing such scatterers. Theoretically the angular distribution of the transmitted light can be calculated by a far field transform, following from the equivalence principle [127]. The challenge of such a study is in the statistical nature of the column spatial distribution, which cannot be directly accounted for in the numerical simulation. Simulations for large arrays of randomly standing columns currently require large computational resources, especially memory. Therefore theoretical formalism is needed which will take into account the random distribution of GLAD columns but limit the simulated domain to as few columns as possible.

6.2.2 Multiscale and multiphysical simulations

Many practical applications, such as solar cells and lasers, involve current transport, light emission, and heat transfer besides the transmission and absorption of light. To completely describe these systems a number of physical processes often have to be simulated simultaneously. Therefore the electromagnetic propagation problem has to be coupled with a number of others, describing the electron transport and possibly a spatial charge distribution. The electromagnetic simulation proved to be very efficient as applied to GLAD films therefore it looks promising to extend these simulations to multiphysical problems. Many examples of software that address such multiphysics problems already exist, such as the well known ANSYS software.

6.2.3 Nonlinear processes

Nonlinear materials were not considered in this thesis, because historically they are not often used in GLAD films. However, it is interesting to look at light emission and nonlinear conversion in defect layers of GLAD mirrors, especially

as they were proven here to have relatively wide omnidirectional reflection bands. Large enhancement of second harmonic generation has been previously reported for band gap materials [100, 124] and photonic crystals were also used to produce single mode lasers, emitting the frequency of the photonic crystal resonant mode, and on the edge of photonic band gap. Therefore, in the future it will be interesting to study gain and nonlinear materials both in isotropic and in anisotropic omnidirectionally reflecting films, and compare these architectures. Nonlinear and gain materials can be simulated with FDTD if nonlinear susceptibilities are added to the dielectric response of studied materials [119]. FDTD allows one to include nonlinear susceptibilities without additional assumptions, and therefore it is applicable to structures of any geometric complexity. It has also been shown to remain stable for hundreds of thousands of timesteps, describing nonlinear materials as accurately as nondispersive dielectrics [59].

Bibliography

- [1] J. P. Albert, C. Jouanin, D. Cassagne, and D. Bertho. Generalized wannier function method for photonic crystals. *Phys. Rev. B*, 61:4381–4384, Feb 2000.
- [2] J. Anderson, M. Okoniewski, and S. Stuchly. Practical 3-d contour/staircase treatment of metals in fddd. *Microwave and Guided Wave Letters, IEEE*, 6(3):146–148, mar 1996.
- [3] D. Ariza-Flores, L. M. Gaggero-Sager, and V. Agarwal. Omnidirectional photonic bandgap in dielectric mirrors: a comparative study. *J. Phys. D: Appl. Phys.*, 45(015102), 2012.
- [4] J. Arriaga and X. I. Saldana. Band structure and reflectivity of omnidirectional si-based mirrors with a gaussian profile refractive index. *J. Appl. Phys.*, 100(044911), 2006.
- [5] N. W. Ashcroft and N. D. Mermin. *Solid State Physics*. Saunders, 1976.
- [6] R. Atkinson, W. R. Hendren, G. A. Wurtz, W. Dickson, A. V. Zayats, P. Evans, and R. J. Pollard. Anisotropic optical properties of arrays of gold nanorods embedded in alumina. *Phys. Rev. B*, 73:235402, Jun 2006.
- [7] K. Aydin. Broadband polarization-independent resonant light absorption using ultrathin plasmonic super absorbers. *Nat Commun*, 2, 2011.
- [8] E. W. Baumgartner, T. Schwarzl, G. Springholz, and W. Heiss. Highly efficient epitaxial bragg mirrors with broad omnidirectional reflectance bands in the midinfrared. *Applied Physics Letters*, 89(051110), 2006.

- [9] R. Bilyalov, L. Stalmans, G. Beaucarne, R. Loo, M. Caymax, J. Poortmans, and J. Nijs. Porous silicon as an intermediate layer for thin-film solar cell. *Solar Energy Materials and Solar Cells*, 65(14):477 – 485, 2001. [jce:titlejPVSEC 11 Part Ij/ce:titlej](#).
- [10] M. Born and E. Wolf. *Principles of optics: Electromagnetic theory of propagation, Interference and Diffraction of light*. Pergamon Press, 4 edition, 1968.
- [11] M. J. Brett, A. L. Elias, and K. D. Harris. Fabrication of Helically Perforated Gold, Nickel, and Polystyrene Thin Films. *Journal of Microelectromechanical Systems*, 13(5):808–813, Oct. 2004.
- [12] D. Bruggeman. pages 636–664, 1935.
- [13] H. U. Camron, R. M. Pilliar, and I. Macnab. The rate of bone ingrowth into porous metal. *Journal of Biomedical Materials Research*, 10(2):295–302, 1976.
- [14] R. Carey and B. W. J. Thomas. Magneto-optic size effects in granular films. *Journal of Physics D: Applied Physics*, 8:336–341, 1975.
- [15] G. A. Chapman. An interference filter for observing the photospheric network. *Solar Physics*, 13:78–84, 1970. [10.1007/BF00963943](#).
- [16] K. M. Chen, A. W. Sparks, H.-C. Luan, D. R. Lim, K. Wada, and L. C. Kimerling. $\text{SiO}_2/\text{TiO}_2$ omnidirectional reflector and microcavity resonator via the sol-gel method. *Applied Physics Letters*, 75(24):3805–3807, 1999.
- [17] M. Chevalier, R. Luebbers, and V. Cable. Fdtd local grid with material traverse. *Antennas and Propagation, IEEE Transactions on*, 45(3):411–421, 1997.
- [18] F. Chiadini and A. Lakhtakia. Extension of hodgkinson’s model for optical characterization of columnar thin films. *Microwave and Optical Technology Letters*, 42(1):72–73, 2004.

- [19] D. N. Chigrin, A. D. Lavrinenko, D. A. Yarotsky, and S. V. Gaponenko. All-dielectric one-dimensional periodic structures for total omnidirectional reflection and partial spontaneous emission control. *J. Lightwave Technol*, 17:2018–2024, 1999.
- [20] D. N. Chigrin, A. D. Lavrinenko, D. A. Yarotsky, and S. V. Gaponenko. Observation of total omnidirectional reflection from a one-dimensional dielectric lattice. *Appl. Phys. A*, 68:25–28, 1999.
- [21] D. N. Chigrin and C. M. Sotomayor Torres. Periodic thin-film interference filters as one-dimensional photonic crystals. *Optics and Spectroscopy*, 91(3):484–489, 2001.
- [22] J. Chilwell and I. Hodgkinson. Thin-films field-transfer matrix theory of planar multilayer waveguides and reflection from prism-loaded waveguides. *Journal of the optical society of America A*, 1(7):742–753, July 1984.
- [23] S. Y. Chou. Sub-10 nm imprint lithography and applications. *Journal of Vacuum Science & Technology B: Microelectronics and Nanometer Structures*, 15(6):2897, Nov. 1997.
- [24] J. A. Dobrowolski and A. Waldorf. High-performance thin film polarizer for the uv and visible spectral regions. *Applied Optics*, 20(1):111–116, 1981.
- [25] J. W. Eaton, D. Bateman, and S. Hauberg. *GNU Octave Manual Version 3*. Network Theory Limited, 2008.
- [26] J. O. Estevez, J. O. Arriaga, A. Mendez Blas, and V. Agarwal. Omnidirectional photonic bandgaps in porous silicon based mirrors with a gaussian profile refractive index. *Applied Physics Letters*, 93(191915), 2008.
- [27] J. O. Estevez, J. O. Arriaga, A. Mendez Blas, and V. Agarwal. Enlargement of omnidirectional photonic bandgap in porous silicon dielectric mirrors with a gaussian profile refractive index. *Applied Physics Letters*, 94(061914), 2009.
- [28] Y. Fink, J. N. Winn, S. Fan, C. Chen, J. Michel, J. D. Joannopoulos, and E. L. Thomas. A dielectric omnidirectional reflector. *Science*, 282:1679, 1998.

- [29] U. Gangopadhyay, S. Dhungel, P. Basu, S. Dutta, H. Saha, and J. Yi. Comparative study of different approaches of multicrystalline silicon texturing for solar cell fabrication. *Solar Energy Materials and Solar Cells*, 91(4):285 – 289, 2007.
- [30] J. K. Gansel, M. Thiel, M. S. Rill, M. Decker, K. Bade, V. Saile, G. von Freymann, S. Linden, and M. Wegener. Gold helix photonic metamaterial as broadband circular polarizer. *Science*, 325:1513–1515, 2009.
- [31] N. Garcia, E. V. Ponizovskaya, H. Zhu, J. Q. Xiao, and A. Pons. Wide photonic band gaps at the visible in metallic nanowire arrays embedded in a dielectric matrix. *Applied Physics Letters*, 82(19):3147 –3149, may 2003.
- [32] D. S. Ginley and J. D. Perkins. Transparent conductors. In D. S. Ginley, editor, *Handbook of Transparent Conductors*, pages 1–25. Springer US, 2010.
- [33] D. Gish, M. Summers, and M. Brett. Morphology of periodic nanostructures for photonic crystals grown by glancing angle deposition. *Photonics and Nanostructures - Fundamentals and Applications*, 4(1):23–29, Feb. 2006.
- [34] J. I. Gittleman and B. Abeles. Comparison of the effective medium and the maxwell-garnett predictions for the dielectric constants of granular metals. *Physical Review B*, 15(6):3273–3275, 1976.
- [35] A. N. Grigorenko, A. K. Geim, H. F. Gleeson, Y. Zhang, A. A. Firsov, I. Y. Khrushchev, and J. Petrovic. Nanofabricated media with negative permeability at visible frequencies. *Nature*, 438(7066):335–338, 2005.
- [36] L. Guo. Nanoimprint Lithography: Methods and Material Requirements. *Advanced Materials*, 19(4):495–513, Feb. 2007.
- [37] M. M. Hawkeye and M. J. Brett. Narrow bandpass optical filters fabricated with one-dimensionally periodic inhomogeneous thin films. *J. Appl. Phys.*, 100(044322), 2006.
- [38] M. M. Hawkeye and M. J. Brett. Glancing angle deposition: Fabrication, properties, and applications of micro- and nanostructured thin films. *J. of Vac. Sci. & Tech. A.*, 25(5):1317–1335, 2007.

- [39] M. M. Hawkeye and M. J. Brett. Controlling the optical properties of nanostructured tio₂ thin films. *Phys. Status Solidi A*, 206(5):940–943, 2009.
- [40] M. M. Hawkeye and M. J. Brett. Optimized colorimetric photonic-crystal humidity sensor fabricated using glancing angle deposition. *Advanced Functional Materials*, 21(19):3652–3658, 2011.
- [41] M. M. Hawkeye, R. J. Joseph, C. Sit, and M. J. Brett. Coupled defects in one-dimensional photonic crystal films fabricated with glancing angle deposition. *Optics Express*, 18(12):13220–13226, 2010.
- [42] Y. He, Z. Zhang, C. Hoffmann, and Y. Zhao. Embedding ag nanoparticles into mgf₂ nanorod arrays. *Advanced Functional Materials*, 18(11):1676–1684, 2008.
- [43] K. Ho, C. Chan, and C. Soukoulis. Existence of a photonic gap in periodic dielectric structures. *Physical Review Letters*, 65(25):3152–3155, Dec. 1990.
- [44] K. M. Ho, C. T. Chan, and C. M. Soukoulis. Existence of a photonic gap in periodic dielectric structures. *Phys. Rev. Lett.*, 65:3152–3155, Dec 1990.
- [45] I. Hodgkinson, Q. hong Wu, and J. Hazel. Empirical equations for the principal refractive indices and column angle of obliquely deposited films of tantalum oxide, titanium oxide, and zirconium oxide. *Appl. Opt.*, 37(13):2653–2659, May 1998.
- [46] I. Hodgkinson and Q. H. Wu. Birefringent thin-film polarizers for use at normal incidence and with planar technologies. *Applied Physics Letters*, 74(13):1794–1796, 1999.
- [47] I. Hodgkinson and Q. H. Wu. Serial bideposition of anisotropic thin films with enhanced linear birefringence. *Applied Optics*, 38(16):3621–3625, 1999.
- [48] I. Hodgkinson, Q. H. Wu, M. Arnold, L. De Silva, G. Beydaghyan, K. Kamin-ska, and K. Robbie. Biaxial thin-film coated-plate polarizing beam splitters. *Applied optics*, 45(7):1563–8, Mar. 2006.
- [49] I. Hodgkinson, Q. H. Wu, L. De Silva, and M. Arnold. Inorganic positive uniaxial films fabricated by serial bideposition. *Optics express*, 12(16):3840–7, Aug. 2004.

- [50] P. C. P. Hrudehy, B. Szeto, and M. J. Brett. Strong circular bragg phenomena in self-ordered porous helical nanorod arrays of alq3. *Applied Physics Letters*, 88(25):251106–251106–3, jun 2006.
- [51] S. Hughes, L. Ramunno, J. F. Young, and J. E. Sipe. Extrinsic optical scattering loss in photonic crystal waveguides: Role of fabrication disorder and photon group velocity. *Physical Review Letters*, 94(033903), 2005.
- [52] M. J. Jackson. Microfabrication using x- ray lithography. In *Micro and Nanomanufacturing*, pages 55–98. Springer US.
- [53] Y.-J. Jen, C.-H. Chen, and C.-W. Yu. Deposited metamaterial thin film with negative refractive index and permeability in the visible regime. *Opt. Lett.*, 36(6):1014–1016, Mar 2011.
- [54] M. Jensen and M. Brett. Periodically Structured Glancing Angle Deposition Thin Films. *IEEE Transactions On Nanotechnology*, 4(2):269–277, Mar. 2005.
- [55] M. O. Jensen and M. J. Brett. Porosity engineering in glancing angle deposition thin films. *Appl. Phys. A.*, 80(4):763–768, 2005.
- [56] M. O. Jensen and M. J. Brett. Square spiral 3D photonic bandgap crystals at telecommunications frequencies. *Optics Express*, 13(9):3348, 2005.
- [57] L. Jiang, G. Zheng, L. Shi, and X. Li. Broad omnidirectional reflector design for optical telecommunications band using genetic algorithm. *Japanese Journal of Applied Physics*, 47(8):6333–6336, 2008.
- [58] S. G. Johnson and J. D. Joannopoulos. Block-iterative frequency-domain methods for maxwell’s equations in a planewave basis. *Optics Express*, 8(3):173–190, 2001.
- [59] R. Joseph and A. Taflove. Fdtd maxwell’s equations models for nonlinear electrodynamics and optics. *Antennas and Propagation, IEEE Transactions on*, 45(3):364–374, 1997.
- [60] K. Kalantar-zadeh and B. Fry. Nano fabrication and patterning techniques. In *Nanotechnology-Enabled Sensors*, pages 135–210. Springer US.

- [61] K. Kaminska and K. Robbie. Birefringent omnidirectional reflector. *Applied Optics*, 43(7):1570–1576, 2004.
- [62] S. R. Kennedy and M. J. Brett. Porous broadband antireflection coating by glancing angle deposition. *Applied optics*, 42(22):4573–9, Aug. 2003.
- [63] S. R. Kennedy and M. J. Brett. Advanced techniques for the fabrication of square spiral photonic crystals by glancing angle deposition. *Journal of Vacuum Science & Technology B: Microelectronics and Nanometer Structures*, 22(3):1184, May 2004.
- [64] S. R. Kennedy, M. J. Brett, O. Toader, and S. John. Fabrication of Tetragonal Square Spiral Photonic Crystals. *Nano Lett.*, 2(1):59–62, 2002.
- [65] S. Y. Kim. Simultaneous determination of refractive index, extinction coefficient, and void distribution of titanium dioxide thin film by optical methods. *Applied Optics*, 35(34):6703–6707, 1996.
- [66] J. C. Knight. Photonic crystal fibres. *Nature*, 424(6950):847–851, 2003.
- [67] D. Knorr and D. Tracy. A review of microstructure in vapor deposited copper thin films. *Materials Chemistry and Physics*, 41(3):206 – 216, 1995.
- [68] J. D. Krabbe, V. Leontyev, M. T. Taschuk, A. Kovalenko, and M. J. Brett. Square spiral photonic crystal with visible bandgap. *Journal of Applied Physics*, 111(6):064314, 2012.
- [69] K. M. Krause, D. W. Vick, M. Malac, and M. J. Brett. Taking a little off the top: Nanorod array morphology and growth studied by focused ion beam tomography. *Langmuir*, 26(22):17558–17567, 2010.
- [70] V. G. Kravets, S. Neubeck, A. N. Grigorenko, and A. F. Kravets. Plasmonic blackbody: Strong absorption of light by metal nanoparticles embedded in a dielectric matrix. *Phys. Rev. B*, 81:165401, Apr 2010.
- [71] J. Lee, R. Lee, and A. Cangellaris. Time-domain finite-element methods. *IEEE transactions on antennas and propagation*, 45(3):430–442, 1997.
- [72] H. W. Lehmann and K. Frick. Optimizing deposition parameters of electron beam evaporated tio2 films. *Appl. Opt.*, 27(23):4920–4924, Dec 1988.

- [73] V. Leontyev, M. Hawkeye, A. Kovalenko, and M. J. Brett. Omnidirectional reflection from nanocolumnar tio₂ films. *Journal of Applied Physics*, 112(8):084317–084317–8, 2012.
- [74] V. Leontyev, N. G. Wakefield, K. Tabunshchuk, J. C. Sit, M. J. Brett, and A. Kovalenko. Selective transmittance of linearly polarized light in thin films rationally designed by fdtd and fdfd theories and fabricated by glancing angle deposition. *Journal of Applied Physics*, 104(10):104302–104302–9, 2008.
- [75] S. Lichter and J. Chen. Model for columnar microstructure of thin solid films. *Phys. Rev. Lett.*, 56:1396–1399, Mar 1986.
- [76] S. Y. Lin, J. G. Fleming, D. L. Hetherington, B. K. Smith, R. Biswas, K. M. Ho, M. M. Sigalas, W. Zubrzycki, S. R. Kurtz, and J. Bur. A three-dimensional photonic crystal operating at infrared wavelengths. *Nature*, 394(16):251–253, 1998.
- [77] S. Linden, C. Enkrich, G. Dolling, M. W. Klein, J. Zhou, T. Koschny, C. M. Soukoulis, S. Burger, F. Schmidt, and M. Wegener. Photonic metamaterials: Magnetism at optical frequencies. *Selected Topics in Quantum Electronics, IEEE Journal of*, 12(6):1097–1105, nov.-dec. 2006.
- [78] M. E. Lines. Scattering losses in optic fiber materials. i. a new parametrization. *Journal of Applied Physics*, 55(11):4052–4057, 1984.
- [79] M. Lipiski, S. Bastide, P. Panek, and C. Lvy-Clment. Porous silicon antireflection coating by electrochemical and chemical etching for silicon solar cell manufacturing. *physica status solidi (a)*, 197(2):512–517, 2003.
- [80] Y. Liu and X. Zhang. Metamaterials: a new frontier of science and technology. *Chem. Soc. Rev.*, 40:2494–2507, 2011.
- [81] E. Lorenzo, C. J. Oton, N. E. Capuj, M. Ghulinyan, D. Navarro-Urrios, Z. Gaburro, and L. Pavesi. Porous silicon-based rugate filters. *Appl. Opt.*, 44(26):5415–5421, Sep 2005.
- [82] W. Lü, J. Dong, and Z.-Y. Li. Optical properties of aligned carbon nanotube systems studied by the effective-medium approximation method. *Phys. Rev. B*, 63:033401, Dec 2000.

- [83] A. Madaria, A. Kumar, F. Ishikawa, and C. Zhou. Uniform, highly conductive, and patterned transparent films of a percolating silver nanowire network on rigid and flexible substrates using a dry transfer technique. *Nano Research*, 3:564–573, 2010. 10.1007/s12274-010-0017-5.
- [84] J. Manzanares-Martinez, R. Archuleta-Garcia, P. Castro-Garay, D. Moctezuma-Enriquez, and E. Urrutia-Banuelos. One-dimensional photonic heterostructure with broadband omnidirectional reflection. *Progress In Electromagnetics Research*, 111:105–117, 2011.
- [85] R. J. Martin-Palma, V. Torres-Costa, M. Manso, and J. M. Martinez Duart. Applications of nanostructured porous silicon in the field of optical sensing. *Proceedings of SPIE*, 7041:70410D–70410D–7, 2008.
- [86] J. C. Maxwell-Garnett. *Philos. Trans. R. Soc. Lond. A*, 203:385–420, 1904.
- [87] G. Mie. Beitrage zur optik truber medien, speziell kolloidaler metallosungen. *Ann Phys Vierte Folge*, 25(3):377445, 1908.
- [88] N. Q. Minh. Ceramic fuel cells. *Journal of the American Ceramic Society*, 76(3):563–588, 1993.
- [89] A. Mir, A. Akjouj, E. H. El Boudouti, B. Djafari-Rouhani, and L. Dobrzynski. Large omnidirectional band gaps and selective transmission in one-dimensional multilayer photonic structures. *Vacuum*, 63:197–203, 2001.
- [90] P. Monk and E. Suli. Error estimates for yee’s method on non-uniform grids. *Magnetics, IEEE Transactions on*, 30(5):3200–3203, 1994.
- [91] B. A. Movchan and A. V. Demchishin. Study of the structure and properties of thin vacuum condensates of nickel, titanium, tungsten, aluminum oxide and zirconium dioxide. *Fiz. Met. Metalloved.*, 28:653660, 1969.
- [92] J. M. Nieuwenhuizen and H. B. Haanstra. Microfractography of thin films. *Philips Technical Review*, 27(3-4):87–91, 1966.
- [93] G. A. Niklasson, C. G. Granqvist, and O. Hunderi. Effective medium models for the optical properties of inhomogeneous materials. *Appl. Opt.*, 20(1):26–30, Jan 1981.

- [94] A. F. Oskooi, D. Roundy, M. Ibanescu, P. Bermel, J. D. Joannopoulos, , and S. G. Johnson. Meep: A flexible free-software package for electromagnetic simulations by the fdtd method. *Computer Physics Communications*, 181:687702, 2010.
- [95] E. Ozbay. Plasmonics: Merging photonics and electronics at nanoscale dimensions. *Science*, 311(5758):189–193, 2006.
- [96] A. Pandolfo and A. Hollenkamp. Carbon properties and their role in supercapacitors. *Journal of Power Sources*, 157(1):11 – 27, 2006.
- [97] M. Patterson and S. Hughes. Disorder-induced incoherent scattering losses in photonic crystal waveguides: Bloch mode reshaping, multiple scattering, and breakdown of the beer-lambert law. *Physical Review B*, 80(195305), 2009.
- [98] N. J. Podraza, S. M. Pursel, C. Chen, M. W. Horn, and R. W. Collins. Analysis of the optical properties and structure of serial bi-deposited TiO₂ chiral sculptured thin films using Mueller matrix ellipsometry. *Journal of Nanophotonics*, 2(1):021930, 2008.
- [99] A. D. Rakic, A. B. Djurišić, J. M. Elazar, and M. L. Majewski. Optical properties of metallic films for vertical-cavity optoelectronic devices. *Appl. Opt.*, 37(22):5271–5283, Aug 1998.
- [100] F. F. Ren, R. Li, C. Cheng, H. T. Wang, J. Qiu, J. Si, and K. Hirao. Giant enhancement of second harmonic generation in a finite photonic crystal with a single defect and dual-localized modes. *Physical Review B*, 70(24):245109, Dec. 2004.
- [101] D. J. Resnick, W. J. Dauksher, D. Mancini, K. J. Nordquist, T. C. Bailey, S. Johnson, N. Stacey, J. G. Ekerdt, C. G. Willson, S. V. Sreenivasan, and N. Schumaker. Imprint lithography for integrated circuit fabrication. *Journal of Vacuum Science & Technology B: Microelectronics and Nanometer Structures*, 21(6):2624, Dec. 2003.
- [102] K. Robbie and M. J. Brett. Sculptured thin films and glancing angle de-

- position: Growth mechanics and applications. *J. Vac. Sci. Technol. A*, 15(3):1460-1465, 1997.
- [103] K. Robbie, J. C. Sit, and M. J. Brett. Advanced techniques for glancing angle deposition. *Journal of Vacuum Science and Technology B: Microelectronics and Nanometer Structures*, 16(3):1115–1122, 1998.
- [104] R. Ruppin. Evaluation of extended maxwell-garnett theories. *Optics Communications*, 182:273–279, 2000.
- [105] P. Russell. Photonic crystal fibers. *Science*, 299(5605):358–362, 2003.
- [106] K. K. Seet, V. Mizeikis, M. Shigeki, J. Saulios, and H. Misawa. Three-dimensional horizontal circular spiral photonic crystals with stop gaps below $1\mu\text{m}$. *Advanced Materials*, 17(5):541–545, 2005.
- [107] N. Simicevic and D. T. Haynie. Fdtd simulation of exposure of biological material to electromagnetic nanopulses. *Physics in Medicine and Biology*, 50(2):347, 2005.
- [108] J. C. Sit, D. J. Broer, and M. J. Brett. Liquid crystal alignment and switching in porous chiral thin films. *Advanced Materials*, 12(5):371–373, 2000.
- [109] D. R. Smith, W. J. Padilla, D. C. Vier, S. C. Nemat-Nasser, and S. Schultz. Composite medium with simultaneously negative permeability and permittivity. *Phys. Rev. Lett.*, 84:4184–4187, May 2000.
- [110] D. R. Smith, S. Schultz, P. Markoš, and C. M. Soukoulis. Determination of effective permittivity and permeability of metamaterials from reflection and transmission coefficients. *Phys. Rev. B*, 65:195104, Apr 2002.
- [111] J. J. Steele and B. M. J. Nanostructure engineering in porous columnar thin films: recent advances. *J Mater Sci: Mater Electron*, 18:367–379, 2007.
- [112] J. J. Steele, M. T. Taschuk, and M. J. Brett. Nanostructured metal oxide thin films for humidity sensors. *IEEE Sensors J*, 8(7-8):1422–1429, 2008.
- [113] J. J. Steele, A. C. van Popta, M. M. Hawkeye, J. C. Sit, and M. J. Brett. Nanostructured gradient index optical filter for high-speed humidity sensing. *Sensors and Actuators B: Chemical*, 120(1):213 – 219, 2006.

- [114] M. Summers, B. Djurfors, and M. Brett. Fabrication of silicon submicrometer ribbons by glancing angle deposition. *Journal of Microlithography, Microfabrication, and Microsystems*, 4(3):033012, 2005.
- [115] M. A. Summers and M. J. Brett. Optimization of periodic column growth in glancing angle deposition for photonic crystal fabrication. *Nanotechnology*, 19(41):415203, Oct. 2008.
- [116] M. A. Summers and M. J. Brett. Thermal oxidation of periodically aligned silicon square-spirals. *Microelectronic Engineering*, 85(5-6):1222–1224, May 2008.
- [117] G. Sun and A. G. Kirk. Analyses of negative refraction in the partial bandgap of photonic crystals. *Opt. Express*, 16(6):4330–4336, Mar 2008.
- [118] K. V. Tabunshchyk, M. M. Hawkeye, A. Kovalenko, and M. J. Brett. Three-dimensional simulation of periodically structured thin films with uniaxial symmetry. *Journal of Physics D: Applied Physics*, 40:4936–4942, 2007.
- [119] A. Taflove. *Computational Electrodynamics: The Finite-Difference Time-Domain Method*. Artech House, 1995.
- [120] R. Tait, T. Smy, and M. Brett. Modelling and characterization of columnar growth in evaporated films. *Thin Solid Films*, 226(2):196 – 201, 1993.
- [121] L. Thylen, M. Qiu, and S. Anand. Photonic crystals a step towards integrated circuits for photonics. *ChemPhysChem*, 5:1268–1283, 2004.
- [122] O. Toader and S. John. Proposed square spiral microfabrication architecture for large three-dimensional photonic band gap crystals. *Science (New York, N.Y.)*, 292(5519):1133–5, May 2001.
- [123] O. Toader and S. John. Square spiral photonic crystals: Robust architecture for microfabrication of materials with large three-dimensional photonic band gaps. *Physical Review E*, 66(1):016610, July 2002.
- [124] J. Torres, D. Coquillat, R. Legros, J. P. Lascaray, F. Teppe, D. Scalbert, D. Peyrade, Y. Chen, O. Briot, M. Le Vassor d’Yerville, E. Centeno,

- D. Cassagne, and J. P. Albert. Giant second-harmonic generation in a one-dimensional gan photonic crystal. *Phys. Rev. B*, 69:085105, Feb 2004.
- [125] C. Tserkezis, N. Stefanou, and N. Papanikolaou. Extraordinary refractive properties of photonic crystals of metallic nanorods. *J. Opt. Soc. Am. B*, 27(12):2620–2627, Dec 2010.
- [126] K. Tsunoda, S. Adachi, and M. Takahashi. Spectroscopic ellipsometry study of ion-implanted si(100) wafers. *Journal of Applied Physics*, 91(5):2936–2941, 2002.
- [127] K. Umashankar and A. Taflove. A novel method to analyze electromagnetic scattering of complex objects. *Electromagnetic Compatibility, IEEE Transactions on*, EMC-24(4):397–405, nov. 1982.
- [128] A. C. van Popta, M. J. Brett, and J. C. Sit. Double-handed circular bragg phenomena in polygonal helix thin films. *Journal of Applied Physics*, 98(8):083517–083517–9, oct 2005.
- [129] A. C. van Popta, M. M. Hawkeye, and M. J. Brett. Gradient-index narrow-bandpass filter fabricated with glancing-angle deposition. *Optics Lett.*, 29(21):2545–2547, 2004.
- [130] A. C. van Popta, J. C. Sit, and M. J. Brett. Optical properties of porous helical thin films. *Appl. Opt.*, 43(18):3632–3639, Jun 2004.
- [131] A. C. van Popta, J. C. Sit, and M. J. Brett. Optical properties of porous helical thin films and the effects of post-deposition annealing. *Organic Optoelectronics and Photonics, Proceedings of SPIE*, Vol. 5464:198–298, 2004.
- [132] V. Veselago, L. Braginsky, V. Shklover, and C. Hafner. Negative refractive index materials. *Journal of Computational and Theoretical Nanoscience*, 3(2):189–218, 2006.
- [133] V. G. Veselago. The electrodynamics of substances with simultaneously negative values of ϵ and μ . *Soviet Physics Uspekhi*, 10(4):509, 1968.
- [134] N. Wakefield and J. Sit. Three-dimensional alignment of liquid crystals in nanostructured porous thin films. *Proc. SPIE 6654, Liquid Crystals XI*, (665404), 2007.

- [135] N. G. Wakefield, A. L. Elias, M. J. Brett, J. C. Sit, and D. J. Broer. Alignment of liquid crystals infiltrated into porous thin films with tailored nanostructures grown by glancing angle deposition. *Molecular Crystals and Liquid Crystals*, 475(1):85–96, 2007.
- [136] G. Wang, L. Zhang, and J. Zhang. A review of electrode materials for electrochemical supercapacitors. *Chem. Soc. Rev.*, 41:797–828, 2011.
- [137] H. E. Went, A. P. Hibbins, J. R. Sambles, C. R. Lawrence, and A. P. Crick. Selective transmission through very deep zero-order metallic gratings at microwave frequencies. *Applied Physics Letters*, 77(18):2789–2791, oct 2000.
- [138] P. Westbergh, J. Gustavsson, B. Ko andgel, A. Haglund, and A. Larsson. Impact of photon lifetime on high-speed vcsel performance. *Selected Topics in Quantum Electronics, IEEE Journal of*, 17(6):1603–1613, nov.-dec. 2011.
- [139] S. Woo and C. K. Hwangbo. Optical anisotropy of tio_2 and mgf_2 thin films prepared by glancing angle deposition. *Journal of the Korean Physical Society*, 49:2136–2142, 2006.
- [140] T. Wriedt. A review of elastic light scattering theories. *Particle & Particle Systems Characterization*, 15(2):67–74, 1998.
- [141] E. Xifre-Perez, L. F. Marsal, J. Ferre-Borrull, and J. Pallares. Confinement in a planar waveguide with porous silicon omnidirectional mirrors as confining walls. *Journal of Luminescence*, 121:301–303, 2006.
- [142] E. Yablonovitch. Inhibited Spontaneous Emission in Solid-State Physics and Electronics. *Physical Review Letters*, 58(20):2059–2062, May 1987.
- [143] E. Yablonovitch and K. Leung. Photonic band structure: Non-spherical atoms in the face-centered-cubic case. *Physica B: Condensed Matter*, 175(13):81–86, 1991. [Analogies in Optics and Micro-Electronics](#).
- [144] P. Yang and K. N. Liou. Finite-difference time domain method for light scattering by small ice crystals in three-dimensional space. *J. Opt. Soc. Am. A*, 13(10):2072–2085, Oct 1996.

- [145] A. Yariv and P. Yeh. *Optical waves in crystals*. John Wiley and Sons, 1984.
- [146] K. S. Yee. Numerical solution of initial boundary value problems involving maxwell's equations in isotropic media. *IEEE Trans. Antennas Propagat.*, AP-14:302307, 1966.
- [147] H. Yoda, K. Muro, and S. Kazuo. Fabrication of rugate optical filters using a-sio x:h thin films. *IEICE Trans. Electron.*, E91-C(10):1639–1643, 2008.
- [148] T. Yonte, J. J. Monzon, A. Felipe, and L. L. Sanchez-Soto. Optimizing omnidirectional reflection by multilayer mirrors. *J. Opt. A: Pure Appl. Opt.*, 6:127–131, 2004.
- [149] Z. Yu, P. Deshpande, W. Wu, J. Wang, and S. Y. Chow. Reflective polarizer based on a stacked double-layer subwavelength metal grating structure fabricated using nanoimprint lithography. *Applied Physics Letters*, 77(7):927–929, 2000.
- [150] Y. Zeng, T. Alford, Y. Zou, A. Amali, B. Ullrich, F. Deng, and S. Lau. Texture and microstructural evolution of thin silver films in Ag/Ti bilayers. *Journal of Applied Optics*, 83(2):779–785, JAN 15 1998.
- [151] J. Zhang, Y. Li, X. Zhang, and B. Yang. Colloidal Self-Assembly Meets Nanofabrication: From Two-Dimensional Colloidal Crystals to Nanostructure Arrays. *Advanced materials (Deerfield Beach, Fla.)*, 22(38):4249–69, Aug. 2010.
- [152] K. Zhang, Q. Wu, J.-H. Fu, F.-Y. Meng, and L.-W. Li. Metamaterials with tunable negative permeability based on mie resonance. *Magnetics, IEEE Transactions on*, 48(11):4289–4292, nov. 2012.
- [153] S. Zongping and S. M. Haile. A high-performance cathode for the next generation of solid-oxide fuel cells. *Nature*, 431:170–173, 2004.